의학박사 학위논문

Mechanisms underlying hippocampal regulation of behavioral despair and hippocampal dysfunction in the metabolic disorder.

해마의 행동적 절망 조절과 대사 이상에 의한 해마 기능장애 기전

2021년 8월

서울대학교 대학원

의과학과 의과학 전공

윤 상 호

A thesis of the Degree of Doctor of Philosophy

해마의 행동적 절망 조절과 대사 이상에 의한 해마 기능장애 기전

Mechanisms underlying hippocampal regulation of behavioral despair and hippocampal dysfunction in the metabolic disorder.

August 2021

The Department of Biomedical Sciences

Seoul National University College of Medicine

Sang Ho Yoon

해마의 행동적 절망 조절과 대사 이상에 의한 해마 기능장애 기전

지도 교수 김 명 환

이 논문을 의학박사 학위논문으로 제출함

2021년 4월

서울대학교 대학원

의과학과 의과학 전공

윤 상 호

윤상호의 의학박사 학위논문을 인준함

2021년 7월

위 원 장 _____

부위원장 _____

위 원 _____

위 원 _____

위 원 _____

Mechanisms underlying hippocampal regulation of behavioral despair and hippocampal dysfunction in the metabolic disorder.

By Sang Ho Yoon

A thesis submitted to the Department of Biomedical Sciences

in partial fulfillment of the requirements

for the Degree of Doctor of Philosophy

at the Seoul National University College of Medicine

July 2021

Approved by Thesis Committee:

Chair _____

Vice chair _____

Examiner _____

Examiner _____

Examiner _____

Abstract

Modifications in the hippocampal circuits induced by the activity-dependent changes in synaptic transmission and neuronal excitability are thought to play a major role in learning and memory formation. In addition to cognitive function, the hippocampus plays diverse functions through the neural connection with various brain areas. As the hippocampus is vulnerable to changes in microenvironments, hippocampal damage and resultant impairments in cognitive and emotion-related behaviors are frequently accompanied by various diseases including metabolic disorders. However, hippocampal regulation of emotional behaviors is unclear. In addition, it is unknown how altered brain metabolism affects hippocampal microcircuits. In this study, I investigated the emotional role of the dorsal hippocampus, which is generally thought to mediate cognitive processing. The thesis also addresses the molecular and cellular changes associated with hippocampal pathology in an inborn error of metabolism. Knockdown of $GABA_A$ receptor gamma 2 subunit gene (Gabrg2) or DREADD-mediated suppression of interneuron activity in the dorsal hippocampus resulted in anti-despair-like behaviors in mice. Conversely, pharmacological and chemogenetic potentiation of GABAergic transmission in CA1 neurons induced despair-like behaviors. These results indicate that inhibitory circuitry in the dorsal hippocampus

selectively affects despair-like behaviors. To understand how altered brain metabolism affects hippocampal circuits, I analyzed molecular and cellular changes in an inborn error of metabolism caused by aminopeptidase P1 deficiency. A deficiency of aminopeptidase P1 in mice resulted in altered gene expression and glial population in the hippocampus. The density of astrocytes was increased in the entire hippocampus, while the density of microglia was selectively increased in the hippocampal CA3 area in which severe neurodegeneration is observed. These observations indicate that insufficient astrocytic neuroprotection and enhanced neuronal excitability may underlie selective excitotoxic cell death of CA3 neurons and that migration of microglia to the sites of neurodegeneration. Collectively, the thesis suggests that the dorsal hippocampus regulates despair-like behaviors, in addition to cognitive processing, and that chronic exposure of the hippocampus to the accumulated substrates in aminopeptidase P1 deficiency leads to hippocampal dysfunction through the alterations in glial density and neuronal excitability.

Keywords

Hippocampus, Hippocampal circuit, Behavioral despair, inhibitory synaptic transmission, microenvironment, inborn errors of metabolism, aminopeptidase P1

Student number: 2013-21783

Contents

List of Figures

Chapter 1. Altered GABAergic inhibition in CA1 pyramidal neurons modifies despair-like behavior in mice.

Chapter 2. Deficiency of aminopeptidase P1 causes neurodegeneration and altered glial population in the hippocampus.

List of Tables

Chapter 1. Altered GABAergic inhibition in CA1 pyramidal neurons modifies despair−like behavior in mice.

Chapter 2. Deficiency of aminopeptidase P1 causes neurodegeneration and altered glial population in the hippocampus.

General introduction

The hippocampus plays a critical role in both cognition and mood. Based on the anatomical connectivity and deficit lesion studies, it is widely accepted that the hippocampus is functionally segregated along the hippocampal longitudinal axis; dorsal (posterior in primates) and ventral (anterior in primates) regions of the hippocampus contribute to cognitive and emotional processing, respectively (Strange et al. 2014; Fanselow and Dong 2010). It has been suggested that the dorsal hippocampus send projections to the retrosplenial area (RSP) of the anterior cingulate cortex and the septum, while ventral hippocampal projections target the medial prefrontal cortex (mPFC), hypothalamus, amygdala, bed nucleus of the stria terminalis (BNST), and the nucleus accumbens (NA) (Tannenholz, Jimenez, and Kheirbek 2014). In line with the anatomical connectivity, lesions in the dorsal hippocampus impaired spatial memory and cognitive function, whereas lesions in the ventral hippocampus altered stress responses and emotional behaviors including innate anxiety (Fanselow and Dong 2010; Strange et al. 2014). However, several studies observed that the ventral hippocampus contribute to spatial memory formation in rodents (Ferbinteanu, Ray, and McDonald 2003; Rudy and Matus-Amat 2005). There is also evidence that manipulations of the dorsal hippocampus modify

emotion-related behaviors including depression-like behaviors and conditioned fear in rodents(Kim, Chang, and Johnston 2012; Han et al. 2017). Importantly, recent studies revealed that dorsal hippocampus has projections to the NAc and mPFC(Strange et al. 2014; Xu and Sudhof 2013; Ahrlund-Richter et al. 2019). These brain areas are known to play pivotal roles in emotional and motivational behaviors(Strange et al. 2014). However, the behavioral responses to altered activity of the dorsal hippocampus remain largely unknown, except for learning and memory.

The hippocampus is plastic and vulnerable to a variety of stimuli such as stress, ischemia, abnormal brain activity, and altered brain metabolism. Hippocampal atrophy and/or sclerosis is frequently observed in late-onset neurodegenerative diseases, Cushing's disease, epilepsy, ischemic stroke, and inheritable metabolic diseases(Anand and Dhikav 2012; Bae et al. 2018). Compared to other diseases, hippocampal pathology in inheritable metabolic diseases, also known as inborn errors of metabolism (IEMs), has not been extensively studied. The accumulation of toxic metabolites or deficiency of necessary substances resulting from a defective metabolic process seem to cause hippocampal dysfunction and pathology(Bae et al. 2018). However, IEMs are extremely diverse and thus individual IEMs are rare(Applegarth, Toone, and Lowry 2000;

Raghuveer, Garg, and Graf 2006; Sanderson et al. 2006), which hinders the understanding of the neural circuit mechanisms underlying neurological complications in most IEMs, despite that the most serious and common outcomes in IEMs are neurological complications including microcephaly, hyperactivity, attention deficit, autism, and intellectual disability.

In this study, I investigated how altered GABAergic inhibition in the dorsal hippocampal CA1 area influences behavior, and found that altered synaptic inhibition in the dorsal hippocampus is sufficient to modify despair-like behaviors of mice without affecting anxiety and general explorative behaviors. In the second part of the thesis, I investigated the molecular and cellular characteristics of the hippocampal pathology in mice with aminopeptidase P1 deficiency. I show that a deficiency of aminopeptidase P1 modifies gene expression profiles, glial population, and neuronal excitability in the hippocampus.

Chapter 1. Altered GABAergic inhibition in CA1 pyramidal neurons modifies despair-like behavior in mice.

Introduction

Despair is a common human feeling characterized by the loss of hope that significantly disrupts motivation and goal-directed thinking(Snyder et al. 1991). Notably, despair is one of the core symptoms of depressive disorders, and hopelessness is a strong risk factor for suicidal thoughts(Turecki et al. 2012; Nestler et al. 2002). Although the brain mechanisms underlying despair remain unknown, stress is a potent risk factor for depressive symptoms and behavioral despair in humans and laboratory animals, respectively(Nestler et al. 2002; Duman et al. 2016). Conversely, antidepressants improve despair and suicidal thoughts in patients with depression, as well as behavioral despair in rodent models(Nestler et al. 2002; Duman et al. 2016; Phillips et al. 2019).

A growing body of evidence suggests that rapid-acting antidepressant agents, such as ketamine (an NMDA receptor blocker),

the ketamine metabolite (2R,6R)-hydroxynorketamine, and scopolamine (a muscarinic acetylcholine receptor antagonist), share core mechanisms for synaptic action by rapidly suppressing synaptic inhibition to pyramidal neurons in the medial prefrontal cortex (mPFC) and hippocampus(Zanos et al. 2018; Widman and McMahon 2018). Enhanced glutamatergic neurotransmission, termed the "glutamate burst" and caused by disinhibition of pyramidal neurons, is thought to trigger protein synthesis-dependent LTP (long-term potentiation)-like changes in synaptic efficacy and neuronal morphology in the brain areas implicated in depressive disorders(Duman et al. 2016). The activation of signaling cascades associated with protein synthesis, including eukaryotic elongation factor 2 (eEF2), mammalian target of rapamycin (mTOR), and extracellular signal-regulated kinase (ERK), reportedly increases brain-derived neurotrophic factor (BDNF) and synaptic protein synthesis, modifies the function of neural circuits, and mediates the effects of rapid-acting antidepressant agents(Li et al. 2010; Autry et al. 2011; Duman et al. 2016).

A low dose of ketamine rapidly disinhibits hippocampal CA1 neurons, consequently increasing the probability of synaptically driven action

potential in CA1 pyramidal neurons(Widman and McMahon 2018). In line with these findings, L-655,708 or MRK-016, negative allosteric modulators of the α5-subunit-containing $GABA_A$ receptor ($GABA_AR$), rapidly reverse depression-like behaviors and stress-impaired AMPAR-mediated transmission at hippocampal temporoammonic-CA1 synapses in stressed rodents(Fischell et al. 2015). Collectively, these findings demonstrate that disinhibition of CA1 pyramidal neurons might be associated with the effects of rapid-acting antidepressants.

Deficiency of RalBP1, a downstream effector of the small GTP-binding proteins RalA and RalB, results in reduced interneuron density in the hippocampal CA1 areas(Bae et al. 2013). Basal excitatory synaptic transmission and LTP at the Schaffer collateral-CA1 synapse were normal in $RalBP1^{-/-}$ mice, but long-term depression (LTD) was modestly attenuated(Han et al. 2009). Based on these findings, I investigated whether reduced synaptic inhibition in CA1 pyramidal neurons caused by reduced interneuron numbers in RalBP1-mutant mice recapitulates disinhibition and behavioral effects of rapid-acting antidepressants.

Although depression- or stress-related synaptic deficits and antidepressant-induced synaptic changes are observed in both the mPFC and the hippocampus, the behavioral responses to altered activity of hippocampal CA1 microcircuits remain unclear. To address this issue, I selectively manipulated the activity of CA1 interneurons or inhibitory synaptic transmission to CA1 pyramidal neurons. I show here that disinhibition of CA1 pyramidal neurons is sufficient to induce anti-despair-like behaviors in mice. The present study suggests that the enhanced hippocampal CA1 neuron activity contributes to the antidepressant effects of ketamine.

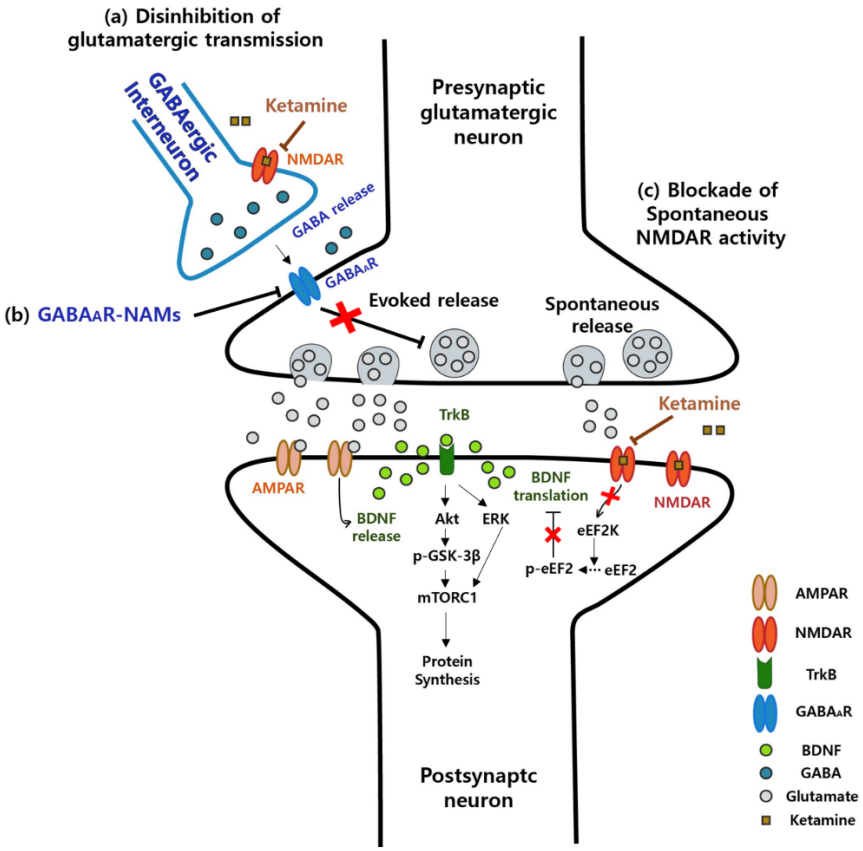

Modified from (Zanos et al. 2018).

Figure 1. Mechanism for antidepressant effect of Ketamine.

(a) Disinhibition of glutamatergic transmission: Ketamine selectively block N-methyl-D-aspartate receptors (NMDARs) expressed on GABAergic inhibitory interneurons, leading to a disinhibition of pyramidal neurons, and enhanced glutamatergic transmission. The resulting glutamatergic activity promotes BDNF release, leading to activation of mTOR and ERK signaling associated with protein synthesis.

(b) Negative modulators of $GABA_A$ receptors ($GABA_AR$-NAMs) directly exert to decrease GABAergic inhibition on pyramidal neuron, evoking glutamatergic transmission.

(c) Blockade of spontaneous NMDAR activation: Ketamine blocks NMDAR-mediated spontaneous neurotransmission. Inhibition of NMDAR inactivates eukaryotic elongation factor 2 kinase (eEF2K) activity, which prevents phosphorylation of eEF2 substrates. The effect leads to de-suppression of BDNF translation.

Result

Reduced synaptic inhibition in CA1 neurons and anti-despair-like behaviors in RalBP1$^{-/-}$ mice.

RalBP1 is widely expressed in brain neurons and RalBP1$^{-/-}$ mice exhibit fewer GAD67 (glutamic acid decarboxylase 67)-positive neurons in the hippocampus(Bae et al. 2013; Han et al. 2009). To examine the functional consequence of reduced interneurons in the hippocampal CA1 area, I measured the ratio of synaptic excitation (E) and inhibition (I) to CA1 pyramidal neurons. I first recorded evoked excitatory postsynaptic currents (EPSCs) at the reversal potential of inhibitory postsynaptic currents (IPSCs) using a low-chloride (15 mM) pipette solution and then recorded IPSCs at the reversal potential of EPSCs in the same cell (Figure 2a). The reversal potentials of IPSCs and EPSCs were −57 mV and +3 mV, respectively (Figure 3). The amplitudes of evoked IPSCs were significantly decreased in RalBP1$^{-/-}$ CA1 neurons, whereas evoked EPSCs were unaltered (Figure 2b). These results indicate that the RalBP1$^{-/-}$ mutation leads to an increased synaptic E/I ratio in CA1 neurons (Figure 2c).

The hippocampus contains a mixed population of GABAergic (γ-

aminobutyric acid-ergic) interneurons, derived from the medial ganglionic eminence (MGE) and caudal ganglionic eminence (CGE)(Tricoire et al. 2011). I observed fewer MGE-derived parvalbumin (PV)-expressing interneurons, but a normal density of somatostatin (SST)-expressing interneurons, which originate from both MGE and CGE, in the RalBP1$^{-/-}$ hippocampal CA1 region (Figure 4a and b). On examining the density of CGE-derived interneurons expressing vasoactive intestinal peptide (VIP) and/or cholecystokinin (CCK), the density of VIP-positive interneurons, but not CCK-positive interneurons, was reduced in the RalBP1$^{-/-}$ CA1 area (Figure 3c and d).

To understand the behavioral consequences of reduced synaptic inhibition in RalBP1$^{-/-}$ mice, I first investigated mood-related behaviors. I employed the tail suspension test (TST) and forced swim test (FST) to examine depression-like behaviors in RalBP1$^{-/-}$ mice(Steru et al. 1985; Porsolt, Bertin, and Jalfre 1977). Compared with the wild-type (WT) control, RalBP1$^{-/-}$ mice spent significantly less time immobile during the TST and FST (Figure 2d and e), suggesting that RalBP1 deficiency reduces behavioral despair in mice.

I examined additional depression-related behaviors, including anhedonia, locomotor activity, and anxiety, using a series of behavioral tests. During the sucrose consumption test, the degree of preference for sucrose was indistinguishable between genotypes (Figure 2f). RalBP1$^{-/-}$ mice exhibited normal behavior in an open field box (Figure 2g). Furthermore, RalBP1$^{-/-}$ mice did not present behavioral signs of seizures or epileptic electroencephalogram (EEG) rhythms in their homecages (Figure 5). These observations exclude the possibility that the reduced immobility of RalBP1$^{-/-}$ mice during both TST and FST might stem from behavioral hyperactivity(Miyakawa et al. 2001) or epilepsy. Consistent with normal levels of thigmotaxis in the open-field test (Figure 2g), RalBP1$^{-/-}$ mice exhibited normal anxiety levels in both the elevated plus-maze and zero-maze tests (Figure 2h and i). Collectively, these results suggest that the deficiency of RalBP1 selectively affects despair-like behaviors in mice.

RalBP1 deficiency does not affect hippocampus-dependent learning, social interaction and sensory gating.

I examined hippocampus-dependent learning and memory function in RalBP1 mutant mice. In Morris water maze training session, RalBP1 mutant mice showed prolonged escape latency in the first two days (day 1= 71.83±7.17 s, day 2= 75.25±6.84 s for RalBP1$^{-/-}$ mice), compared with WT littermates (day 1= 73.77±3.97 s, day 2= 53.23±7.09 s for WT mice). But, there was no significant difference between both genotypes (two-way ANOVA repeated measure: group $F_{(1, 19)}$ = 1.430 p= 0.247; training x group $F_{(6, 114)}$ = 1.870 p= 0.092) (Figure 6a). In accordance with this result, both genotypes spent more time in the target quadrant than any of the three other quadrants in the recall test (Figure 6b and c). The Morris water maze performance of RalBP1$^{-/-}$ mice was not affected by motor function, as revealed by normal swimming speed (+/+, 16.54 ± 1.29 cm/s; –/–, 17.15 ± 1.37 cm/s; $p > 0.05$, Student t-test) and rotarod performance (Figure 6d). RalBP1$^{-/-}$ mice also performed normally both in the contextual and in the cued fear conditioning tests (Figure 6e). These results suggest that hippocampus-dependent learning and memory remain normal in

RalBP1$^{-/-}$ mice. As dysfunction of GABAergic neurotransmission has been implicated in the pathophysiology of autism and schizophrenia(Marin 2012), I assessed social interaction, repetitive behaviors, and sensory gating function in RalBP1$^{-/-}$ mice. In the three-chamber test(Moy et al. 2004), WT and RalBP1$^{-/-}$ mice showed similar sociability and preference for social novelty (Figure 6f-i). In addition, RalBP1$^{-/-}$ mice did not display repetitive or stereotyped behaviors (Figure 6j), as determined by normal behaviors in the marble-burying test(Thomas et al. 2009). Impairment in prepulse inhibition of the acoustic startle response, a deficit in sensorimotor gating, which is frequently observed in animal models of schizophrenia(Swerdlow et al. 2008), was not detected in RalBP1$^{-/-}$ mice (Figure 6k).

Altered hippocampal circuit function is associated with anti-despair-like behavior in RalBP1$^{-/-}$ mice.

I wondered whether changes in brain regions other than the hippocampus are responsible for anti-despair-like behaviors in RalBP1$^{-/-}$ mice. The PFC and amygdala have been implicated in despair/depression-like behaviors(Covington et al. 2010; Kumar et al.

2013; Mineur, Taylor, and Picciotto 2014; Shi et al. 2012). However, the interneuron density in the mPFC and basolateral amygdala of RalBP1$^{-/-}$ mice were comparable with those of WT mice (Figure 7).

Based on the observed altered hippocampal network and anti-despair-like behaviors in RalBP1$^{-/-}$ mice, I wondered whether pharmacological potentiation of GABAergic transmission in the hippocampal CA1 area would induce despair-like behavior in mice. Indeed, bilateral infusion of muscimol, a $GABA_AR$ agonist, into the dorsal hippocampal CA1 region of WT mice induced despair-like behaviors in a dose-dependent manner during the TST (Figure 8a and b). I further examined whether enhancement of GABAergic transmission in the CA1 area would reverse anti-despair-like behavior in RalBP1$^{-/-}$ mice. Cannula implantation did not affect anti-despair-like behaviors in RalBP1$^{-/-}$ mice, as reduced immobility in RalBP1$^{-/-}$ mice was again observed during the TST (Figure 8c, TST1). However, on infusing muscimol (0.5 μg) bilaterally into the hippocampal CA1 region, the immobility observed in RalBP1$^{-/-}$ mice was comparable with that of saline-treated WT mice (Figure 8c, TST2). Behavioral changes in RalBP1$^{-/-}$ mice were treatment-specific

as RalBP1$^{-/-}$ mice regained anti-despair-like behaviors when both genotypes were administered saline (Figure 8c, TST3). These results indicate that altered activity in the hippocampal network is responsible for anti-despair-like behaviors in RalBP1$^{-/-}$ mice.

Activation of signaling pathways associated with protein synthesis, such as the mTOR, ERK and/or eEF2 signaling pathways, is required to mediate behavioral effects of the rapidly acting antidepressant ketamine(Autry et al. 2011; Li et al. 2010). I investigated whether activation of these signaling pathways is accompanied in the RalBP1$^{-/-}$ hippocampus. RalBP1$^{-/-}$ mice exhibited significantly reduced levels of phosphorylated (inactivated) eEF2 compared with WT mice, whereas both genotypes showed similar levels of total eEF2 in the hippocampus (Figure 8d). As dephosphorylation (activation) of eEF2 stimulates protein synthesis and blockade of action potential-mediated network activity promotes phosphorylation of eEF2(Autry et al. 2011; Sutton et al. 2007), enhanced hippocampal network activity caused by disinhibition promotes dephosphorylation of eEF2 and translation of downstream signaling molecules, including BDNF(Autry et al. 2011). However, hippocampal BDNF levels in RalBP1$^{-/-}$ mice did not differ

from those in WT littermates. Consistent with this result, modification of mTOR and ERK signaling, downstream pathways of BDNF−TrkB (tropomyosin receptor kinase B) signaling, was not detected in the RalBP1$^{-/-}$ mouse hippocampus, as neither total protein expression nor phosphorylation levels differed between genotypes (Figure 8d). Considering that excitatory synaptic functions, including NMDAR− and AMPAR−mediated synaptic transmissions, as well as expression levels of excitatory synaptic proteins, are normal in the RalBP1$^{-/-}$ mouse hippocampus(Han et al. 2009), activation of the hippocampal eEF2 signaling pathway might be associated with reduced synaptic inhibition in RalBP1$^{-/-}$ mice.

Suppression of synaptic inhibition in CA1 pyramidal neurons induces anti−despair−like behavior

Synaptic $GABA_A$Rs contain one of the three γ subunits (γ_1 − γ_3), and the γ_2 subunit encoded by the Gabrg2 gene plays a critical role in clustering major postsynaptic $GABA_A$Rs(Essrich et al. 1998; Jacob, Moss, and Jurd 2008). To examine the direct causal relationship between reduced synaptic inhibition in CA1 neurons and anti−despair−

like behaviors in mice, I prepared four different knockdown vectors containing short hairpin RNA (shRNA) targeting the $GABA_AR$ γ_2 subunit (Gabrg2), and determined the gene knockdown efficiency of each construct in HEK293T cells (Figure 9). An shRNA sequence with the highest target knockdown activity (Gabrg2-shRNA#3, shGabrg2) was subcloned into the lentiviral transfer vector and delivered into CA1 neurons (Figure 10a, b and Figure 9d). Gabrg2 knockdown significantly decreased the frequency but not the amplitude of miniature IPSCs (mIPSCs) in CA1 neurons (Figure 10c-e). In contrast to mIPSCs, neither the frequency nor amplitude of miniature EPSCs (mEPSCs) was affected by Gabrg2 knockdown (Figure 10f-h). These results rule out nonspecific neuronal defects induced by shRNA expression or lentivirus infection, excluding homeostatic downregulation of glutamatergic neurotransmission, which is observed in Gabrg2-mutant mice(Ren et al. 2016). Normal mIPSCs and mEPSCs in CA1 neurons expressing a non-targeting shRNA (shNT) further support the specificity of Gabrg2 knockdown. Consistent with fewer mIPSCs, CA1 pyramidal neurons infected with shGabrg2 exhibited reduced amplitudes of evoked IPSCs and increased EPSC/IPSC ratios when

compared with those infected with shNT or those non-infected (Figure 10i-l).

I then examined the effect of Gabrg2 knockdown in CA1 neurons on despair-like behaviors. Similar to RalBP1$^{-/-}$ mice injected with virus expressing shNT, WT mice infected with shGabrg2-expressing virus spent a significantly reduced time immobile in the TST than those infected with shNT virus (Figure 10m and n). Given that general locomotor activity in the open field box was unaltered by Gabrg2 knockdown in CA1 neurons (Figure 10o and p), reduced immobility in the TST reflects anti-despair-like behavior in mice.

Pharmacogenetic manipulation of CA1 interneuron activity modulates behavioral despair

Reduction of CA1 interneurons or inhibitory synaptic transmission to CA1 pyramidal neurons induced anti-despair-like behaviors in mice. Based on these findings, I hypothesized that changes in CA1 interneuron activity might modulate behavioral despair. To selectively manipulate the activity of CA1 interneurons, I expressed excitatory (hM3Dq) or inhibitory (hM4Di) designer receptors exclusively

activated by designer drugs (DREADDs) in the hippocampal CA1 area of Vgat-ires-Cre knock-in (Vgat-Cre) mice using adeno-associated virus (AAV) carrying Cre-dependent (double-floxed inverse orientation, DIO) DREADD receptor expression vectors (Figure 11a). mCherry signals were restricted to GAD67-positive inhibitory neurons (Figure 11b), including PV- and SST-expressing neurons (Figure 12).

I confirmed the action of clozapine-N-oxide (CNO) in controlling the activity of DREADD-expressing neurons using whole-cell patch-clamp recordings. A bath application of CNO rapidly depolarized the membrane potential and significantly increased the firing rate in hM3Dq-expressing neurons, whereas hM4Di-expressing neurons exhibited hyperpolarization and decreased firing rates in response to CNO perfusion (Figure 11c-e). In the absence of DREADDs (DiO-mCherry), CNO did not affect membrane potential or firing rate.

I next explored the role of CA1 interneuron activity in modulating behavioral despair (Figure 11f-i). The expression of DREADDs in inhibitory neurons did not affect behavioral despair. In the absence of CNO, all groups spent a similar amount of time immobile during both the TST (Figure 11f) and FST (Figure 11h). Interestingly, CNO

injection markedly increased the immobility time of hM3Dq-expressing mice in the TST (Figure 11g) and FST (Figure 11i). In contrast, hM4Di-expressing mice exhibited reduced immobility in both the TST and FST following CNO injection. However, CNO injection did not produce any statistically significant changes in the immobility time of mCherry-expressing mice (TST: $t_{(9)} = -0.726$, $P = 0.487$; FST: $t_{(6)} = -2.418$, $P = 0.052$; paired *t*-test). CNO-induced changes in TST and FST behaviors were unlikely to arise from altered general activity or anxiety, as hM3Dq- and hM4Di-expressing mice showed similar locomotor activities and thigmotaxis levels when compared with mCherry-expressing mice in the open-field test (Figure 11j-m).

I further examined whether a specific type of hippocampal interneurons was associated with despair-like behaviors (Figure 13). On injecting AAV2-hSyn-DIO-DREADDs-mCherry into the hippocampal CA1 area of PV-Cre knock-in (PV-Cre) mice, mCherry signals were mainly detected in PV-positive cells (Figure 13a and b). A small portion of mCherry-expressing cells was immunostained with anti-SST antibodies, indicating DREADD expression in cells expressing both PV and SST (Figure 14). Infection of WT mice with a

mixture of AAV-SST-Cre and AAV2-hSyn-DIO-DREADDs-mCherry predominantly expressed DREADDs-mCherry in SST-expressing cells (Figure 13c, d and Figure 15). However, pharmacogenetic manipulation of both types of interneurons produced similar effects on immobility behaviors in the TST and FST (Figure 13e-l). Activation of PV- or SST-expressing cells increased immobility behaviors, while suppression of either type of interneuron decreased despair-like behaviors. Consistent with the pharmocogenetic manipulation of Vgat-positive interneurons, altered activity in PV or SST-positive cells did not significantly impact open-field behaviors of mice (Figure 13m-t). Collectively, these results indicate that changes in CA1 interneuron activity are sufficient for modulating despair-like behaviors.

Pharmacological disinhibition induces rapid eEF2 activation in the hippocampus and transient antidepressant-like behavior

RalBP1$^{-/-}$ mice exhibited enhanced eEF2 activation in the hippocampus (Figure 8), but the expression levels and function of NMDARs in RalBP1$^{-/-}$ CA1 neurons remained unaltered(Han et al. 2009). Based on these observations, I hypothesized that reduced synaptic inhibition and the resultant activation of principal neurons might be sufficient to activate eEF2 signaling. To assess this hypothesis, I examined the effect of disinhibition induced by the $GABA_AR$ antagonist pentylenetetrazol (PTZ) (Huang et al. 2001) on phosphorylation and expression levels of eEF2 in the WT hippocampus. A single administration of a subconvulsive dose (20 mg/kg, i.p.) of PTZ induced rapid (< 30min) and significant dephosphorylation of eEF2 in the hippocampus. However, the PTZ-induced activation of eEF2 did not alter BDNF levels or activation of mTOR and ERK signaling in the hippocampus (Figure 16a).

I next examined the effect of acute PTZ administration on TST behaviors. A single administration of PTZ (20 mg/kg, i.p.) significantly reduced the immobility time of mice during the 6-min TST (Figure

16b). This concentration of PTZ is a sub-convulsant dose, as no detectable convulsions, seizure behaviors, or hyperactivity were observed (Figure 17). I further examined the effect of PTZ-induced disinhibition on stress-induced despair-like behaviors. Accordingly, I measured the immobility time of WT mice in the TST (TST1; Figure 16c, d) and assigned mice to two experimental groups. One group received chronic unpredictable stress (CUS) for 4 weeks (Figure 16d). Mice exposed to CUS spent significantly more time immobile when compared with controls, indicating CUS-induced despair-like behaviors in the stressed group (TST2; Figure 16d). Furthermore, acute PTZ administration (20 mg/kg, i.p., 30 min before the test) effectively improved the despair-like behaviors of stressed mice, as both mice groups spent similar amounts of time immobile in the third TST (TST3; Figure 16d). Intriguingly, a single PTZ administration did not induce a long-lasting behavioral change in stressed mice. Mice exposed to chronic stress displayed enhanced despair-like behavior when compared with control mice in the fourth TST, performed two days after PTZ administration (TST4; Figure 16d). As PTZ has a short half-life (2.5 - 3.8 h) in rodents(Meilleur et al. 2003), the rapid and

short-lasting behavioral effects of PTZ could be attributed to transient synaptic disinhibition and activation of eEF2. I then wondered whether eEF2 activity would return to the basal level within 2 days of PTZ administration. Using a different cohort of unstressed mice, I investigated hippocampal eEF2 phosphorylation levels and TST behaviors of mice 48 h after drug administration. Unexpectedly, the phosphorylation levels of eEF2 were still lower in the PTZ group than those detected in the vehicle group (Figure 16e). Moreover, despite sustained eEF2 activation, hippocampal BDNF levels did not differ between the two groups. Similar to mice exposed to CUS, antidepressant behavior induced by a single PTZ administration did not persist for 48 h in unstressed mice (Figure 18). These findings further indicate that the activation of BDNF signaling may be required for sustained antidepressant behaviors.

Ketamine induces rapid activation of CA1 pyramidal neurons and anti-despair-like behaviors

In hippocampal slice electrophysiology, it has been reported that 1 μM of ketamine, a rapid-acting antidepressant, disinhibits CA1 pyramidal neurons and consequently increases the activity of these neurons(Widman and McMahon 2018). However, it remains unclear whether an antidepressant dose (5 mg/kg, i.p.) of ketamine would rapidly increase hippocampal neuronal activity *in vivo*. Accordingly, I examined hippocampal c-Fos expression as an indicator of neuronal activation. Indeed, the number of cells expressing c-Fos protein was significantly increased in both the hippocampus and mPFC within 1 h after ketamine injection (Figure 19a, b and Figure 20). Interestingly, in ketamine-treated mice, most c-Fos^{+} cells in the CA1 area were distributed in the principal cell layer and did not exhibit immunoreactivity for PV or SST (Figure 19c and d). Considering that alterations in the hippocampal circuitry are sufficient to modify despair-like behaviors (Figures 8, 10, 11, and 13), these results suggest that rapid enhancement in the activity of CA1 pyramidal neurons may contribute to the antidepressant effect of ketamine.

Consistent with enhanced c-Fos expression, a rapid antidepressant effect was detected in the TST at 30 min after ketamine (5 mg/kg) administration (Figure 19e). The decreased immobility during the TST at this time point was unlikely to arise from hyperlocomotion or the dissociative effects of ketamine(Zanos et al. 2016), as enhanced locomotor activities did not last for more than 10 min in the open-field test, which was performed using independent cohorts of animals (Figure 19f and g). Notably, in contrast to PTZ, the behavioral effect of ketamine persisted for more than 48 h after a single intraperitoneal administration (Figure 19e). I investigated the effects of ketamine on intercellular signaling 30 min after a single administration using a different cohort of mice. Ketamine exhibited similar effects to PTZ on hippocampal eEF2. However, ketamine rapidly increased the expression of the mature isoform of BDNF (m-BDNF) in the hippocampus. Moreover, phosphorylation of mTOR and ERK in the hippocampus was significantly enhanced within 30 min of ketamine administration (Figure 19h), indicating the activation of downstream signaling pathways of BDNF. If activation of BDNF signaling is associated with the long-lasting antidepressant effects of ketamine,

suppression of BDNF downstream pathways would preferentially impair the sustained effect of ketamine, leaving the transient effect intact. m-BDNF exhibits a higher affinity for the TrkB receptor than the p75 neurotrophin receptor, and the cellular effects of m-BDNF are mainly mediated via the TrkB receptor(Kowianski et al. 2018; Huang and Reichardt 2001). The TrkB receptor antagonist ANA-12 penetrates the blood-brain barrier and reaches its peak concentration in the mouse brain as early as 30 min after intraperitoneal injection(Cazorla et al. 2011). I, therefore, pretreated mice with ANA-12 (0.5 mg/kg, i.p.) 30 min before ketamine injection and assessed TST behaviors both 30 min and 48 h after ketamine administration (Figure 19i). Ketamine still exhibited antidepressant effects in ANA-12 pretreated mice at 30 min after treatment, such that the immobility time during the TST was significantly reduced by ketamine. This finding is consistent with previous results that pretreatment (30 min) with intracerebroventricular administration of K252a, another TrkB receptor antagonist, did not block the antidepressant effect in the TST at 30 min after ketamine treatment(Koike et al. 2013). Surprisingly, the antidepressant effects of ketamine did not persist for 48 h in ANA-

12 pretreated mice (Figure 19i). Forty-eight hours after the saline or ketamine injection, both groups displayed a similar amount of immobile time in the TST. Consistent with these observations, ketamine rapidly increased hippocampal c-Fos expression in ANA-12 pretreated (30 min before ketamine injection) mice, indicating a transient increase in neuronal activity by disinhibition (Figure 19j and k). Collectively, these results implies that enhanced activity of hippocampal principal neurons may contribute to the rapid antidepressant effect of ketamine and that elevation of BDNF levels and the activation of downstream signaling pathways are responsible for the long-lasting antidepressant effects of ketamine(Shirayama et al. 2002; Autry et al. 2011; Duman and Monteggia 2006).

Discussion

The present study suggests that alterations in synaptic inhibition in CA1 neurons affect despair-like behaviors in mice. RalBP1 mutant mice exhibited anti-despair-like behaviors and reduced synaptic inhibition with normal excitatory synaptic transmission in the hippocampus. The reduced despair-like behaviors of RalBP1$^{-/-}$ mice were reversed by pharmacological potentiation of inhibitory synaptic transmission in CA1 neurons. Hippocampal CA1-specific suppression of inhibitory synaptic transmission via virus-mediated knockdown of Gabrg2 in WT mice recapitulated the anti-despair-like behaviors observed in RalBP1 mutant mice. Chemogenetic manipulation of CA1 interneuron activity bidirectionally modified despair-like behaviors in mice without affecting general locomotor activity and anxiety. Collectively, these results indicate that GABAergic inhibitory control of CA1 pyramidal neurons regulates behavioral despair. Furthermore, the present study provides experimental evidence suggesting that increase in the activity of CA1 pyramidal neurons may contribute to the antidepressant effects of ketamine.

It has been suggested that defects in GABAergic circuitry and an

increased synaptic excitation–inhibition (E/I) ratio in the brain are associated with depressive disorders(Luscher, Shen, and Sahir 2011; Fee, Banasr, and Sibille 2017). Decreased GABA and increased glutamate levels have been observed in the occipital cortex in major depressive disorder (MDD)(Sanacora et al. 2004), and a postmortem study showed fewer GABAergic neurons in the dorsolateral PFC in MDD(Rajkowska et al. 2007). Consistent with these clinical observations, heterozygous deletion of the $GABA_AR$ $\gamma 2$ subunit ($\gamma 2^{+/-}$) induces depression–like behaviors in mice(Ren et al. 2016). Interestingly, $\gamma 2^{+/-}$ mice exhibit a homeostatic–like reduction in the expression levels of glutamate receptors, as well as functional impairment of glutamatergic synapses in the hippocampus and mPFC. These glutamatergic defects and depression–like behaviors in $\gamma 2^{+/-}$ mice were reversed by ketamine(Ren et al. 2016). In addition to GABAergic defects, glutamatergic defects such as reduced spine density in pyramidal neurons and impaired excitatory synaptic transmission and plasticity in the hippocampus were consistently observed in stressed rodents(Csabai et al. 2017; Banasr et al. 2017; Xiong et al. 2018; Sanacora, Treccani, and Popoli 2012; Kallarackal et

al. 2013; Duman et al. 2016). These alterations in excitatory and inhibitory synapses may result in abnormal neuronal activity in the hippocampus. However, the E/I ratio in the hippocampus of patient with depression remains unknown.

Based on the anatomical connectivity and deficit lesion studies, it is widely accepted that the hippocampus is functionally segregated along the hippocampal longitudinal axis; dorsal (posterior in primates) and ventral (anterior in primates) regions of the hippocampus contribute to cognitive and emotional processing, respectively(Moser and Moser 1998; Fanselow and Dong 2010; O'Leary and Cryan 2014)(but see(Strange et al. 2014)). Although the brain area responsible for despair remains elusive, recent studies support my observation that dorsal hippocampal network activity affects depression-related behaviors, at least despair-like behaviors in rodents. Suppression of dendritic expression of hyperpolarization-activated cyclic nucleotide-gated (HCN) channels in CA1 neurons of the dorsal hippocampus enhances neuronal excitability, while behavioral despair was reduced(Kim, Chang, and Johnston 2012). Restoration of HCN channel function by viral expression of TRIP8b in CA1 pyramidal neurons of the dorsal hippocampus reverses neuronal excitability and anti-

despair-like behaviors in TRIP8b mutant mice(Han et al. 2017). Because neural network activity is determined by synaptic function and cellular excitability, it is likely that reduced synaptic inhibition and enhanced neuronal excitability similarly influence neural network activity. I observed that bilateral infusion of muscimol into the dorsal hippocampal CA1 area increased the immobility of WT mice in a dose-dependent manner and reversed the anti-despair-like behaviors of RalBP1$^{-/-}$ mice during the TST (Figure 8). Moreover, previous pharmacological studies have provided evidence that manipulations of the dorsal hippocampus modify despair-like behaviors in rodents. Stereotaxic infusion of UFP-101 (a nociceptin/orphanin-FQ opioid peptide receptor antagonist), 1-aminocyclopropanecarboxylic acid (a ligand for the glycine modulatory site of the NMDAR complex), CGP 37849 (a competitive NMDA receptor antagonist), imipramine (a tricyclic antidepressant), and BDNF into the dorsal hippocampus induced anti-despair-like behaviors in rodents(Goeldner et al. 2010; Przegalinski et al. 1997; Shirayama et al. 2002; Aso et al. 2008). Thus, in addition to cognitive processing, the dorsal hippocampus seems to affect despair-like behaviors rather than anxiety or anhedonia. Additionally, dorsal hippocampus has direct synaptic connections with mPFC neuron(Xu and Sudhof 2013; Ahrlund-Richter et al. 2019;

Hoover and Vertes 2007). Recently, it has been reported that enhancing axon terminal from dorsal hippocampus increases neuronal activity in the mPFC(Ye et al. 2017; Qin et al. 2021), and elevated mPFC neuronal activity induces anti-depressant-like behavior in rodent(Biselli et al. 2021; Fuchikami et al. 2015; Hare et al. 2019). Considering these findings, neuronal connection between dorsal hippocampus and mPFC might influence despair-like behaviors.

Intriguingly, it has been suggested that despair consists of cognitive, emotional, behavioral, and biological domains in humans. Cognitive despair includes hopelessness, guilt, worthlessness and learned helplessness(Shanahan et al. 2019), which is considered to be concerned with cognitive style coping with stress(Turecki et al. 2012; Kircanski, Joormann, and Gotlib 2012; Davidson et al. 2002; Hartley and Phelps 2010). Recent studies have suggested that cognitive function associated with the ability for goal-directed action, problem-solving and decision-making process have implicated in emotional regulation and depressive disorder(Gabrys et al. 2018; Anacker and Hen 2017; Rubin et al. 2014; Baker and Wong 2019; Turecki et al. 2012), and local infusion of muscimol or DREADD-mediated suppression of neuronal activity in the dorsal hippocampus impaired the recall of instrumental learning in mice, indicating disruption of goal-

directed action(Bradfield et al. 2020). Given that coping behavior has been also suggested to be associated with instrumental learning process(Gabrys et al. 2018; Cabib et al. 2020), it is possible that hippocampus-dependent cognitive function might be involve in cognitive aspect of despair or coping behavior.

Immobile behavior in the TST and FST is believed to represent behavioral despair, by reflecting either a failure to persist in escape-directed behavior or the development of passive-coping behavior(Cryan, Mombereau, and Vassout 2005; Krishnan and Nestler 2011). Additionally, behavioral changes in these tests may result from behavioral adaptation or adaptive cognitive processes, at least in the FST(Molendijk and de Kloet 2015). Indeed, the mean immobility time tended to increase when mice were exposed to TSTs more than three times (Figure 8c and 16d), indicating habituation or adaptive learning. However, no significant difference in the immobility time was observed in control group animals across multiple TSTs (Table 2). Moreover, a genotype-specific phenotype was still observed in the third TST (Figure 8c), although intrahippocampal infusion of muscimol reversed the abnormal TST behaviors of RalBP1$^{-/-}$ mice in the previous test. Similarly, I observed bidirectional effects of CUS (TST2) and PTZ

treatments (TST3) on immobile behavior, and recovery (TST4) after PTZ treatment (Figure. 16d). Furthermore, manipulation of hippocampal inhibitory circuitry produced similar effects on immobile behaviors in both the TST and FST, without affecting general locomotor activity. Recent studies have suggested that hippocampal activity might be involved in active or passive coping behavior(de Kloet and Molendijk 2016; Fisher et al. 2018; Commons et al. 2017). Mice showing increased neuronal excitability in the dorsal hippocampus shows enhanced active coping behavior against stress(Fisher et al. 2018). Based on this finding, decreased immobile behavior caused by reduced synaptic inhibition in the dorsal hippocampus might be associated with active coping behavior. However, further investigation is needed to determine whether immobile behaviors in these tests are affected by coping strategies of mice to stressful stimuli or other hippocampus-dependent cognitive functions.

My studies suggest that the anti-despair-like behavior can be attributed to the increased activity of hippocampal CA1 neurons caused by disinhibition or BDNF-induced potentiation of excitatory synaptic transmission. A recent study has revealed that ketamine induces long-

lasting (24 h >) enhancement of excitatory synaptic transmission in CA1 pyramidal neurons(Aguilar-Valles et al. 2020). In the present study, DREADD-mediated manipulation of CA1 interneuron activity rapidly modified behavioral despair. Pharmacological suppression of inhibitory transmission by PTZ (20 mg/kg) administration was sufficient to induce rapid anti-despair-like behaviors in both control and stressed mice (Figure 16). A previous study has shown that a low dose (1 mg/kg, i.p.) of the $GABA_AR$ antagonist picrotoxin did not affect the immobility behaviors of mice during the FST(Autry et al. 2011). Consistent with this result, oral administration of 10 mg/kg, but not 2.5 and 5 mg/kg, picrotoxin produced a statistically significant reduction in the duration of immobility during the FST(Betin et al. 1982). Furthermore, subconvulsant doses of bicuculine (a $GABA_AR$ antagonist) and strychnine (a glycine receptor antagonist) significantly reduce behavioral despair in mice(Betin et al. 1982).

Importantly, however, PTZ did not exhibit sustained antidepressant effects or accompany BDNF elevation in the hippocampus. Considering the short half-life (2.5-3.8 h) of PTZ in the rodent brain(Meilleur et al. 2003), it is likely that the increased E/I ratio induced by disinhibition

was restored to the basal level after complete clearance of PTZ in the absence of BDNF-induced excitatory synaptic potentiation. RalBP1 mutant mice also displayed decreased despair-like behaviors and reduced levels of phosphorylated eEF2, with normal BDNF levels. Reduced interneuron density might result in permanently enhanced activity in CA1 pyramidal neurons and lead to stable anti-despair-like behavior in RalBP1$^{-/-}$ mice. Decreased immobility of RalBP1$^{-/-}$ and PTZ-treated mice in the TST and FST are unlikely to originate from epileptic seizures. RalBP1$^{-/-}$ mice did not exhibit convulsive seizures, epileptic EEG rhythms, or behavioral signs of absence seizures, such as sudden behavioral arrest, nodding, whisker trembling, tail flicking, or hyperactivity. The PTZ dose used in behavioral and biochemical analyses was not sufficiently high to induce overt seizure activity in mice (Figure 17).

Ketamine exhibited rapid (< 30 min) and sustained (~ 48 h) behavioral effects (Figure 18). Ketamine more effectively antagonizes NMDARs on GABAergic interneurons than on pyramidal neurons, resulting in the decreased firing of interneurons and subsequent pyramidal neuron bursts(Homayoun and Moghaddam 2007; Duman et al. 2016; Ali et al.

2020; Widman and McMahon 2018). Consistent with a previous electrophysiology study(Widman and McMahon 2018), ketamine rapidly increased c-Fos expression in the CA1 pyramidal population regardless of TrkB receptor inhibition (Figure 19). These findings suggest that the rapid antidepressant effect of ketamine is attributable, either in full or in part, to the enhanced neuronal activity of pyramidal neurons caused by disinhibition. In contrast to mice administered PTZ, which showed transient antidepressant activity, increased BDNF levels, as well as activation of the downstream signaling molecules ERK and mTOR, were observed in the hippocampus of ketamine-treated mice. This indicates that the long-lasting antidepressant action of ketamine might originate from an enhanced E/I ratio(Aguilar-Valles et al. 2020) or increased signal to noise caused by BDNF-induced neurotropic and neuroplastic changes(Ying et al. 2002; Alonso, Medina, and Pozzo-Miller 2004; Kang and Schuman 1995). Selective suppression of the sustained antidepressant effect of ketamine by the TrkB receptor antagonist ANA-12 further supports this finding (Figure. 18). Although the mechanisms underlying ketamine-induced BDNF elevation and behavioral responses are not comprehensively

understood(Autry et al. 2011; Wray et al. 2018; Zanos et al. 2016), my studies suggest that alterations in hippocampal activity contribute to the antidepressant effect of ketamine.

Collectively, decreased synaptic inhibition in the dorsal CA1 area induces anti-despair-like behavior, and enhancement of synaptic inhibition increases immobile behavior in TST and FST. Based on these finding, my study suggests that dorsal hippocampus regulates behavioral despair in mice.

Method

Animals.

All experiments were performed using male mice (C57BL/6N), except for the EEG recordings. Animals were group-housed (3-5/cage) in a specific pathogen-free facility and maintained in a climate-controlled room with free access to food and water under a 12 h light/dark cycle. Generation and genotyping of RalBP1 mutant mice have been described previously(Han et al. 2009; Bae et al. 2013). RalBP1 mutant mice and Vgat-ires-Cre (Slc32a1$^{tm2(cre)Lowl}$ knock-in; Jackson Laboratory stock #016962) mice were backcrossed to C57BL/6N (Orient Bio, Sungnam, Korea) mice for at least 10 generations before use. PV-Cre knock-in (Pvalb$^{tm1(cre)Arbr}$; Jackson Laboratory stock #017320) mice were transferred from Institute for Basic Science (IBS, Daejeon, Korea) and were backcrossed to C57BL/6N mice for 2 generations. Animal maintenance and all animal experiments were approved by the Institutional Animal Care and Use Committee (IACUC) at SNU.

Behaviors analyses

All behavioral tests were performed between 10 a.m. and 6 p.m. with male mice that were at least 9 weeks old at the start of testing. All experimental mice were acclimated to the behavior testing room for at least 1 h prior to beginning of testing. Between trials, mazes and apparatuses were cleaned with 70% ethanol. Muscimol, pentylenetetrazol and ANA-12 were purchased from Sigma-Aldrich (St. Louis, MO, USA). Ketamine hydrochloride was purchased from Yuhan (Seoul, Korea). Most of the behavioral tests were conducted as previously described(Bae et al. 2018), unless otherwise noted.

For tail suspension test (TST), mice were suspended by the tail from a metal hook extending from a steel bar using an adhesive tape in a 3-sided chamber with opaque walls. The distance between the floor of the chamber and the steel bar was approximately 40 cm. Mice that climbed onto their tail or fell off during the test were excluded from analysis. The duration of immobility over a 6-min session was manually scored by an experienced experimenter blind to treatment and mouse genotype.

Forced swim test (FST) was conducted by placing mice in glass

beakers (20 cm high, 15 cm in diameter) containing 25−26 ° C water at a 15−cm depth. An opaque plastic divider was placed between the glass beakers. Water was regularly changed and the beakers were cleaned between subjects. A mouse was judged to be immobile when it remained floating in the water without struggling or swimming and was only making minimum movements necessary to stay afloat. The total duration of immobility over the 6 min observation period was scored by an experimenter blinded to the experimental details.

Sucrose preference test was performed once daily for 3 days. Mice were deprived of water but not food for 12 h before each test and allowed to freely access to both water and 1% sucrose in individual cages for 12 h. The position of each bottle was switched daily to avoid false sucrose preference resulting from side bias. Volume of liquid consumed was determined by weighting the bottles. The preference (%) for sucrose solution was calculated as follows: (sucrose solution intake /total liquid intake) × 100%.

Open field test was conducted by placing in the center of an open field apparatus with opaque walls (40 × 40 × 40 cm) in a dimly lit room. The behavior of each mouse was monitored by video recording.

The total distance traveled and time spent in the entire open field and in the center (20 × 20 cm) were calculated using video tracking software (Ethovision XT, Noldus, Netherlands).

Elevated plus maze test was performed using a plus-shaped maze with two open arms and closed arms surrounded by opaque walls (20 cm in height). The maze was elevated 50 cm from the floor, and dimension of each arm was 5 cm wide and 30 cm in length. Each mouse was place in the center of the maze and movement of the mouse was video recorded for 5 min.

The elevated zero maze consisted of black acrylic in a circular track 5 cm wide, 60 cm in diameter, and elevated 50 cm from the floor. The maze was divided into four equal quadrants, two of which were enclosed with black acrylic walls (20cm in height). Each mouse was placed in the center of one of the two closed quadrants and movement of the mouse was video recorded for 5 min.

The Morris water maze test was performed using a white circular pool (120 cm in diameter) filled with 23° C-25° C water, which was made opaque with nontoxic white paint. A transparent circular platform (10 cm in diameter) submerged 1 cm beneath the surface. Two-day

pre-training sessions consisted of one trial per day, and each mouse was allowed to remain on the visible platform for 30 s. The mice were then trained to find the hidden platform for 7 days with four trials per day and inter-trial intervals of 1 min. In each trial, mice were released at one of the three starting points and allowed to find a submerged platform. If mice did not locate the platform within 90 s, they were manually placed on the platform by the experimenter. Mice remained on the platform for 30 s before subsequent trials or before being returned to home cages. The probe test was performed 1 d after the completion of the training sessions. Swim paths and quadrant occupancies of each mouse were analyzed using video tracking software (Ethovision XT, Noldus).

The accelerating rotarod test was performed using the Rotamex 5 equipment (Columbus Instruments, OH, USA). Mice were placed on motionless rods, which were then accelerated from 5 to 40 rpm over 5 min. The latencies to falling off the rotating rod were measured. Each mouse was trained once daily for 3 days.

Training sessions for contextual and cued fear conditioning consisted of a 300 s exploration period (Pre-CS, contextual), followed by the

presentation of an 18 s tone and a 2 s tone paired with a foot shock (0.7 mA) in the fear conditioning chamber (Coulbourn Instruments). Afterwards, each mouse was kept in the chamber for 60 s before being returned to its home cage. Contextual fear conditioning tests were performed in the same chamber (CS, contextual) 24 h after the training by monitoring mouse activity for 5 min. For cued fear conditioning, mice were placed in a distinct chamber, and their activities (pre-CS, cued) were monitored for 180 s, followed by presentation of a 180 s tone (CS, cued). The time spent freezing was scored post hoc by an experimenter blind to genotype.

Marble burying test was performed by placing animals individually in a transparent acrylic cage containing 15 clean glass marbles (1.5 cm in diameter) spaced evenly (3 × 5) on the surface of the 5-cm-deep bedding. Animals were allowed to explore the marbles for 10 min, and the number of marbles buried with bedding up to two-thirds of their surface area was counted.

Social behavior of animals was tested using the three-chambered social approach apparatus. The apparatus was white open-topped box (60 × 40 × 20 cm) and divided into three chambers (a 20-cm-wide

center chamber and 20-cm-wide side chambers) with two acrylic walls. Each of the two side chambers contained an empty wire cup. Dividing walls had retractable doorways that allowed access into each chamber. During the habituation phase, animals were placed in the center chamber and allowed to explore freely for 10 min. During the sociability phase, the animal was gently guided to the center chamber, and the two doors were blocked while a stranger C57BL/6 mouse (stranger 1) placed inside one of the wire cups and an inanimate object was placed inside the other wire cup. Then, the two doors were opened and the subject animal was allowed to explore all the three chambers for 10 min. The amount of time spent in each chamber and time spent exploring mice or objects were measured. For the social novelty test, the subject mice again gently guided to the center chamber, and the two doors were blocked while an inanimate object was replaced by a novel unfamiliar mouse (stranger 2). Afterwards, the two doors were opened and the subject animal again allowed to explore all three chambers for 10 min. The behavior of the animals was recorded and analyzed using video tracking software (Ethovision XT, Noldus). All stranger mice were males of the same age and previously habituated

to being enclosed in wire cups in the apparatus for 30 min one day before the test.

Pre-pulse inhibition (PPI) test was performed using the SR-Lab Startle Response system (San Diego Instruments, Ca, USA). Mice were placed into a small transparent tube mounted on a movement sensor platform in a sound-attenuating chamber and acclimated for 10 min before the testing session. The startle pulse was 120 dB (40 ms) and pre-pulses were either 75 or 80 dB (20 ms). During the acclimation period and each test session, background white noise (65 dB) was continuously presented. Baseline startle responses of animals were measured by 5-10 startle pulse (120 dB) alone trials, with inter-trial interval of 30 s. The peak startle amplitude was determined by measuring the largest positive and negative peaks of the startle response within a 300 ms window after the onset of the acoustic stimulus. During the PPI sessions, the same startle pulse preceded (100 ms) by a 75 dB or 80 dB pre-pulse in a pseudorandom order, with 5 testing trails per each pre-pulse. Scores for each measure were averaged, and PPI was calculated as a percent reduction of startle response: PPI (%) = (startle pulse alone - startle pulse with pre-

pulse) / startle pulse alone) × 100.

Chronic unpredictable stress

As previously reported(Yoon et al. 2014), I demonstrated that mice exposed to chronic unpredictable stress (CUS) showed increased immobility during tail suspension test. In brief, mice were exposed in a random order to a variety of chronic stressors, including a wet cage (12 h), light–dark cycle reversal (24 h), white noise (100 dB, 12 h), cold water swim (10 ° C, 1 h), restraint (2 h), cage shake (30 rpm, 12 h) and electric foot shocks (10 scrambled shocks with duration of 2 s over 120 min). Animals were subjected to one stressor daily for 28 days.

Constructs and virus preparation

For Gabrg2 knockdown assay, Gabrg2 cDNA was amplified from mouse hippocampal cDNA and was cloned into pGW1 vector. Four independent shRNA (#1: gcattggaagctcagtctactctcctgta; #2: tggaatgatggtcgagttctctacacctt; #3: ccaaggtctcctatgtcacagcaatggat; #4:

tggattgaggaatacaactgaagtagtga) constructs in the pGFP-V-RS vector and a non-targeting (NT: gcactaccagagctaactcagatagtact) pGFP-V-RS plasmid were purchased from OriGene (Cat. # TL515175). For lentivirus-mediated expression, the cassettes containing the human U6 (hU6) promoter-shRNA#3 and hU6-NT were amplified by PCR, and then subcloned into the pLVX-DsRed-Monomer-C1 (Clontech) vector, displacing the CMV promoter-DsRed-Monomer cassette. The PGK promoter-puromycin resistance gene cassette in the vector was further replaced by the CMV-eGFP cassette from the pEGFP-C1 vector (Clontech). The sequence-verified plasmid was transfected into Lenti-X 293T cells (Takara Bio) together with the packaging plasmid psPAX2 (Addgene) and the envelope plasmid pMD2.G (Addgene) using a polyethylenimine (PEI)-based transfection protocol (total DNA to PEI μg ratio of 1: 2). The ratio of pLVX-shRNA: psPAXs: pMD2.G was 4:1:2 (total 300 μg / 245 mm square dish). Lenti-X 293T cells were cultivated in the high glucose (4.5 g/L) Dulbecco's Modified Eagle's Medium (DMEM) containing 4 mM L-glutamine, 3.7 g/L sodium bicarbonate, 10% (v/v) tetracycline-free fetal bovine serum (FBS), 1 mM sodium pyruvate, and 1% (v/v)

penicillin/streptomycin. The medium was replaced with fresh medium 24 h after transfection. Lentivirus-containing medium was harvested 72 h after transfection and was briefly centrifuged at 900 g for 10 min to remove debris. Supernatant was filtered (0.45-μm pore size) for sterilization, and lentivirus particles were concentrated by 2 rounds of ultracentrifugation (10,000 g for 2 h). Pellets were resuspended in PBS, aliquoted and stored at -80 ° C. Viral titer (10^{12-13} IU/mL) was determined by transfecting serially diluted virus stocks into HEK293T cells and analyzing the number of GFP-positive cells using a fluorescence-activated cell sorter (FACS).

AAV2/hSyn-DIO-mCherry (#50459), AAV2/hSyn-DIO-hM3Dq-mCherry (#44361) and AAV2/hSyn-DIO-hM4Di-mCherry (#44362) were obtained from Addgene (Watertown, MA, USA). AA2/SST-Cre (#CV17210-AV2) was purchased from Vigene Biosciences (Rockville, MD, USA).

Surgery and stereotaxic injection

Under deep anesthesia with a mixture of Zoletil (50 mg/kg, i.p) and

Xyalazine (1 mg/kg, i.p), mice were placed in a stereotaxic device. The skin was cut over the midline and craniotomies were performed bilaterally over the hippocampus. Either purified AAV (0.5 μL/side) or lentivirus (1 μL/side) was injected into the CA1 region of the dorsal medial hippocampus (−1.9 anteroposterior, ±1.5 mediolateral, −1.8 dorsoventral from the Bregma) using a Hamilton syringe at a rate of 100 nL/min. After completion of injection, the needle (33 gauge) was remained in place for an additional 10 min to allow the diffusion of the injection medium, and then carefully retracted to prevent backflow. Experiments were performed 3−4 weeks after viral injections.

For intrahippocampal infusion of muscimol, cannula assemblies consisted of a stainless−steel guide cannula (26 gauge with 2 mm) and a stylet were bilaterally implanted into the dorsal medial hippocampus (−1.9 anterior/posterior, ±1.5 medial/lateral, −1.2 dorsal/ventral) and were affixed to the skull with dental cement. Following surgery, mice were allowed to recover for at least 10 days before microinjection. Intrahippocampal infusion (0.5 μL/side) was made using a syringe pump (Harvard Apparatus, Pump 11) at a rate of 100 nL/min. Stainless steel injection cannulas connected to the injection syringe by

polyethylene tubing were inserted into the guide cannulas. Following microinjection, the injection cannulas were remained in place for 5 min to allow diffusion of the solution into the tissue and then replaced by stylets.

Electrophysiology

Parasagittal hippocampal slices (400 μm thick) were prepared using a vibratome (Leica, Germany) in ice-cold dissection buffer (sucrose 230 mM; $NaHCO_3$ 25 mM; KCl 2.5 mM; NaH_2PO_4 1.25 mM; D-glucose 10 mM; Na-ascorbate 1.3 mM; $MgCl_2$ 3 mM; $CaCl_2$ 0.5 mM, pH 7.4 with 95% O_2/5% CO_2). Immediately after sectioning, the CA3 region was surgically isolated. The slices were allowed to recover at 36 °C for 1 h in normal artificial cerebrospinal fluid (ACSF: NaCl 125 mM; $NaHCO_3$ 25 mM; KCl 2.5 mM; NaH_2PO_4 1.25 mM; D-glucose 10 mM; $MgCl_2$ 1.3 mM; $CaCl_2$ 2.5 mM, pH 7.4 with 95% O_2/5% CO_2), and then maintained at room temperature.

All electrophysiological recordings were performed in a submerged recording chamber, which was perfused with heated (29-30°C) ACSF.

The signals were filtered at 2.8 kHz and digitized at 10 kHz using a MultiClamp 700B amplifier and a Digidata 1440A interface (Molecular Devices, CA, USA). Data were analyzed by using custom macros written in Igor Pro (WaveMetrics, OR, USA).

Miniature EPSCs (mEPSCs) were measured at −70 mV with a pipette solution containing (in mM) 110 K−gluconate, 20 KCl, 8 NaCl, 10 HEPES, 0.5 QX−314−Cl, 4 Mg−ATP, 0.3 Na−GTP, and 10 BAPTA, adjusted to pH 7.25 and 290 mOsm/kg. Spontaneous action potentials and IPSCs were blocked by tetrodotoxin (TTX, 1 μM) and picrotoxin (50 μM), respectively. For miniature IPSC (mIPSC) recording, K−gluconate in the pipette solution was replaced by equimolar KCl, and currents were measured at −70 mV in the presence of TTX (1 μM), NBQX (10 μM), and AP−5 (50 μM) in ACSF.

To measure evoked EPSC/IPSC ratio (Figs. 1 and 3), whole−cell voltage clamp recordings were made using patch pipettes (3–4 MΩ) filled with solution containing (in mM) 130 CsMeSO4, 10 TEA−Cl, 10 HEPES, 4 Mg−ATP, 0.3 Na−GTP, 5 QX−314−Cl and 10 EGTA, adjusted to pH 7.25 and 290 mOsm/kg. The synaptic responses were evoked at 0.05 Hz with an ACSF−filled broken glass pipette (0.3–0.5

MΩ) placed in the proximal region of the stratum radiatum. The mean AMPAR-mediated EPSCs were obtained by averaging 30-40 traces recorded at -57 mV. Stimulation intensity was adjusted to yield a 100-300 pA EPSC peak amplitude. To isolate the $GABA_AR$-mediated currents, 30-40 traces of synaptic currents were recorded at +3 mV. To examine the effect of PTZ on inhibitory synaptic transmission (Fig. 6), evoked IPSCs were measured at a holding potential of -70 mV with the same pipette solution used for the measurement of mEPSCs. NBQX (10 μM) and AP-5 (50 μM) were added to the ACSF throughout recordings to block AMPAR- and NMDAR-mediated EPSCs, respectively. The series resistance and seal resistance were monitored, and data were discarded if they changed by more than 20% during recordings.

The membrane potentials were recorded under whole-cell current clamp mode with a pipette solution containing (in mM) 110 K-gluconate, 20 KCl, 8 NaCl, 10 HEPES, 4 Mg-ATP, 0.3 Na-GTP, and 0.5 EGTA, adjusted to pH 7.25 and 290 mOsm/kg. Neurons displaying an unstable resting potential at the beginning or during the recording were discarded.

All reagents were purchased from Sigma-Aldrich (MO, USA), except for QX-314-Cl, CNO, NBQX, AP-5 from Tocris (Bristol, UK).

Immunohistochemistry and western blotting

Immunohistochemistry and western blotting analyses were performed as described previously (Bae et al. 2018). Briefly, mice were deeply anesthetized with diethyl ether and transcardially perfused with heparinized (10 U/mL) phosphate-buffered saline (PBS), followed by PBS-buffered 4% (w/v) paraformaldehyde (PFA). Brains were removed, post-fixed in 4% PFA for 48 h at 4 °C and cut into 60 μm coronal sections using a vibratome (VT1200S, Leica, Germany). The sections were post-fixed (1 h), permeabilized with 0.3% (v/v) Triton X-100 in PBS, incubated in blocking buffer (5% normal goat serum, 5% horse serum, 5% donkey serum, and 0.5% BSA in PBS) for 2 h. Sections were successively incubated with primary [anti-PV: Swant, (Cat. # PV27) and Millipore (Cat. # MAB1572); anti-SST: Santa Cruz Biotechnology (Cat. # sc-55565); anti-VIP: Immunostar (Cat. # 20077); anti-CCK: Abcam (Cat. # ab37274); anti-GAD67: Millipore (Cat. # MAB5406); anti-mCherry: Abcam (Cat. # ab167453); anti-

GFP: Synaptic Systems (Cat. # 132 004); anti-c-Fos: Cell Signaling Technology (Cat. # 2250S); anti-NeuN: Millipore (Cat. # ABN78 and Cat. # MAB377); overnight at 4 ° C] and fluorescence (Cy3, Alexa fluor 647 or FITC: Jackson ImmunoResearch Laboratories, PA, USA) conjugated-secondary (3 h at room temperature) antibodies. Between each step, the sections were rinsed 3 times for 10 min with PBS. Images were acquired using an FV 3000 confocal laser scanning microscope and processed with FV31S-SW Viewer (Olympus, Japan). Wide-field images of entire brain sections were acquired using a TCS SP8 confocal microscope and Leica Application Suite X (Leica, Germany).

For western blotting, mouse hippocampi were homogenized in buffer (320 mM sucrose, 10 mM Tris-HCl, 5 mM EDTA, pH 7.4) containing phosphatase inhibitor cocktail (GenDEPOT, TX, USA, Cat. # P3200) and proteinase inhibitor cocktail (Sigma-Aldrich, MO, USA, Cat. # P8340). Proteins were separated by SDS-PAGE and transferred to nitrocellulose membranes. The membranes were successively incubated with primary and horseradish peroxidase (HRP)-conjugated secondary (Jackson ImmunoResearch Laboratories, PA, USA)

antibodies. Signals were detected by enhanced chemiluminescence (GE Healthcare, UK) and quantified using MetaMorph software (Molecular Devices, CA, USA). The following primary antibodies were obtained from commercial suppliers: anti-ERK (Cat. # 9102S), anti-p-ERK (Cat. # 9106S), anti-eEF2 (Cat. # 2332S), anti-p-eEF2 (Cat. # 2331S), anti-mTOR (Cat. # 2972S), anti-p-mTOR (Cat. # 2971S) from Cell Signaling Technology; BDNF (Cat. # ab108319) from Abcam; Gabrg2 (Cat. # 224 003) from Synaptic Systems; tGFP (Cat. # TA150041) from Origene; α-tubulin (Cat. # T5168) from Sigma-Aldrich.

Electroencephalogram (EEG) recording

EEG surgeries and recordings were performed as previously described(Bae et al. 2018). Mice (7-9 weeks old) were anesthesized with 1.5% isoflurane. The skin was incised over the midline, and four epidural electrodes were bilaterally anchored into the frontal and temporal regions of the skull (frontal: +2.0 mm anteroposterior, ±1.0 mm mediolateral; temporal: -2.3 mm anteroposterior, ±2.0 mm mediolateral). A reference electrode was placed in the occipital region

of the skull (−4.2 mm anteroposterior). All connectors were fixed to the skull using dental cement. Mice were allowed to recover from surgery for 7–10 days. EEG signals and video recordings were simultaneously acquired for 30 min. Mice of both sexes (+/+: three males and two females; −/−: four males and two females) were used for EEG recordings, and sex differences were not observed. EEG signals were amplified (Digital Lynx acquisition system and Cheetah software, Neuralynx) and digitized at a sampling rate of 32 kHz. The data were analyzed using Neuroexplorer (Nex Technologies). Representative spectrograms and traces were obtained using Neuroexplorer and custom macros written in Igor Pro (WaveMetrics, OR, USA), respectively.

Statistical analysis

Statistical analyses were performed using Igor Pro (WaveMetrics) and SPSS (IBM, Armonk, USA). The normality of the collected data was determined using the Shapiro−Wilk test and Mauchly's sphericity test. The Mann−Whitney test was used to compare non−normally distributed samples. Samples that satisfied normal distribution were

compared using two-tailed Student's t-tests. For multiple groups, one-way ANOVA, followed by with Tukey's HSD (Honestly Significant Difference) post-hoc test was used to compare samples. For Morris water maze training experiment, repeated two-way ANOVA, followed by Bonferroni's post-hoc test was used to compare samples. All bar graphs in the figures show the mean ± standard error of the mean (SEM). The levels of significance are indicated as follows: $*P < 0.05$, $**P < 0.01$, $***P < 0.001$, n.s., not significant ($p \geq 0.05$).

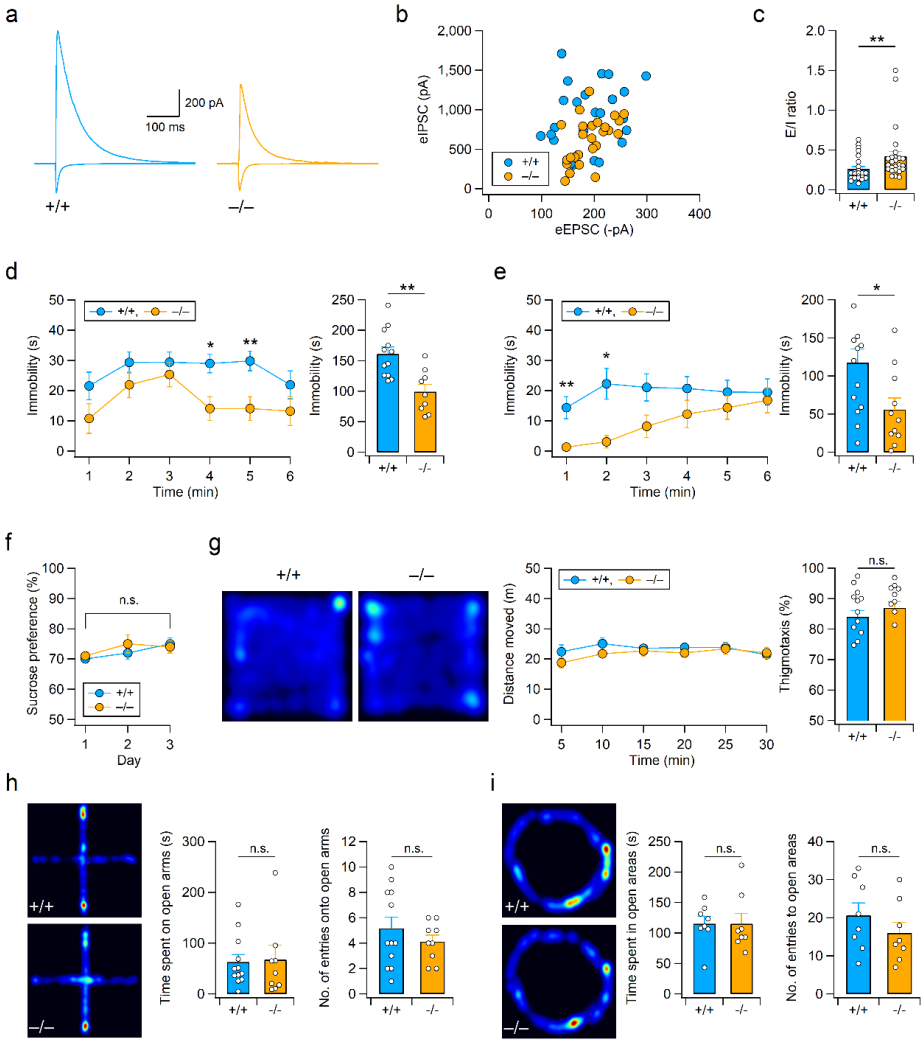
a
200 pA
100 ms
+/+
–/–
b
eIPSC (pA)
eEPSC (-pA)
+/+
–/–
c
E/I ratio
**
+/+
-/-
d
Immobility (s)
Time (min)
+/+, –/–
*
**
Immobility (s)
**
+/+
-/-
e
Immobility (s)
Time (min)
+/+, –/–
**
*
Immobility (s)
*
+/+
-/-
f
Sucrose preference (%)
n.s.
Day
+/+
–/–
g
+/+
–/–
Distance moved (m)
Time (min)
+/+, –/–
Thigmotaxis (%)
n.s.
+/+
-/-
h
+/+
–/–
Time spent on open arms (s)
n.s.
+/+
-/-
No. of entries onto open arms
n.s.
+/+
-/-
i
+/+
–/–
Time spent in open areas (s)
n.s.
+/+
-/-
No. of entries to open areas
n.s.
+/+
-/-

Figure 2. RalBP1$^{-/-}$ mice display decreased synaptic inhibition and anti-despair-like behaviors but normal anxiety levels.

(a-c) Enhanced excitation-inhibition (E/I) ratio in RalBP1$^{-/-}$ CA1 pyramidal neurons. (a) Representative traces (average of 15 consecutive sweeps) of evoked EPSCs (downward deflections at −57 mV) and IPSCs (upward deflections at +3 mV) recorded in CA1 pyramidal neurons from WT (RalBP1$^{+/+}$) and RalBP1$^{-/-}$ mice. (b) The mean amplitude of evoked IPSCs measured in each cell was plotted against the mean amplitude of EPSCs. (c) The E/I ratios are significantly increased in RalBP1$^{-/-}$ mice. (d, e) RalBP1$^{-/-}$ mice display anti-despair-like behavior. (d) Immobility time of mice was measured every 1 min during the TST (left). Total time spent immobile over 6 min in the TST (right). (e) Forced swimming test (FST) of RalBP1$^{+/+}$ and RalBP1$^{-/-}$ mice (left). RalBP1$^{-/-}$ mice spent significantly less time immobile during the 6-min FST (right). (f) Sucrose preference during the 3-day-sucrose-consumption test is unaltered in RalBP1$^{-/-}$ mice. (g-i) Normal anxiety levels and locomotor activity in RalBP1$^{-/-}$ mice. (g) Representative activity paths (left), distance moved (middle), and the thigmotaxis (a tendency to remain close to walls) levels (right) in the open-field test. (h) Representative activity traces (left), time

spent in the open arms (middle), and the number of open-arm entries (right) of WT and RalBP1$^{-/-}$ mice in the elevated plus maze test. (i) Representative activity traces (left), time spent in the open areas (middle), and the number of entries into open areas (right) of WT and RalBP1$^{-/-}$ mice in the elevated zero-maze test.

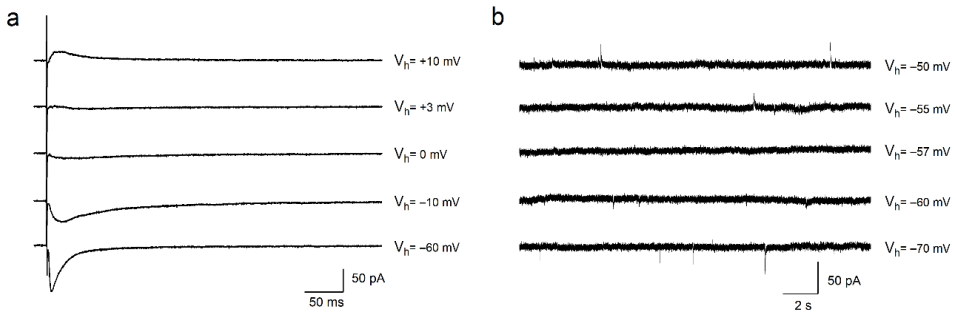

Figure 3. Determination of the reversal potentials for EPSCs and IPSCs in CA1 pyramidal neurons.

(a) Sample traces of evoked EPSCs in the presence of the GABAAR blocker picrotoxin in the bathing solution. The holding potentials (Vh) are shown with each trace. Recording at +3 mV leads to negligible evoked EPSCs owing to the absence of a driving force for cations. (b) Example traces of spontaneous IPSCs recorded from CA1 pyramidal neurons in the presence of the AMPAR blocker NBQX and NMDAR blocker AP−5. The reversal potential of spontaneous IPSCs was −57 mV.

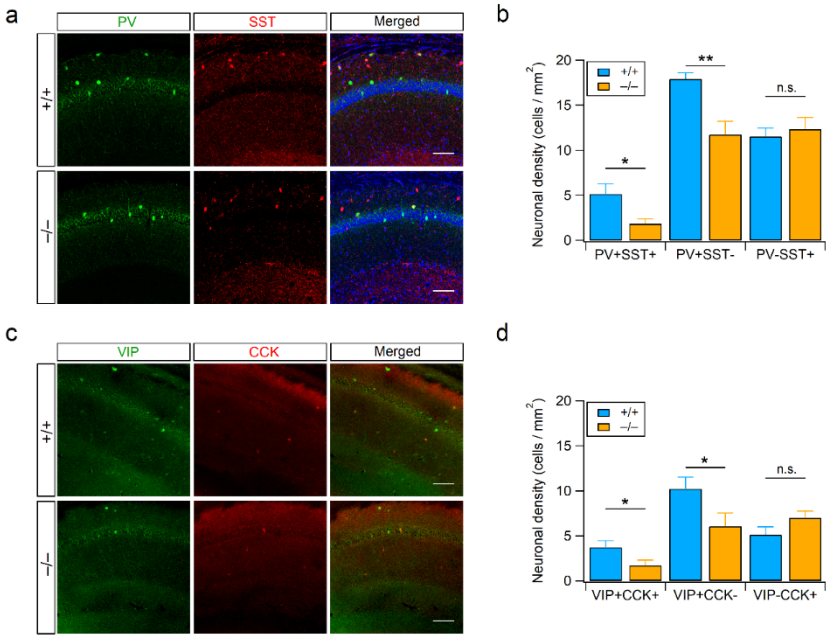

Figure 4. RalBP1$^{-/-}$ mice exhibit fewer interneurons in the hippocampus.

(a) Immunohistochemical staining for parvalbumin (PV) and somatostatin (SST) in the WT and RalBP1$^{-/-}$ hippocampal CA1 areas. DAPI (blue) was used to visualize cell nuclei (right). (b) Quantification of PV− and/or SST−expressing neurons in the hippocampal CA1 area. (c) Immunostainings for vasoactive intestinal peptide (VIP) and cholecystokinin (CCK) are shown. (d) Quantification of VIP− and/or CCK−expressing neurons in the hippocampal CA1 area. (a and c) Scale bars, 100 μm.

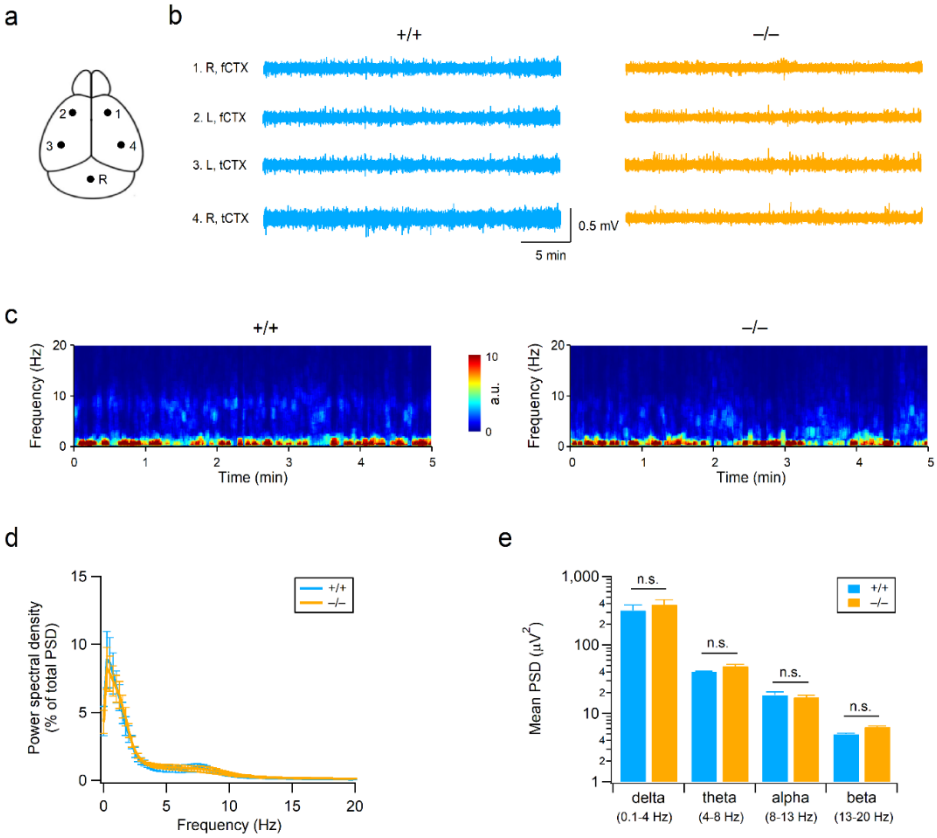
a
b
+/+
–/–
1. R, fCTX
2. L, fCTX
3. L, tCTX
4. R, tCTX
0.5 mV
5 min
c
Frequency (Hz)
Time (min)
a.u.
d
Power spectral density (% of total PSD)
Frequency (Hz)
e
Mean PSD (µV²)
n.s.
delta (0.1-4 Hz)
theta (4-8 Hz)
alpha (8-13 Hz)
beta (13-20 Hz)

Figure 5. Normal electroencephalogram (EEG) rhythms in RalBP1$^{-/-}$ mice.

(a) Diagram showing the placement of epidural electrodes in the mouse brain. R, reference electrode. (b) Sample EEG traces of RalBP1$^{+/+}$ (left) and RalBP1$^{-/-}$ (right) mice recorded for 30 min from four epidural electrodes in their homecages. No epileptic activity was observed in both genotypes. R, right; L, left; fCTX, frontal cortex; tCTX, temporal cortex. (c) Time−frequency plots of EEG waves recorded in the right temporal region of the control (left) and RalBP1$^{-/-}$ (right) brain. (d) Frequency characteristics of EEG traces recorded for 30 min in the right temporal region of RalBP1$^{+/+}$ and RalBP1$^{-/-}$ mice were calculated by fast Fourier transformation. (e) The average power spectral density of delta, theta, alpha, and beta rhythms calculated from RalBP1$^{+/+}$ (N = 5) and RalBP1$^{-/-}$ (N = 6) mice. n.s., not significant, $P > 0.05$ by Student's t−test.

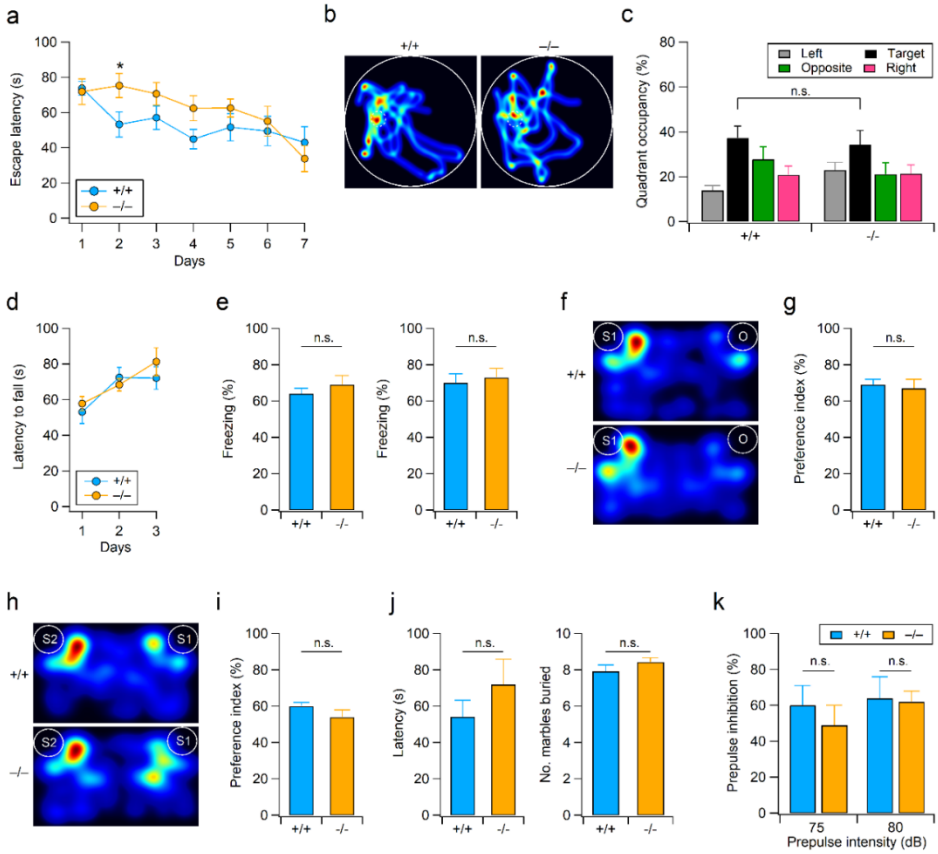
a
Escape latency (s)
Days
+/+
–/–
b
+/+
–/–
c
Quadrant occupancy (%)
Left
Target
Opposite
Right
n.s.
+/+
-/-
d
Latency to fall (s)
Days
e
Freezing (%)
n.s.
f
S1
O
g
Preference index (%)
h
S2
S1
i
Preference index (%)
j
Latency (s)
No. marbles buried
k
Prepulse inhibition (%)
Prepulse intensity (dB)
75
80

Figure 6. Normal learning, social interaction and sensory gating in RalBP1$^{-/-}$ mice.

(a–e) Intact hippocampus–dependent learning in RalBP1$^{-/-}$ mice. (a) The escape latencies were averaged from 4 trials on each day during the Morris water maze training. *$P < 0.05$ by Student t–test. (b) Representative swim paths of mice during the probe trials (60 s) after completion of 7 days of training. (c) The percentage of time spent in each quadrant during the probe trials. (d) RalBP1$^{-/-}$ mice display normal motor coordination and motor learning. The latencies to falling from the accelerating rotarod are plotted against the training days. (e) Quantification of context–specific (left) and cue–specific (right) freezing behaviors measured 24 h after the fear conditioning training. (f–i) Normal social approach and social novelty recognition in RalBP1$^{-/-}$ mice. (f) Representative activity traces of WT (top) and RalBP1$^{-/-}$ (bottom) mice during the three–chamber social approach test. (g) Both genotypes spent more time in the social chamber containing a stranger mouse (S1) than the chamber containing an inanimate object (O). Preference index (%) = Time sniffing the stranger / (Time spent sniffing the stranger + Time spent sniffing the object) × 100. (h) Representative heat maps show the location of WT (top) and RalBP1$^{-/-}$

(bottom) mice during the social novelty recognition test. (i) Quantification preference for a new stranger mouse (S2). Preference index (%) = Time spent sniffing the new stranger (S2) / (Time spent sniffing the new stranger (S2) + Time spent sniffing the familiar (S1)) × 100. (j) Latency (left) to start marble burying and the number (right) of marble buried by WT and RalBP1$^{-/-}$ mice are summarized. (k) Prepulse inhibition (PPI) of acoustic startle response at two different prepulse intensities (75 and 80 dB).

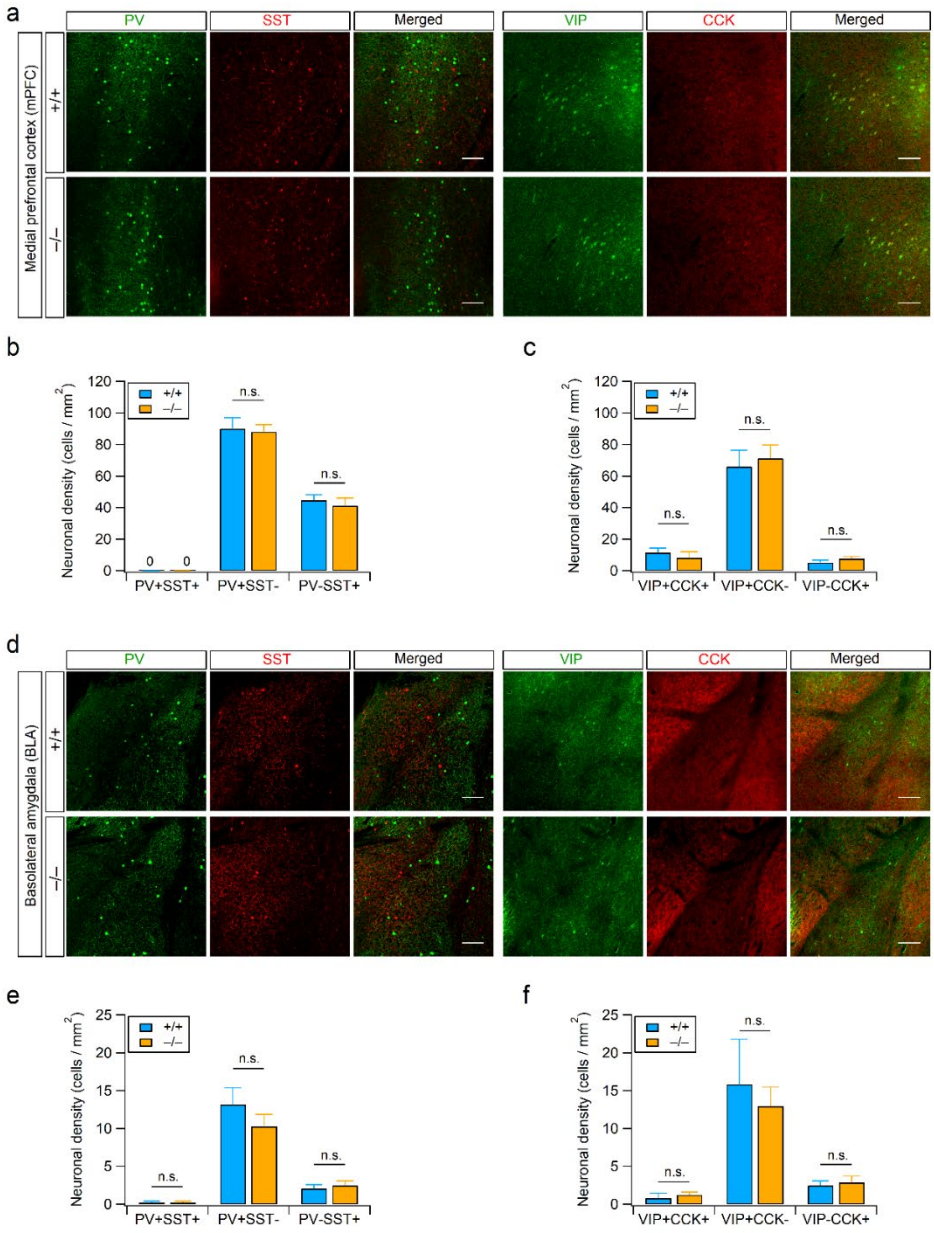
a
PV
SST
Merged
VIP
CCK
Merged
Medial prefrontal cortex (mPFC)
+/+
−/−
b
Neuronal density (cells / mm²)
+/+
−/−
n.s.
0
PV+SST+
PV+SST-
PV-SST+
c
VIP+CCK+
VIP+CCK-
VIP-CCK+
d
Basolateral amygdala (BLA)
e
f

Figure 7. Normal density of interneurons in the RalBP1$^{-/-}$ medial prefrontal cortex (mPFC) and basolateral amygdala (BLA).

(a) Immunohistochemical staining for parvalbumin (PV), somatostatin (SST), vasoactive intestinal peptide (VIP) and cholecystokinin (CCK) in the mPFC from WT and RalBP1$^{-/-}$ mice. (b) RalBP1$^{-/-}$ mice exhibit normal population of PV and SST neurons in the mPFC. (c) Quantification of VIP− and/or CCK−expressing neurons in the mPFC. (d) The distributions of PV, SST, VIP and CCK were examined by immunohistochemistry in the BLA from WT and RalBP1$^{-/-}$ mice. (e) Neurons expressing PV and/or SST in the BLA are unaltered by RalBP1 mutation. (f) Quantification of VIP− and/or CCK−positive neurons in the BLA. (a and d) Scale bars, 100 μm.

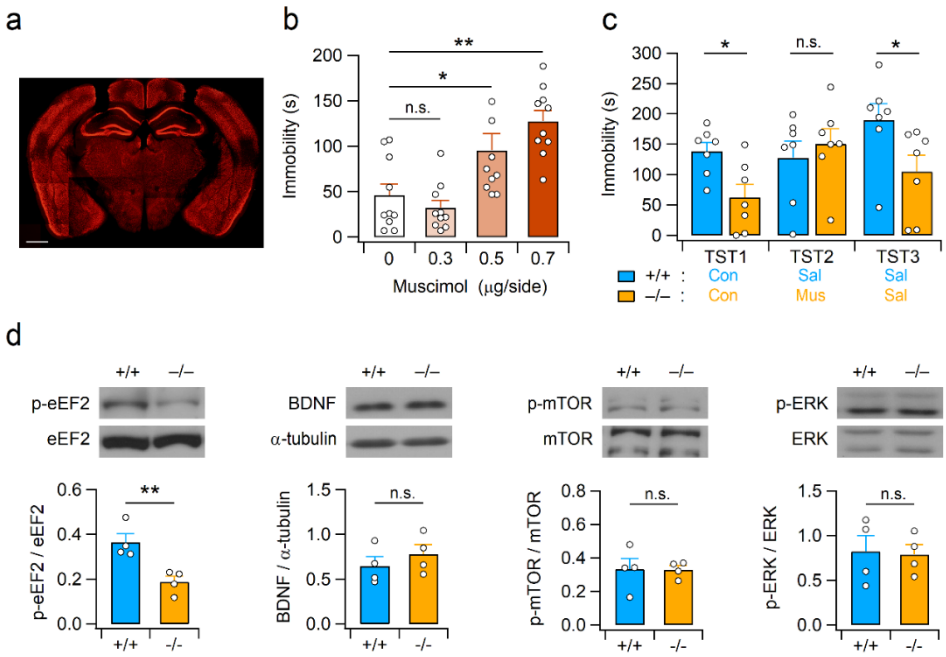
a
b
Immobility (s)
200
150
100
50
0
**
*
n.s.
0
0.3
0.5
0.7
Muscimol (μg/side)
c
Immobility (s)
300
250
200
150
100
50
0
*
n.s.
*
TST1
TST2
TST3
+/+ : Con Sal Sal
–/– : Con Mus Sal
d
+/+
–/–
p-eEF2
eEF2
BDNF
α-tubulin
p-mTOR
mTOR
p-ERK
ERK
p-eEF2 / eEF2
0.6
0.4
0.2
0.0
**
BDNF / α-tubulin
1.5
1.0
0.5
0.0
n.s.
p-mTOR / mTOR
0.8
0.6
0.4
0.2
0.0
n.s.
p-ERK / ERK
1.5
1.0
0.5
0.0
n.s.
+/+
-/-

Figure 8. Attenuation of anti-despair-like behavior by intrahippocampal infusion of muscimol and altered hippocampal eEF2 signaling in RalBP1$^{-/-}$ mice.

(a) Representative image showing the cannula placement in the mouse brain for muscimol infusion. The section was immunostained with anti-NeuN antibodies. Scale bar, 1 mm. (b) Hippocampal infusion of muscimol increases TST immobility time in a dose-dependent manner. (c) Potentiation of GABAergic transmission in the hippocampal CA1 area reverts the anti-despair-like behavior of RalBP1$^{-/-}$ mice. TST was performed 30 min after completion of infusion and inter-test intervals were 2 days. Con, Sal, and Mus represent no infusion, saline infusion, and muscimol infusion, respectively. (d) Representative western blot images (top) and quantification (bottom) showing enhanced eEF2 activation but normal BDNF, mTOR, and ERK signaling in the RalBP1$^{-/-}$ hippocampus. Western blotting using anti-α-tubulin antibody was performed to ensure equal protein loading and transfer, and quantification of BDNF levels in each sample.

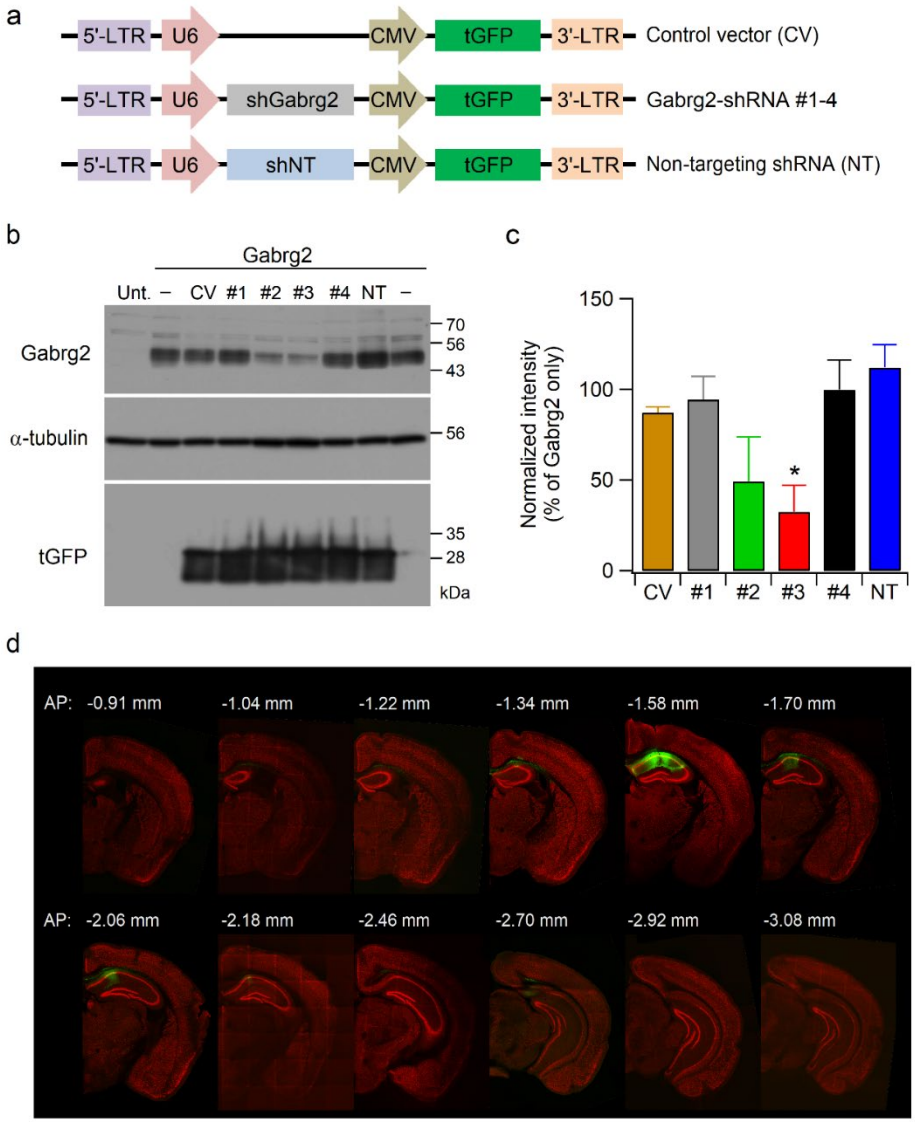
a
5'-LTR
U6
CMV
tGFP
3'-LTR
Control vector (CV)
shGabrg2
Gabrg2-shRNA #1-4
shNT
Non-targeting shRNA (NT)
b
Gabrg2
Unt. – CV #1 #2 #3 #4 NT –
Gabrg2
α-tubulin
tGFP
70
56
43
56
35
28
kDa
c
Normalized intensity
(% of Gabrg2 only)
150
100
50
0
*
CV #1 #2 #3 #4 NT
d
AP: -0.91 mm
-1.04 mm
-1.22 mm
-1.34 mm
-1.58 mm
-1.70 mm
AP: -2.06 mm
-2.18 mm
-2.46 mm
-2.70 mm
-2.92 mm
-3.08 mm

Figure 9. Efficiencies of Gabrg2 knockdown in HEK293T cells and lentivirus infection in the CA1 area of the mouse brain.

(a–c) Western blot analysis of Gabrg2 knockdown efficiencies of four different shRNA sequences (sh#1–4) in HEK293T cells. (a) Schematic representation of the shRNA constructs. (b) Representative western blots for Gabrg2, α–tubulin and TurboGFP (tGFP) obtained from HET293T cell lysates at 72 h post–transfection. Control vector (CV) expresses tGFP without a hairpin sequence. The non–targeting (NT) shRNA contains a tGFP expression cassette and the hairpin with surrounding sequences that do not overlap with any known mouse gene (see Methods for details). α–tubulin and tGFP were used as loading and transfection controls, respectively. Unt., untransfected control HEK293T cells. (c) Quantification of the Gabrg2 knockdown efficiency in transfected cell lines. (d) Series of immunofluorescent images of coronal sections co–stained with eGFP (green) and NeuN (red) show the distribution of lentivirus–infected cells (green) in the mouse brain. Numbers indicate anterior/posterior (AP) coordinates to Bregma.

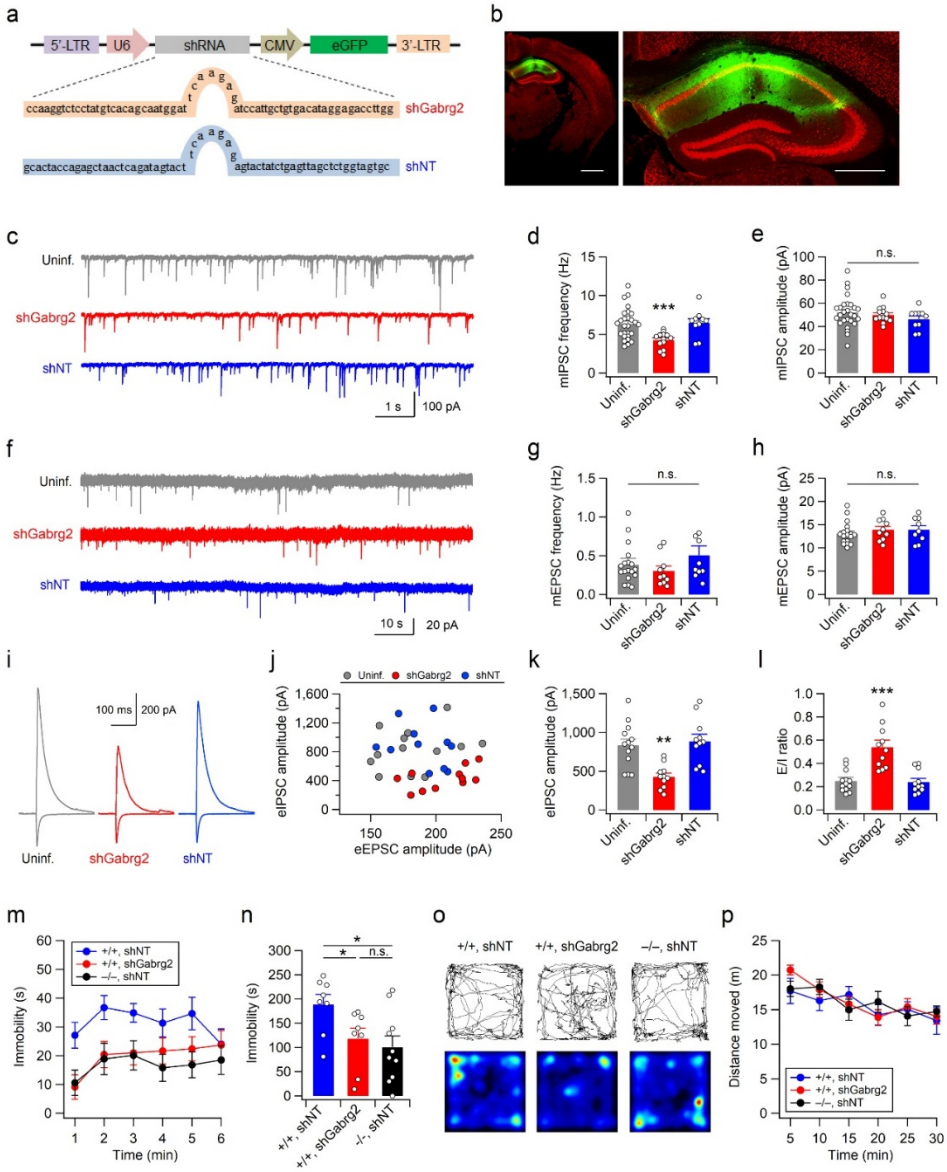
a
5'-LTR
U6
shRNA
CMV
eGFP
3'-LTR
ccaaggtctcctatgtcacagcaatggat
atccattgctgtgacataggagaccttgg
shGabrg2
gcactaccagagctaactcagatagtact
agtactatctgagttagctctggtagtgc
shNT
b
c
Uninf.
shGabrg2
shNT
1 s
100 pA
d
mIPSC frequency (Hz)
***
e
mIPSC amplitude (pA)
n.s.
f
10 s
20 pA
g
mEPSC frequency (Hz)
h
mEPSC amplitude (pA)
i
100 ms
200 pA
j
eIPSC amplitude (pA)
eEPSC amplitude (pA)
k
**
l
E/I ratio
m
Immobility (s)
Time (min)
+/+, shNT
+/+, shGabrg2
–/–, shNT
n
*
n.s.
o
p
Distance moved (m)

Figure 10. Knockdown of Gabrg2 in hippocampal CA1 neurons reduces despair-like behaviors.

(a) Schematic diagram of the viral genome expressing Gabrg2-shRNA#3 (shGabrg2) or non-targeting shRNA (shNT). (b) Coronal brain section from mice expressing eGFP (green) in the hippocampal CA1 area (left). Sections were co-stained with the neuronal marker NeuN (red). Right, enlarged image of the hippocampal area. Scale bars, 1 mm (left) and 500 μm (right). (c) Sample traces of mIPSCs recorded in CA1 pyramidal neurons infected with virus expressing shGabrg2 or NT, and nearby uninfected (uninf.). (d) Gabrg2 knockdown reduces the frequency of mIPSCs. (e) Summary of the mean amplitudes of mIPSCs obtained from uninfected and virus-infected (shGabrg2 or shNT) CA1 neurons. (f-h) Gabrg2 knockdown does not affect mEPSCs. Sample traces (f), mean frequencies (g) and mean amplitudes (h) of mEPSCs recorded in CA1 pyramidal neurons infected with virus expressing shGabrg2 or NT, and nearby uninfected. (i) Representative traces of evoked IPSCs (upward deflections at +3 mV) and EPSCs (downward deflections at −57 mV) recored from CA1 pyramidal neurons. (j) The peak amplitudes of IPSCs are plotted against peak EPSC amplitudes. (k, l) Summary of peak eIPSC amplitudes (k) and the excitation-inhibition

(E/I) ratios (l) in the CA1 pyramidal neurons infected with virus expressing shGabrg2 or NT, and nearby uninfected. (m) shRNA-mediated suppression of Gabrg2 expression in hippocampal CA1 neurons reduces immobility of mice in the TST. (n) Summary of time spent immobile in each experimental group during the 6-min TST. (o) Representative images showing exploration path during the first 5 min (top) and entire 30-min period (bottom) in the open field test. (p) Quantification of distance moved in the open field box.

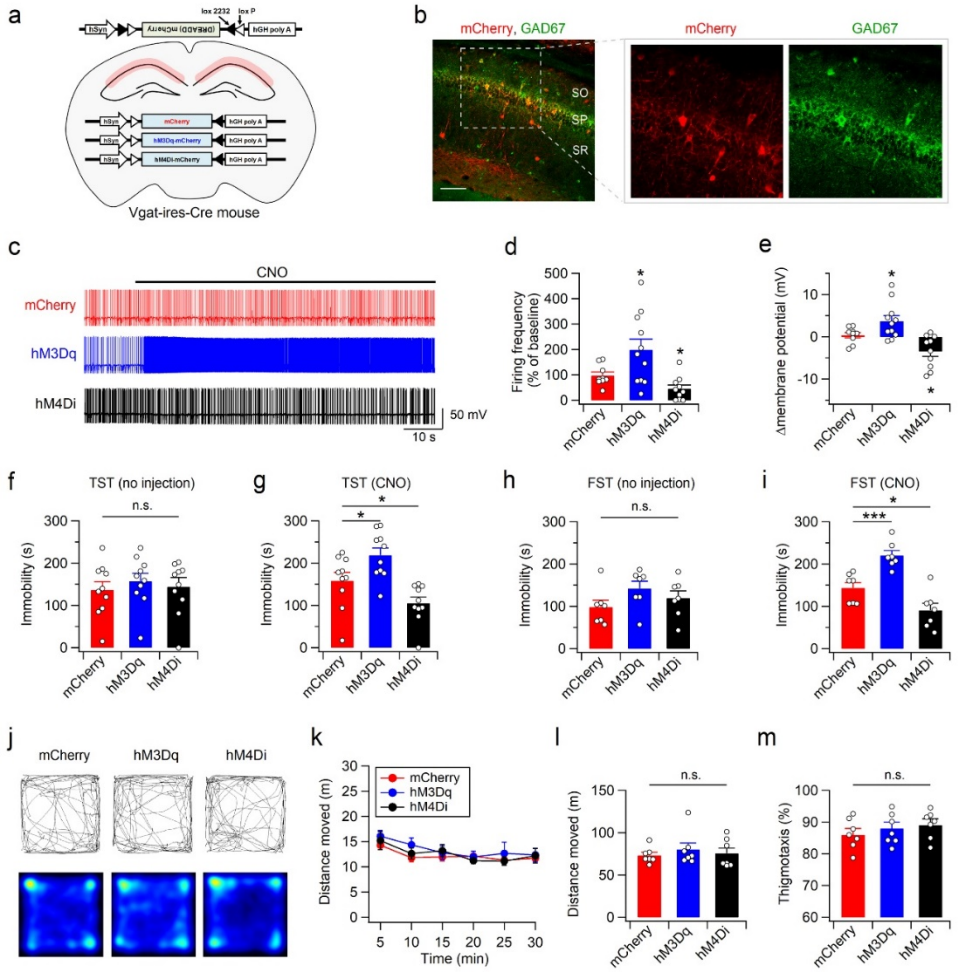
a
hSyn
(DREADD) mCherry
hGH poly A
lox 2232
lox P
mCherry
hM3Dq-mCherry
hM4Di-mCherry
Vgat-ires-Cre mouse
b
mCherry, GAD67
mCherry
GAD67
SO
SP
SR
c
CNO
mCherry
hM3Dq
hM4Di
50 mV
10 s
d
Firing frequency (% of baseline)
mCherry
hM3Dq
hM4Di
e
Δmembrane potential (mV)
f
TST (no injection)
n.s.
Immobility (s)
g
TST (CNO)
h
FST (no injection)
i
FST (CNO)
j
mCherry
hM3Dq
hM4Di
k
Distance moved (m)
Time (min)
l
m
Thigmotaxis (%)

Figure 11. Pharmacogenetic manipulation of CA1 interneurons alters behavioral despair.

(a) Design of Cre-dependent expression of mCherry, hM3Dq-mCherry or hM4Di-mCherry in the CA1 interneurons. (b) Double immunostaining of hippocampal sections with mCherry (red) and GAD67 (green) antibodies reveals interneuron-specific expression of mCherry in the CA1 subfield of Vgat-Cre mice. Scale bar, 100 μm. SO, stratum oriens; SP, stratum pyramidale; SR, stratum radiatum. (c) Representative voltage traces recorded from interneurons expressing mCherry, hM3Dq-mCherry, or hM4Di-mCherry before and during the bath application of CNO (5 μM). (d) Quantification of the CNO effects on firing rate. The firing rates under CNO are expressed as a percentage of baseline (absence of CNO) values. (e) Changes in membrane potential in response to CNO application are summarized. (f-i) Bar graphs represent total time spent immobile during the TST (f, g) and FST (h, i). In the absence of CNO, DREADD expression does not affect despair-like behaviors in the TST (f) and FST (h). CNO-induced activation or suppression of CA1 interneurons expressing DREADDs bidirectionally modifies immobility time in the TST (g) and FST (i). CNO was administered 30 min before the test. (j) Sample path

recordings during the first 5 min (top) and entire 30-min period (bottom) in the open field test. (k) The open-field activities of the control (mCherry) and DREADD-expressing mice with 5-min intervals measured 30 min after CNO injection. (l, m) Quantification of the total distance moved (l) and thigmotaxis (m) in the open field box.

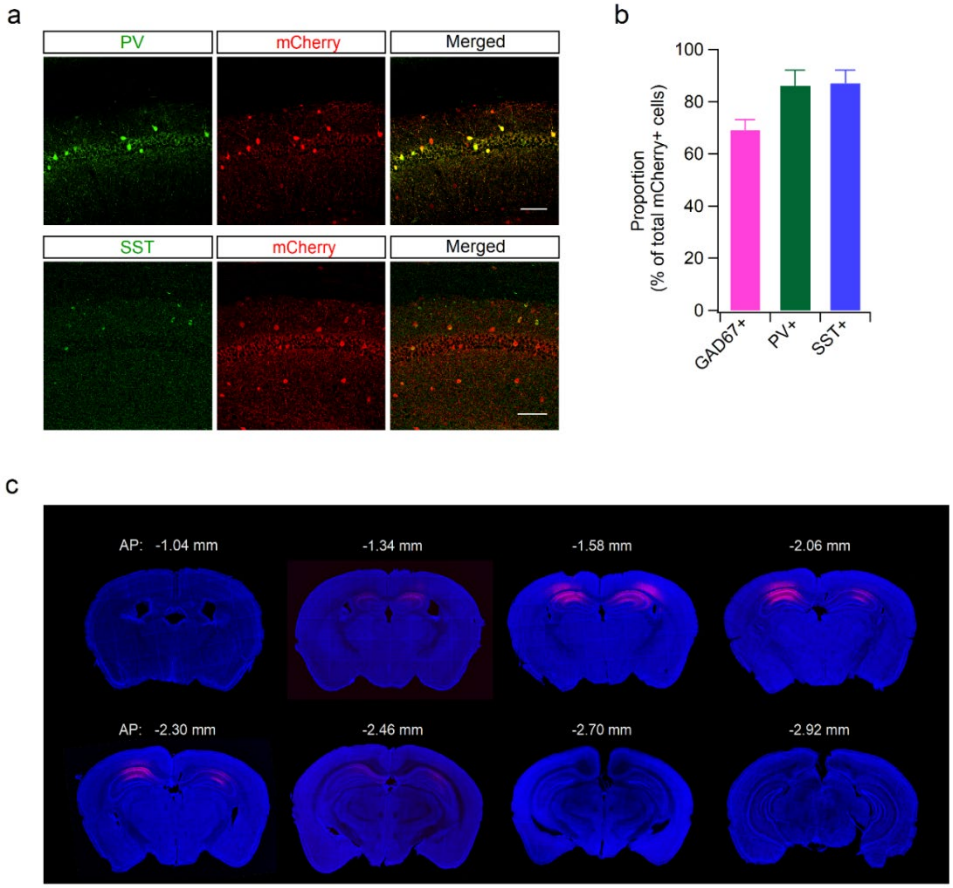
a
PV
mCherry
Merged
SST
mCherry
Merged
b
Proportion
(% of total mCherry+ cells)
100
80
60
40
20
0
GAD67+
PV+
SST+
c
AP: -1.04 mm
-1.34 mm
-1.58 mm
-2.06 mm
AP: -2.30 mm
-2.46 mm
-2.70 mm
-2.92 mm

Figure 12. Expression of mCherry in the PV- and SST-expressing neurons in the hippocampal CA1 area.

(a) Hippocampal section from Vgat-Cre mice infected with DiO-DREADDs-mCherry was double immunostained with PV/mCherry (top) or SST/mCherry (bottom) antibodies. Scale bars, 100 μm. (b) Quantification of mCherry expressing cells in the hippocampal CA1 regions. mCherry signals were detected in 69%, 86%, and 87% of GAD67-, PV-, and SST-positive cells, respectively. N = GAD67, 16 slices from 5 mice; PV, 7 slices from 3 mice; SST, 6 slices from 3 mice. (c) Series of mCherry immunofluorescent images of coronal brain sections show the distribution of cells expressing mCherry (red) in the vGat-Cre mouse. mCherry signals are mainly located in the CA1 subfields of the dorsal hippocampus. DAPI (blue) was used for the identification of brain regions. Numbers indicate anterior/posterior (AP) coordinates to Bregma.

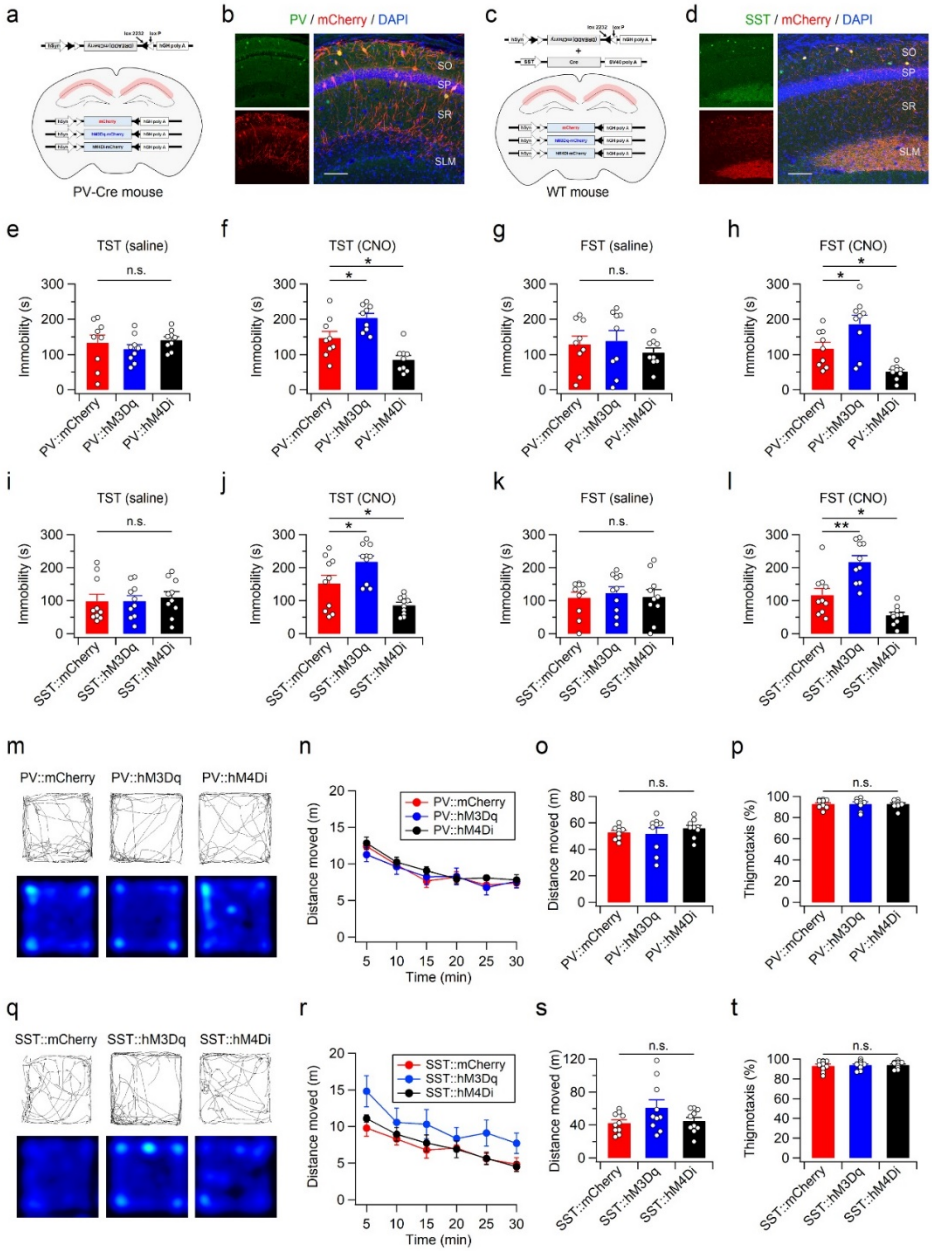
a
PV-Cre mouse
b
PV / mCherry / DAPI
SO
SP
SR
SLM
c
WT mouse
d
SST / mCherry / DAPI
SO
SP
SR
SLM
e
TST (saline)
n.s.
Immobility (s)
PV::mCherry
PV::hM3Dq
PV::hM4Di
f
TST (CNO)
g
FST (saline)
h
FST (CNO)
i
TST (saline)
SST::mCherry
SST::hM3Dq
SST::hM4Di
j
TST (CNO)
k
FST (saline)
l
FST (CNO)
m
PV::mCherry
PV::hM3Dq
PV::hM4Di
n
Distance moved (m)
Time (min)
o
Distance moved (m)
p
Thigmotaxis (%)
q
SST::mCherry
SST::hM3Dq
SST::hM4Di
r
Distance moved (m)
Time (min)
s
Distance moved (m)
t
Thigmotaxis (%)

Figure 13. Pharmacogenetic manipulation of PV or SST interneurons in the hippocampal CA1 area is sufficient to modify behavioral despair.

(a) Design of Cre-dependent expression of mCherry, hM3Dq-mCherry or hM4Di-mCherry in the PV-positive interneurons. (b) Immunohistochemical staining of hippocampal sections from PV-cre mice showing expression of mCherry in the PV-expressing cells. (c) Schematic depiction of Cre-dependent expression of mCherry, hM3Dq-mCherry or hM4Di-mCherry in the SST interneurons. (d) Expression pattern of mCherry in the hippocampal CA1 area of WT mice co-infected with AAV-DiO-mCherry and AAV-SST-Cre. Scale bars, 100 μm. (b, d). (e-l) Manipulation of PV or SST interneuron activity modifies immobility behaviors in the TST and FST. TST immobility time of PV-Cre mice infected with DiO-mCherry, DiO-hM3Dq-mCherry or DiO-hM4Di-mCherry was measured 30 min after saline (e) or CNO (f) injection. (g, h) FST immobility time of PV-Cre mice measured 30 min after saline (g) or CNO (h) injection. TST immobility time of mice expressiong mCherry, hM3Dq-mCherry or hM4Di-mCherry in the CA1 SST interneurons in the absence (i) or presence (j) of CNO. FST immobility time measured 30 min after saline (k) or CNO (l) injection in mice expressing mCherry or DREADD-

mCherry in SST neurons. Inter-test intervals were 7-8 days (e-l). (m-p) Open-field activity of mice is not significantly affected by pharmacogenetic manipulation of PV interneurons in the CA1 area. Example path recordings of PV-Cre mice during the first 5 min (m, top) and entire 30-min period (m, bottom) in the open field test. CNO was administered 30 min before the test. Quantification of the distance moved across 5-min time bins (n), entire 30-min period (o), and thigmotaxis (p) in the open field box. (q-t) same as (m-p) but for mice expressing mCherry or DREADD-mCherry in SST neurons.

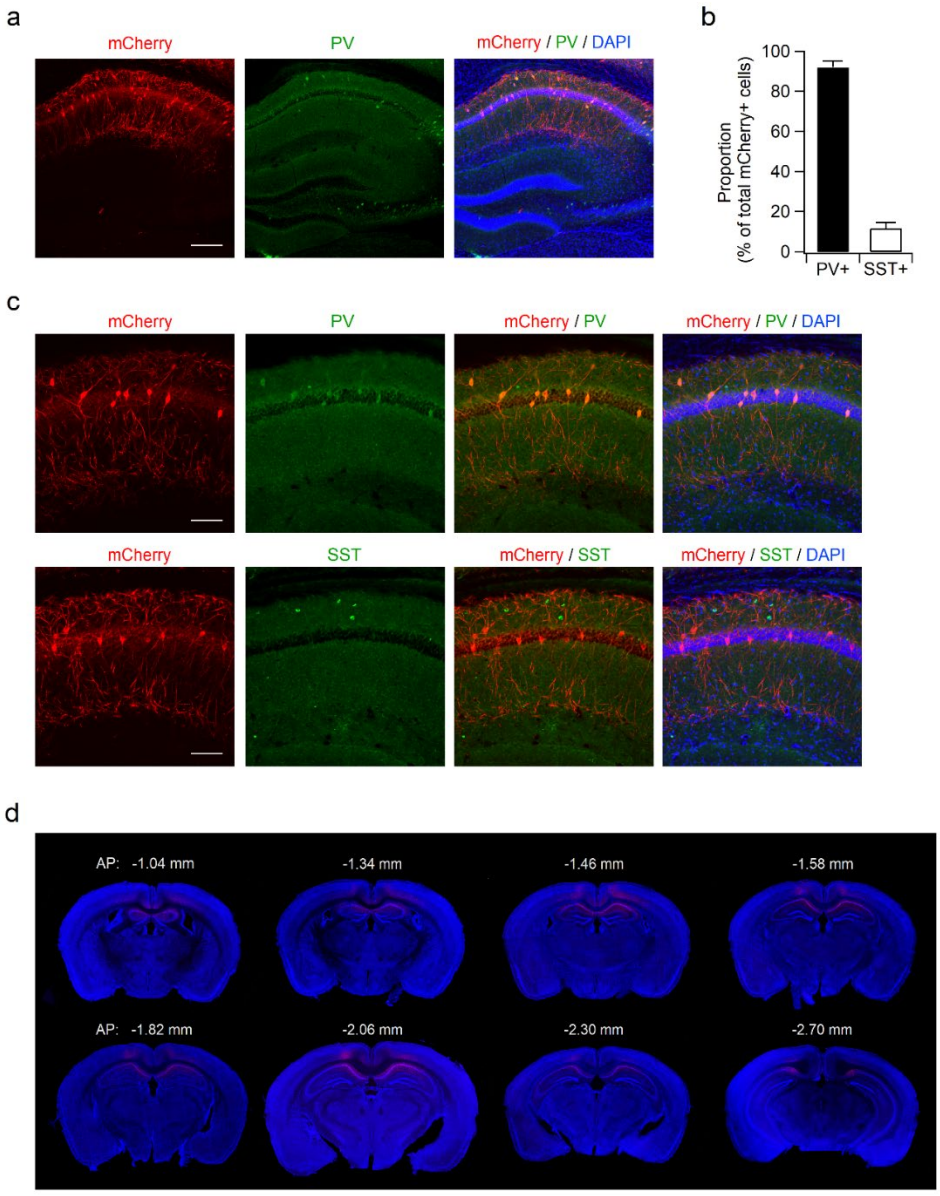
a
mCherry
PV
mCherry / PV / DAPI
b
Proportion
(% of total mCherry+ cells)
100
80
60
40
20
0
PV+
SST+
c
mCherry
PV
mCherry / PV
mCherry / PV / DAPI
mCherry
SST
mCherry / SST
mCherry / SST / DAPI
d
AP: -1.04 mm
-1.34 mm
-1.46 mm
-1.58 mm
AP: -1.82 mm
-2.06 mm
-2.30 mm
-2.70 mm

Figure 14. mCherry was mainly localized in the PV-positive cells in the hippocampus of PV-Cre mice.

(a) Sample images showing the distribution of mCherry (red) and PV (green) in the dorsal hippocampus of PV-Cre mice infected with DiO-DREADDs-mCherry. Scale bar, 200 μm. (b) mCherry signals in the CA1 area were detected in 92% and 12% of PV- and SST-positive cells, respectively. N = 8 slices from 4 mice. Scale bars, 100 μm. (c) Co-immunostainings of hippocampal sections with PV/mCherry (top) and SST/mCherry (bottom) show preferential expression of mCherry in the PV-expressing cells. (d) The series of mCherry immunofluorescent images of coronal brain sections showing the distribution of mCherry (red) in the PV-Cre mouse. Numbers indicate anterior/posterior (AP) coordinates to Bregma. DAPI (blue) was used for identification of brain regions and structures (a,c,d).

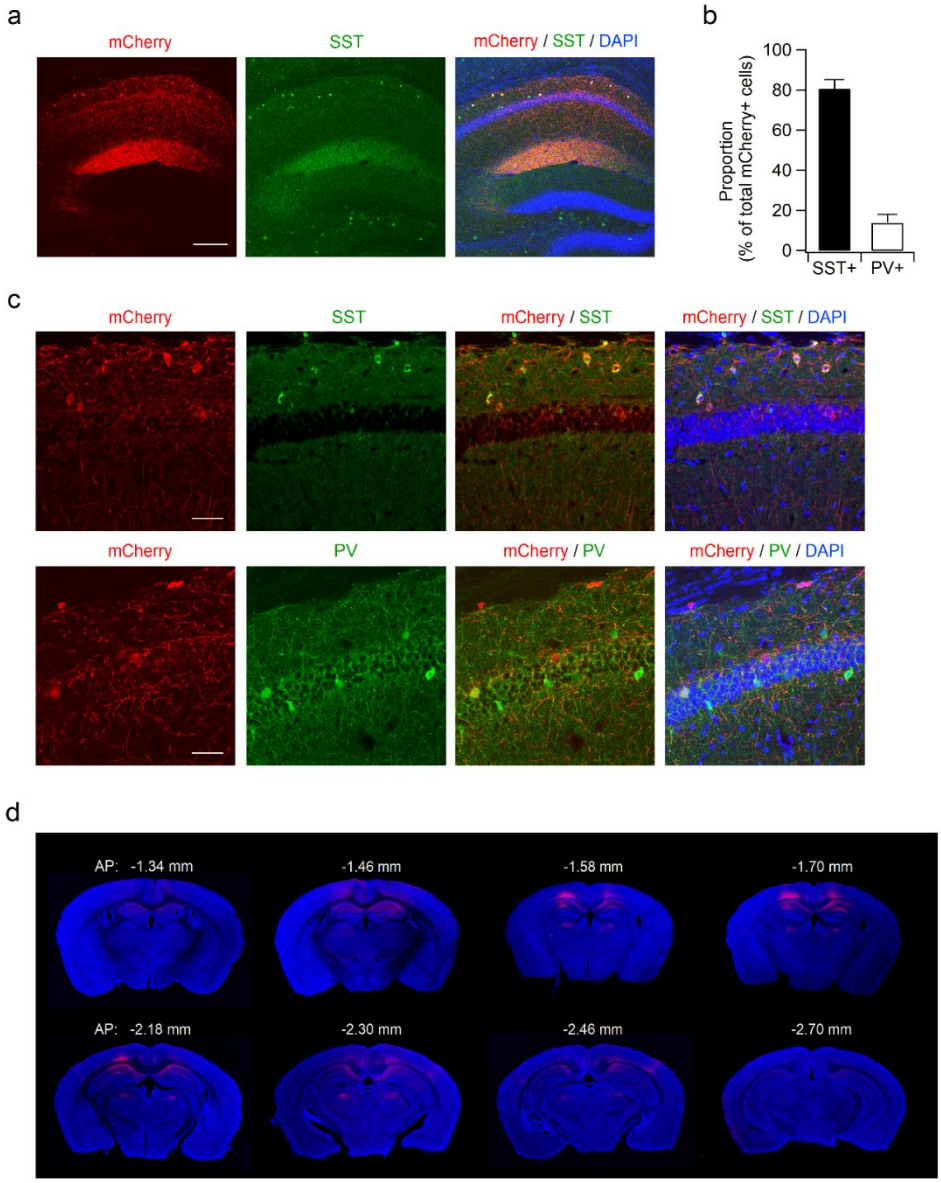
a
mCherry
SST
mCherry / SST / DAPI
b
Proportion
(% of total mCherry+ cells)
100
80
60
40
20
0
SST+
PV+
c
mCherry
SST
mCherry / SST
mCherry / SST / DAPI
mCherry
PV
mCherry / PV
mCherry / PV / DAPI
d
AP: -1.34 mm
-1.46 mm
-1.58 mm
-1.70 mm
AP: -2.18 mm
-2.30 mm
-2.46 mm
-2.70 mm

Figure 15. mCherry signals are mainly detected in the SST-immunoreactive cells by stereotaxic injection of AAV-DiO-DREADDs-mCherry/AAV-SST-Cre mixture.

(a) Sample images showing the distribution of mCherry (red) and SST (green) in the dorsal hippocampus of WT mice infected with a mix of AAV-DiO-DREADDS-mCherry and AAV-SST-Cre. Scale bar, 200 μm (b) Quantification of mCherry-expressing cells shows the predominant expression of mCherry expression in SST-positive cells (81%) than PV-positive cells (13%) in the hippocampal CA1 area. N = 6 slices from 3 mice. (c) Co-immunostainings of hippocampal sections with SST/mCherry (top) and PV/mCherry (bottom) reveal predominant expression of mCherry in SST-expressing cells. Scale bars, 50 μm. (d) The distribution of mCherry-expressing cells in the mouse brain infected with a mix of AAV-DiO-DREADDs-mCherry and AAV-SST-Cre was determined by immunohistochemical staining with mCherry antibodies. DAPI (blue) was used to identify brain regions and structures (a, c, d).

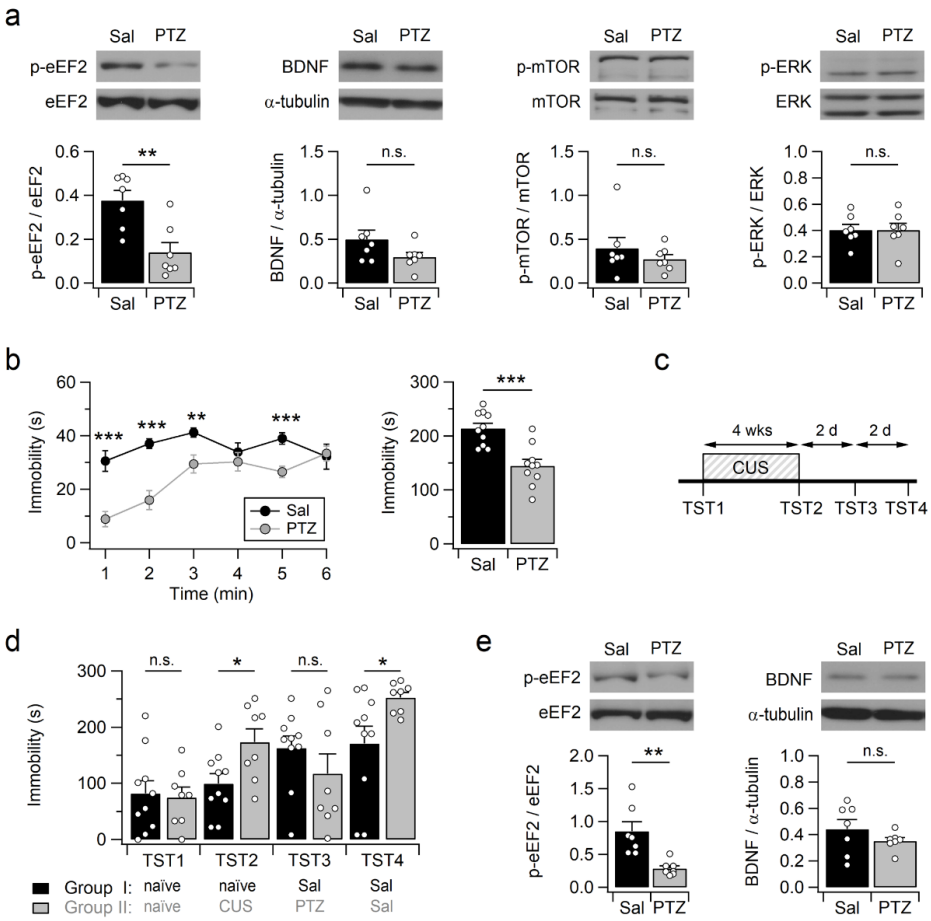
a
Sal PTZ
p-eEF2
eEF2
BDNF
α-tubulin
p-mTOR
mTOR
p-ERK
ERK
p-eEF2 / eEF2
BDNF / α-tubulin
p-mTOR / mTOR
p-ERK / ERK
n.s.
b
Immobility (s)
Time (min)
Sal
PTZ
c
4 wks
2 d
2 d
CUS
TST1
TST2
TST3
TST4
d
Group I: naïve naïve Sal Sal
Group II: naïve CUS PTZ Sal
e

Figure 16. PTZ induces rapid and sustained eEF2 dephosphorylation in the hippocampus but transient antidepressant effects.

(a) Representative western blots for total and phosphorylated forms of eEF2, mTOR and ERK, and BDNF in hippocampal samples obtained 30 min after treatment (top). Densitometric analysis shows the selective effect of PTZ on eEF2 but not BDNF, mTOR and ERK signaling in the hippocampus (bottom). (b) TST immobility is reduced in mice received PTZ. Bar graph represents total immobility time over 6 min (right). TST was performed 30 min after PTZ injection. (c) Experimental scheme. After scoring the immobility time of naïve WT mice in the TST (TST1), one group of mice were exposed to CUS for 4 weeks. CUS-induced despair-like behaviors were analyzed by the TST (TST2) on the next day after the end of CUS. Thirty minutes before the third TST (TST3), control and stressed mice received saline and PTZ, respectively. Both groups of mice were injected with saline 30 min before the fourth TST (TST4). (d) PTZ administration transiently reduces despair-like behaviors induced by CUS. (e) Single PTZ administration induces sustained activation of eEF2 signaling in the hippocampus. Representative western blots for eEF2 and BDNF in hippocampal lysates prepared 48 h after PTZ injection (top).

Quantification of p-eEF2/eEF2 ratio and BDNF levels in the hippocampus (bottom).

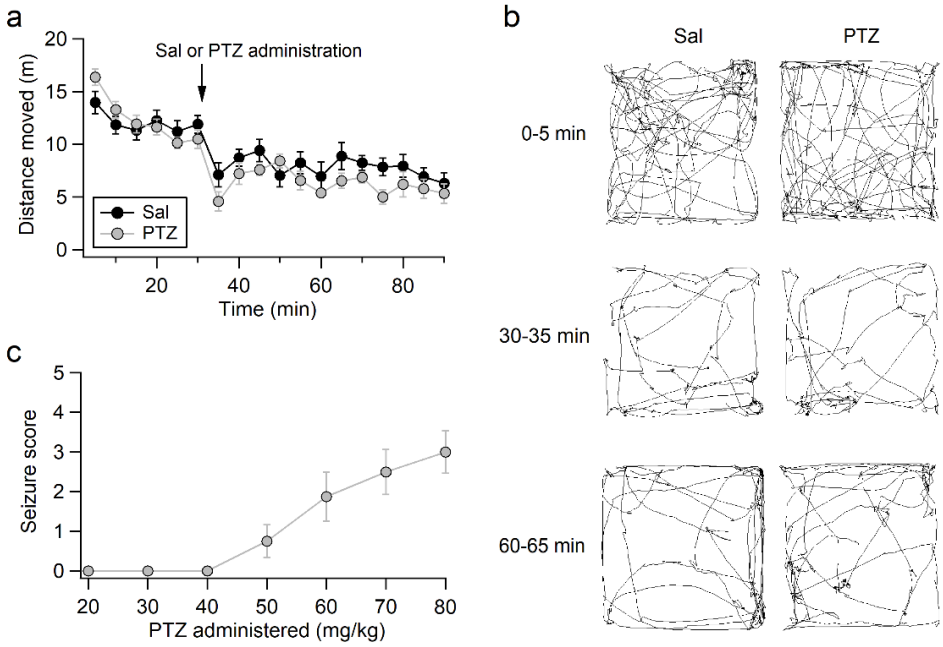
a
Sal or PTZ administration
Distance moved (m)
Time (min)
Sal
PTZ
b
Sal
PTZ
0-5 min
30-35 min
60-65 min
c
Seizure score
PTZ administered (mg/kg)

Figure 17. Low-dose administration of PTZ does not induce seizure activity or hyperlocomotion.

(a) Mice received PTZ (20 mg/kg) or saline (Sal) 30 min after baseline activity recording during the 90-min open-field test. (b) Sample path recordings during the first 5 min of the open field test, and immediately after (30-35 min) and 30 min after (60-65 min) drug administration. (c) Dose-response curves of the effect of different PTZ doses on behavioral seizures in male mice. Animals were monitored for 1 h after the intraperitoneal injection of PTZ. The severity of the behavioral seizures was scored as follows: score 0, no seizure; score 1, head nodding; score 2, clonic jerks, sporadic shaking; score 3, full-body spasms, Straub tail, rearing; score 4, shrieking, jumping, falling; score 5, violent convulsions, death. N = 8-10 mice for each dose.

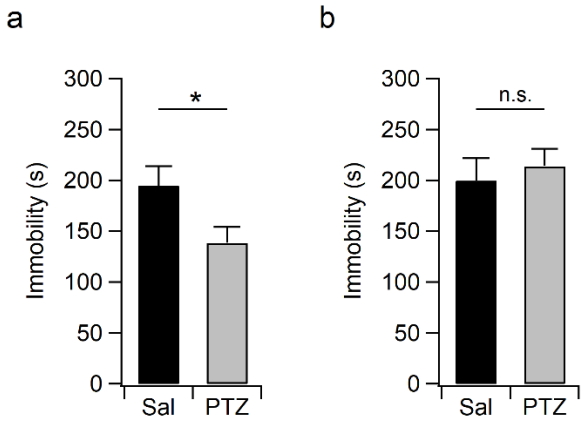

Figure 18. Single PTZ administration induces rapid but not long-lasting antidepressant behaviors.

(a, b) Bar graphs show total immobility time during the 6-min-TST measured 30 min (a) and 48 h (b) after PTZ injection (20 mg/kg, i.p.).

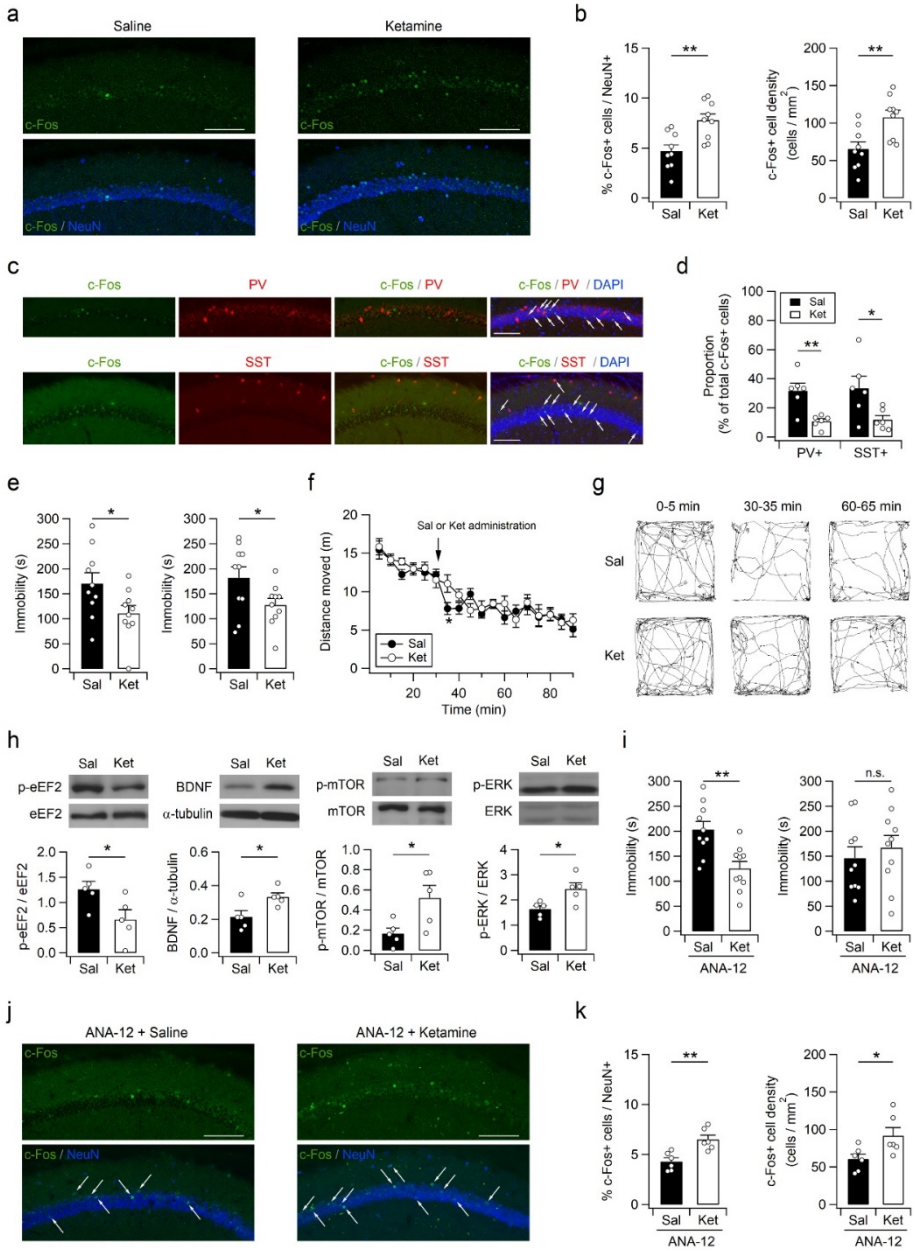
a
Saline
Ketamine
c-Fos
c-Fos / NeuN
b
% c-Fos+ cells / NeuN+
c-Fos+ cell density (cells / mm2)
Sal
Ket
c
c-Fos
PV
c-Fos / PV
c-Fos / PV / DAPI
SST
c-Fos / SST
c-Fos / SST / DAPI
d
Proportion (% of total c-Fos+ cells)
PV+
SST+
e
Immobility (s)
f
Sal or Ket administration
Distance moved (m)
Time (min)
g
0-5 min
30-35 min
60-65 min
h
p-eEF2
eEF2
BDNF
α-tubulin
p-mTOR
mTOR
p-ERK
ERK
p-eEF2 / eEF2
BDNF / α-tubulin
p-mTOR / mTOR
p-ERK / ERK
i
n.s.
ANA-12
j
ANA-12 + Saline
ANA-12 + Ketamine
k

Figure 19. Ketamine induces rapid c-Fos expression in the hippocampus and anti-despair-like behaviors.

(a) Immunohistochemical staining of hippocampal sections with the c-Fos antibody shows rapid activation of neurons by ketamine. To avoid possible effects of novel context on hippocampal neurons, mice received saline (Sal) or ketamine (Ket) and anesthetics (1 h after Sal or Ket injection) in their homecages in the vivarium. (b) Quantification of cells expressing c-Fos in the hippocampal CA1 area. (c) Hippocampal sections from ketamine-treated mice were co-stained with antibodies to c-Fos/PV (top) or c-Fos/SST (bottom). (d) Cells expressing c-Fos/PV or c-Fos/SST were measured as a percentage of total c-Fos positive cells in the hippocampal CA1 area from saline- or ketamine-treated mice. (e) Single ketamine injection induces rapid and long-lasting antidepressant effects. Reduction in TST immobility can be observed at both 30 min (left) and 48 h (right) after ketamine injection. (f) Open-field activities of mice in 5-min time bins across a 90-min session. Mice received ketamine (5 mg/kg) or saline 30 min after baseline activity recording. (g) Sample path recordings during the first 5 min, and immediately after (30-35 min) and 30 min after (60-65 min) drug administration. (h) Ketamine rapidly activates eEF2,

BDNF, mTOR and ERK signaling pathways in the hippocampus. Representative western blots (top) and quantification (bottom) of proteins in hippocampal lysates obtained 30 min after ketamine injection. (i) Pretreatment (30 min before ketamine injection) with ANA-12 blocks sustained but not acute antidepressant effects of ketamine. Bar graphs represent time spent immobile during the 6 min-TST performed 30 min (left) and 48 h (right) after ketamine injection. (j) Ketamine increases the expression of c-Fos in the hippocampus in mice intraperitoneally administered ANA-12 (30 min before Sal or Ket injection). (k) Quantification of c-Fos+ cells in the hippocampal CA1 area from ANA-12-pretreated mice received saline or ketamine. Scale bars, 100 μm (a,c, and j).

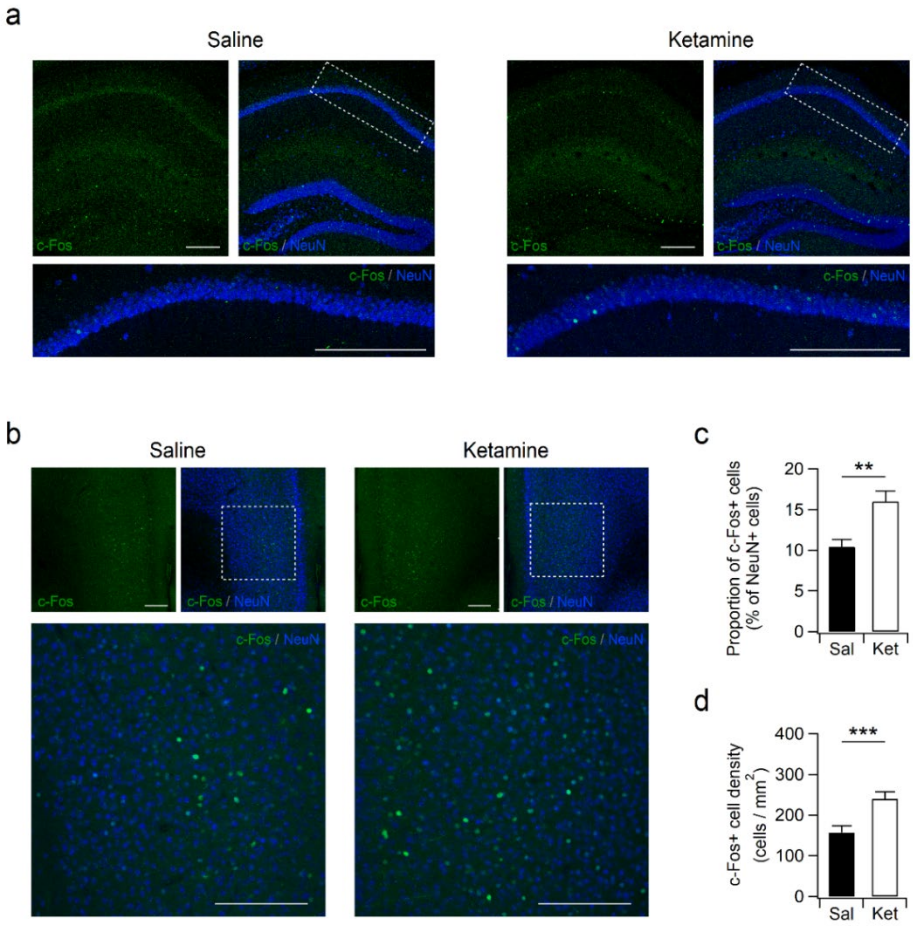
a
Saline
Ketamine
c-Fos
c-Fos / NeuN
b
Saline
Ketamine
c-Fos
c-Fos / NeuN
c
Proportion of c-Fos+ cells (% of NeuN+ cells)
20
15
10
5
0
**
Sal
Ket
d
c-Fos+ cell density (cells / mm2)
400
300
200
100
0
***
Sal
Ket

Figure 20. Enhanced c-Fos expression in the hippocampus and mPFC of ketamine-treated mice.

(a) Coronal hippocampal sections from saline- or ketamine-treated mice were co-immunostained with c-Fos (green) and NeuN (blue) antibodies. Bottom images show the white dotted box regions magnified from top images. Sections were prepared 1 h after saline or ketamine injection. (b) Ketamine induced rapid enhancement in c-Fos (green) expression in the mPFC. NeuN (blue) was used to identify neurons in the mPFC. Bottom shows magnified images indicated by the dotted white boxes in the upper panels. Scale bars, 200 μm (a,b). (c) The number of cells expressing c-Fos were normalized to the total number of NeuN+ cells in the mPFC. N = 6 slices from 3 mice. (d) Bar graphs represent the density of cells expressing c-Fos in the mPFC of mice receiving saline or ketamine. N = 6 slices from 3 mice.

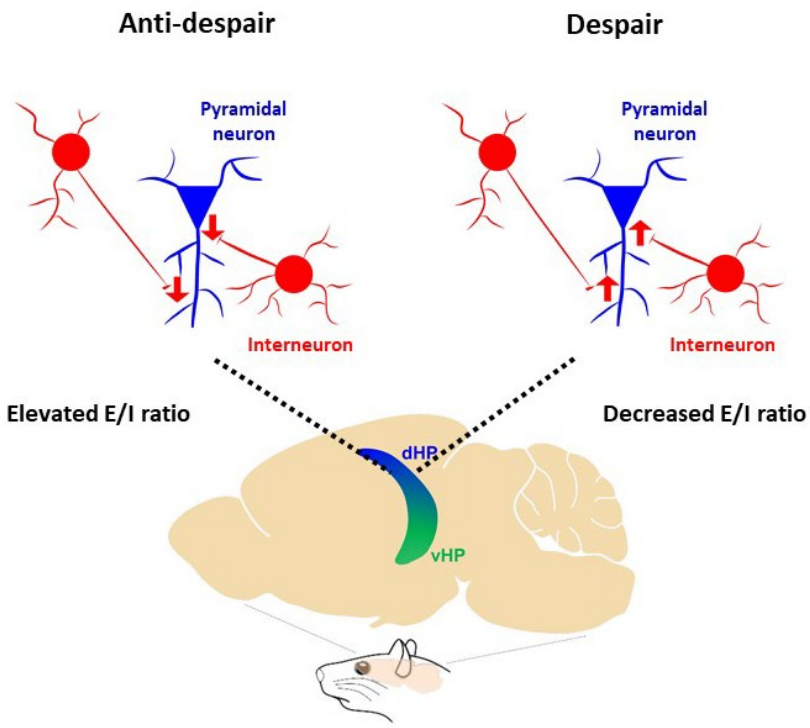

Figure 21. Dorsal hippocampus regulates behavioral despair in mice.

Table 1. Statistical analysis of multiple TST and FST

Figure number	Experiment	Statistics_ANOVA with Tukey's HSD		
Figure.7c	+/+ TST1−3	F(2,18)=1.98 p=0.168	TST1 vs. TST2	p=0.944
			TST1 vs. TST3	p=0.298
			TST2 vs. TST3	p=0.179
Figure.7c	−/− TST1−3	F(2,18)=3.21 p=0.064	TST1 vs. TST2	p=0.0521
			TST1 vs. TST3	p=0.460
			TST2 vs. TST3	p=0.404
Figure.15d	Group I (naïve, Sal) TST1−4	F(3,36)=3.52 p=0.025	TST1 vs. TST2	p=0.955
			TST1 vs. TST3	p=0.095
			TST1 vs. TST4	p=0.057
			TST2 vs. TST3	p=0.251

			TST2 vs. TST4	p=0.166
			TST3 vs. TST4	p=0.995
Figure.15d	Group II (CUS, PTZ) TST1−4	F(3,28)=10.683 p<0.001	TST1 vs. TST2	p=0.030
			TST1 vs. TST3	p=0.585
			TST1 vs. TST4	p<0.001
			TST2 vs. TST3	p=0.350
			TST2 vs. TST4	p=0.103
			TST3 vs. TST4	p=0.002

Figure number	Experiment	Statistics, Paired t-test	
Figure.7c	TST1 vs. TST2	T(6)=0.320	p=0.760
Figure.10f,g	TST1 vs. TST2	T(9)=-0.726	p=0.487
Figure.10h,i	FST1 vs. FST2	T(6)=-2.418	p=0.052
Figure.12e,f	TST1 vs. TST2	T(8)=-0.687	p=0.512
Figure.12g,h	FST1 vs. FST2	T(8)=0.640	p=0.540
Figure.12i,j	TST1 vs. TST2	T(9)=-2.259	p=0.0502
Figure.12k,l	FST1 vs. FST2	T(9)=-0.403	p=0.697
Figure.15d	TST1 vs. TST2	T(9)=-0.809	p=0.439
Figure.17a,b	TST1 vs. TST2	T(9)=-0.205	p=0.842
Figure.18e	TST1 vs. TST2	T(9)=-0.489	p=0.637
Figure.18i	TST1 vs. TST2	T(9)=2.212	p=0.054

Chapter 2. Deficiency of aminopeptidase P1 alters gene expression and glial population in the hippocampus.

Introduction

One of the hallmarks of living systems is metabolism, the sum of biochemical processes that occur within each cell of a living organism, and many human diseases are associated with abnormal metabolic states(DeBerardinis and Thompson 2012). Metabolic disturbance or perturbation in brain cells often causes neuropsychiatric disorders and severe brain injury. One example is inborn errors of metabolism (IEMs), also known as inherited metabolic disorders (IMDs), which frequently accompany abnormal neurodevelopment and behaviors, intellectual disability, epilepsy, and neurodegeneration(Pan and Vockley 2013; van Karnebeek and Stockler 2012). IEMs are a large class of genetic disorders resulting from a deficiency or defective activity of a single enzyme in the metabolic pathway. Despite the substantial prevalence of IEMs ranging from 1/784 to 1/2555 births collectively(Campeau, Scriver, and Mitchell 2008), each disorder is

individually rare. This rarity hinders understanding of each disease and development of effective medications to relieve the symptoms of the disease, especially the neurological symptoms. Animal models for rare inheritable diseases provide opportunities to understand pathological mechanisms, including molecular and cellular changes associated with the disease.

Aminopeptidase P1, encoded by the Xpnpep1 gene, is a proline-specific endopeptidase that cleaves the N-terminal amino acid residue of peptides with a penultimate proline residue(Cottrell, Hooper, and Turner 2000). Aminopeptidase P1 deficiency is a rare inherited metabolic disease that causes massive urinary excretion of undigested peptides containing a penultimate proline(Blau, Niederwieser, and Shmerling 1988; Yoon et al. 2012). In addition to peptiduria, Xpnpep1-mutant mice and a human patient with aminopeptidase P1 deficiency exhibit neurological complications such as microcephaly and epilepsy(Blau, Niederwieser, and Shmerling 1988; Bae et al. 2018; Yoon et al. 2012). Aminopeptidase P1 is abundant in the brain and the expression of Xpnpep1 mRNA in the human brain tissue is as stable as housekeeping genes(Durrenberger et al. 2012), indicating that

aminopeptidase P1 is critical for normal brain function. Consistent with this idea, deficiency of aminopeptidase P1 in mice results in reduced body and brain size, hyperactivity, impaired hippocampus-dependent learning, neurodegeneration in the hippocampal CA3 area(Bae et al. 2018; Yoon et al. 2012). Deducing from the enzymatic activity of aminopeptidase P1, bioactive peptides with a penultimate proline such as bradykinin, substance P, neuropeptide Y, peptide YY, and interleukins, are thought to be the substrates of aminopeptidase P1(Vanhoof et al. 1995). Accumulation or delayed removal of peptides containing a penultimate proline may modify molecular signaling in the brain cells, resulting in brain dysfunction in aminopeptidase P1 deficiency. However, how deficiency of aminopeptidase P1 causes neurodegeneration and hippocampal dysfunction is unclear.

The present study focused on molecular and cellular alterations in the hippocampus with aminopeptidase P1 deficiency because proper metabolism of brain cells, including neurons, astrocytes, and microglia, is critical for normal brain function and because glial alteration may contribute to complex neurological and psychiatric complications in IEMs. I found that aminopeptidase P1 is predominantly expressed in

neurons, and genetic ablation of Xpnpep1 modified the population of glial cells in the hippocampus. I also show that glial changes in aminopeptidase P1 deficiency are distinct from changes seen in common late-onset neurodegenerative diseases and other IEMs.

Result

Gene expression profile of the hippocampus in mice with aminopeptidase P1 deficiency

Xpnpep1$^{-/-}$ mice exhibit hippocampal pathology and impaired hippocampus-dependent learning and memory(Bae et al. 2018). To identify differentially expressed genes in the Xpnpep1$^{-/-}$ hippocampus, I performed microarray analysis of gene expression profiles in the hippocampal samples from 5-week-old wild-type (WT; Xpnpep1$^{+/+}$) and Xpnpep1$^{-/-}$ mice. To avoid possible false-positive interpretations caused by a variation in the individual sample contribution to the pooled sample, each sample was independently hybridized to a single microarray chip and the expression levels of each gene were compared among animals by statistical analyses(Jolly et al. 2005).

Of the total 28,853 gene-level probe sets, the number of probe sets considered to be valid for individual samples did not differ between genotypes (+/+, 27,856 ± 84; −/−, 28,093 ± 90; $t_{(6)} = -1.926$, $p = 0.102$). However, when I compared the expression levels of each gene with a threshold fold change greater than 1.5, or less than 0.667 (1.5-fold down-regulation), I identified 32 genes as differentially

expressed genes (DEGs) with statistical significance ($p < 0.05$, Figure 22a). Among the 32 DEGs, 26 genes (Omd, Bmp5, Serping1, Colec12, Aebp1, Spp1, Aldh1a2, Slc22a2, Fmod, Slc6a20a, Aox3, Ccnd1, D7Ertd443e, Xpnpep1, Dsp, Pdlim1, Gstm6, Scn7a, Casp1, Prickle3, Plp2, Aspa, Opalin, Serpinb1a, Myoc, and Tnfaip6) were down-regulated (Figure 22b and c), while 6 genes (Vmn2r50, Zfp772, 2810047C21Rik1, Vmn1r90, Pcdhb2, and Pcdhb3) were up-regulated in the Xpnpep1$^{-/-}$ hippocampus (Figure 22d and e). As shown in Table 3, DEGs in Xpnpep1$^{-/-}$ hippocampus were significantly enriched with GO categories linking to metabolic process (GO:0008152) and cellular response to organic substance (GO:0071310) in biological process, cytoplasm (GO:0005737), extracellular exosome (GO:0070062), extracellular matrix (GO:0031012), extracellular space (GO:0005615) and extracellular region (GO:0005576) in cellular component. More information about the involved genes of GO enrichment is shown in Table 3. Notably, Xpnpep1 exhibited the largest fold changes (less than 0.21, $p = 0.0000133$) in gene expression by microarray. Since the Xpnpep1 gene in the mutant mice was disrupted by gene trap mutagenesis to produce Xpnpep1-β-geo (β-galactosidase +

neomycin phosphotransferase) fusion transcripts(Yoon et al. 2012) which lack the coding region of the peptidase domain, weak Xpnpep1-positive signals in the Xpnpep1$^{-/-}$ samples might stem from probes in the Xpnpep1 probe set that detect upstream endogenous Xpnpep1 regions of the Xpnpep1-β-geo fusion transcript. Interestingly, the expression levels of Slc6A20a (solute carrier family 6, member 20; sodium/imino-acid transporter, SIT1) were significantly lower in Xpnpep1$^{-/-}$ than in the WT samples (Figure 22c). Considering that Slc6A20a transports imino acids, such as proline and hydroxyproline, across the plasma membrane through the Na^{+}-dependent mechanism(Takanaga et al. 2005; Kowalczuk et al. 2005), downregulation of Slc6A20a may reflect homeostatic responses of hippocampal cells to altered imino acid metabolism in Xpnpep1$^{-/-}$ mice. In addition, reduced expression of Dsp indicates that postnatal development of the dentate gyrus is delayed in Xpnpep1$^{-/-}$ mice(Kobayashi et al. 2010). Importantly, these DEGs comprise genes that are abundant in astrocytes (Myoc, Aldh1a2, Gstm6, Ccnd1, Tnfaip6)(Mizee et al. 2014; Cammer and Zhang 1993; Ciapa and Granon 2018; Zhang et al. 2014; Kwon et al. 2014), oligodendrocytes

(Serpinb1a, Aspa, Opalin)(Zhang et al. 2014), microglia (Slc6a20a, Spp1)(Takanaga et al. 2005; Li et al. 2017; Yamamiya, Tanabe, and Muramatsu 2019) or neurons (Dsp, Slc22a2)(Lein, Zhao, and Gage 2004; Simon et al. 2012; Matsui, Nakata, and Kobayashi 2016), indicating that a deficiency of aminopeptidase P1 affects both glia and neurons in the hippocampus.

Expression patterns of aminopeptidase P1 in the hippocampus.

To investigate how deficiency of aminopeptidase P1 causes neurodegeneration and hippocampal dysfunction, I first examined the developmental expression pattern of aminopeptidase P1 in the forebrain and hippocampus. In the western blot analysis, the expression levels of aminopeptidase P1 in the forebrain and hippocampus were consistently maintained throughout postnatal development (Figure 23). Aminopeptidase P1 is widely expressed in brain neurons, including hippocampal principal neurons(Yoon et al. 2012). Loss of aminopeptidase P1 causes neuronal loss and vacuolation in the hippocampal CA3 region and activation of multiple cell death pathway,

including necrosis, apoptosis, and autophagy in the hippocampus(Bae et al. 2018). However, the cellular mechanisms underlying neurodegeneration in the hippocampus of Xpnpep1$^{-/-}$ mice are unclear. Because anti-aminopeptidase P1 antibody was not suitable for immunohistochemical staining and Xpnpep1 mutant mice express a β-galactosidase (lacZ) reporter under the control of the Xpnpep1 promoter, I labeled aminopeptidase P1-expressing cells in the hippocampal sections from 4 - to 5-week-old Xpnpep1$^{+/-}$ and Xpnpep1$^{-/-}$ mice by X-gal staining. The sections were then immunostained with the neuronal marker NeuN, the astrocyte markers GFAP (glial fibrillary acidic protein) and S100β (S100 calcium-binding protein beta chain), the microglial marker Iba1 (ionized calcium binding adapter molecule 1), or the oligodendrocyte marker O4. In confocal fluorescence microscopy, I observed that each marker labeled distinct cell populations (Figure 24).

Consistent with previous results(Yoon et al. 2012), the hippocampal principal cell layers, which contain mainly excitatory neurons, exhibited intense X-gal staining signals by light transmission microscopy (Figure 25a-d). Strong punctate signals were mostly detected within

the cell body of principal neurons in both Xpnpep1$^{+/-}$ and Xpnpep1$^{-/-}$ mice. In addition, I detected disperse X-gal-positive signals in the dentate gyrus (DG) hilus and outer molecular layer, CA3 *stratum lucidum,* and CA1 *stratum radiatum*. (Figure 25b-d). When I immunostained the X-gal stained section with NeuN antibodies, I observed X-gal precipitates within the NeuN-positive neuronal somata (Figure 25g-i and Figure 26a-d). The merged transmittance and fluorescence images further revealed that X-gal signals were present in MAP2-positive dendrites of neurons in the hippocampus (Figure 26a-d). However, X-gal signals scarcely overlapped with the astrocyte markers GFAP and S100β (Figure 26e-h). In addition, X-gal signals were rarely detected in the CA3 *stratum radiatum*, CA1 *stratum lacunosum-moleculare*, and *stratum oriens* of CA1 and CA3, whereas astrocytes were abundant in these areas (Figure 27). Similar to astrocytes, X-gal signals did not overlap with microglia (Figure 26i and j) and oligodendrocytes (Figure 26k and l) markers.

Previous RNA sequencing studies reported that Xpnpep1 transcripts were present in astrocytes, microglia, and neurons(Zhang et al. 2014; Zhang et al. 2016). However, when I examined the protein expression

levels of aminopeptidase P1 in hippocampal neuron cultures and glial cultures prepared from Xpnpep1$^{+/+}$ embryonic mice, the amount of aminopeptidase P1 was significantly higher (> 7 times) in the βIII-tubulin enriched neuronal lysates than in the GFAP-enriched glial lysates (Figure 28). Collectively, these results suggest that aminopeptidase P1 is predominantly expressed in neurons in the hippocampus.

Reduction of astrocytes in the Xpnpep1$^{-/-}$ hippocampus

Despite exhibiting predominant expression of aminopeptidase P1 in neurons, DEGs identified by microarray and qRT-PCR indicate that aminopeptidase P1 deficiency affects glial cells in the hippocampus. Since astrocyte alterations are frequently associated with brain disorders(Dossi, Vasile, and Rouach 2018), I first determined the density of astrocytes in the hippocampus of 5-week-old mice using the astrocyte markers GFAP and S100β. GFAP expression in astrocytes is known not to be uniform. It is strong in astrocytes compartmentalized to the hippocampus or reactive astrocytes, while

astrocytes in other brain areas exhibit mild to weak GFAP expression in the normal state(Alibhai, Diack, and Manson 2018; Chai et al. 2017). S100β is less specific than GFAP, but it is broadly expressed in astrocytes(Matias, Morgado, and Gomes 2019). Despite that both genotypes showed similar cross-sectional areas in the hippocampus (Figure 28), Xpnpep1$^{-/-}$ mice exhibited fewer GFAP-positive cells in the hippocampus compared to WT mice (Figure 30a-f). Similarly, the number of S100β-positive cells was decreased in the Xpnpep1$^{-/-}$ hippocampus. Quantification of the numbers of GFAP- or S100β-positive cells revealed significant differences in the density of hippocampal astrocytes between the two genotypes (Figure 30d-f). Notably, a reduction in astrocyte density was detected in the whole hippocampal subregions including CA3, CA1, and DG areas (Figure 30a-f). Considering that many neurodegenerative diseases accompany reactive astrogliosis and that reduced astrocyte density was observed in major depressive disorder and starvation(Dossi, Vasile, and Rouach 2018; Frintrop et al. 2019), neurodegeneration accompanying astrocyte reduction in the hippocampus is a unique pathological change in aminopeptidase P1 deficiency. In addition, the morphology of

astrocytes in the Xpnpep1$^{-/-}$ CA3 subfields, determined by GFAP-immunoreactive signals distributed in the cellular processes, was similar to that of control astrocytes (Figure 30g), despite the presence of vacuoles of varying sizes in the Xpnpep1$^{-/-}$ CA3 subfields (Figure 30a and g). Sholl analyses of astrocytic processes showed no difference between the two genotypes (Figure 30h). This observation also eliminates the possibility of astrocytic gliosis in the Xpnpep1$^{-/-}$ hippocampus. Consistent with the reduced density of astrocytes, protein expression levels of GFAP were significantly decreased in the Xpnpep1$^{-/-}$ hippocampus (Figure 30i and j). However, there is a possibility that GFAP expression in each astrocyte, in addition to the reduced astrocyte density, was reduced by the deficiency of aminopeptidase P1.

Increased density of microglia in the Xpnpep1$^{-/-}$ CA3 area.

I next examined microglial populations in the hippocampus using Iba1 and CD68 antibodies. Because Xpnpep1$^{-/-}$ mice exhibit microcephaly(Yoon et al. 2012), I selected coronal brain sections that

displayed similar hippocampus morphology and size for both genotypes (Figure 29c and d). Iba1-positive signals were detected in the cell body and thin processes of microglia, whereas immunoreactive signals for CD68, the reactive microglia marker(Ugolini et al. 2018), were mainly detected as tiny puncta near the cell bodies but not entire cell structures in both genotypes of mice (Figure 31a and b). When I induced microglial activation in WT mice by intraperitoneal injections of lipopolysaccharide (LPS, 1 μg/kg; once daily for 4 days), intense immunoreactivity for CD68 was detected in the cell body and processes of microglia (Figure 32). Punctate CD68-positive signals in Xpnpep1$^{-/-}$ microglia suggest that deficiency of aminopeptidase P1 does not induce activation of microglia in the hippocampus (Figure 31a and b). However, the density of microglia in the CA3 subfields of Xpnpep1$^{-/-}$ mice was significantly higher than those in WT mice (Figure 31a and c). Interestingly, both genotypes showed similar numbers of Iba1-positive cells in the DG and CA1 subfields of the hippocampus (Figure 31d-g). This finding is consistent with the neuropathology of Xpnpep1$^{-/-}$ mice in that neurodegeneration was exclusively observed in the CA3 subfield(Bae et al. 2018). In addition,

some microglia were present but did not accumulate around vacuoles in the CA3 area of Xpnpep1$^{-/-}$ mice (Figure 31a and Figure 33)(Hickman et al. 2018). When I examined the expression levels of Iba1 and CD68 proteins in the whole hippocampal extracts, the expression levels of these proteins were not significantly different between the two genotypes (Figure 31h and i). Collectively, these results suggest that a deficiency of aminopeptidase P1 selectively increases the number of microglial cells in the hippocampal CA3 subfield.

Discussion

Although inborn errors of metabolism (IEMs) are common causes of brain dysfunction and intellectual disability, the cellular changes associated with brain dysfunction are unknown in most metabolic diseases. The present study demonstrates previously unknown changes in the hippocampus with inherited metabolic disease in which long-term exposure of the brain to the altered metabolic status in aminopeptidase P1 deficiency modifies glial population in the hippocampus. Specifically, the density of microglia in the hippocampal CA3 subfield was higher in Xpnpep1$^{-/-}$ mice than in WT mice, whereas the mutant mice exhibited fewer astrocytes in the hippocampus. Interestingly, astrocyte activation or reactive gliosis was not detected in the Xpnpep1$^{-/-}$ hippocampus. Thus, altered glial population and an aberrant glial environment might cause neurodegeneration and hippocampal dysfunction in aminopeptidase P1 deficiency.

As IEMs are usually caused by defects in enzymes, accumulation of substrates for the defective enzyme in the cerebrospinal fluid is considered to cause brain dysfunction and injury, but long-term changes in the brains exposed to the accumulated substrates are

unclear. In the present study, I identified down-regulated genes in the Xpnpep1$^{-/-}$ hippocampus through microarray. There is a possibility that some down-regulated genes that are abundant in astrocytes might be identified as DEGs due to the reduction of astrocyte density in the Xpnpep1$^{-/-}$ hippocampus. Intriguingly, a previous report showed that Slc6a20 mRNA was mainly detected in microglia, meninges, and choroid plexuses in the brain(Takanaga et al. 2005). Although Xpnpep1$^{-/-}$ mice exhibit an increased number of microglia in the hippocampal CA3 subfields, the expression levels of Slc6a20a transcripts in the hippocampus were decreased. Slc6a20a transports imino acids, including proline and hydroxy proline, through the Na^{+}- and Cl^{-}-dependent mechanisms(Kowalczuk et al. 2005; Takanaga et al. 2005). The reduction of Slc6a20a in the Xpnpep1$^{-/-}$ hippocampus probably indicates an altered imino acid gradient across the plasma membrane of brain cells and further suggests adaptive changes in the Xpnpep1$^{-/-}$ brain. Similarly, the reduced mRNA expression of Slc22a2 (OCT2), a transporter for norepinephrine (NE) and serotonin (5-HT), seems to be associated with adaptive changes in the Xpnpep1$^{-/-}$ brain. Slc22a2 is highly expressed in limbic neurons including CA1 and CA3

pyramidal neurons, but not in astrocytes in the brain, and contributes to the clearance of NE and 5-HT, which suppress the firing activity of CA3 pyramidal neurons(Bacq et al. 2012). Reduction of Slc22a2 may slow the clearance of NE and 5-HT, thereby intensifying the suppression of abnormally excitable CA3 neurons in Xpnpep1$^{-/-}$ mice. Another interesting finding from the gene expression profile of the Xpnpep1$^{-/-}$ hippocampus was the down-regulation of desmoplakin (Dsp). Dsp is exclusively expressed in dentate granule cells (GCs) in the hippocampus, and the expression level of Dsp increases with postnatal development(Kobayashi et al. 2010; Lein, Zhao, and Gage 2004). Considering that reduced Dsp expression is a sign of the "immature dentate gyrus (iDG)", which is frequently observed in genetically engineered mice with abnormal behaviors(Hagihara et al. 2013), these results suggest that neurodegeneration and delayed neurodevelopment coincide in aminopeptidase P1 deficiency(Saudubray and Garcia-Cazorla 2018). Intriguingly, mice with the iDG phenotype exhibit hyperexcitability of the dentate GCs. The existence of developmental retardation, hyperlocomotion, and impaired hippocampus-dependent learning in Xpnpep1$^{-/-}$ mice(Bae et

al. 2018; Yoon et al. 2012) means it is likely that iDG, in addition to the hyperexcitable CA3 pyramidal neurons, contributes to hippocampal dysfunction. However, the excitability of Xpnpep1$^{-/-}$ GCs requires further investigation.

Although Xpnpep1$^{-/-}$ mice exhibit neurodegenerative cell death and vacuolation in the hippocampal CA3 region, glial alterations in the Xpnpep1$^{-/-}$ hippocampus were quite different from those observed in common neurodegenerative diseases in that the density of astrocytes and expression levels of GFAP were reduced in the Xpnpep1$^{-/-}$ hippocampus, while the density of microglia was increased specifically in the CA3 subfields. Intriguingly, microglial activation was not observed in the Xpnpep1$^{-/-}$ mice. This observation suggests that the increased number of microglia in the Xpnpep1$^{-/-}$ CA3 area might be associated with physiological housekeeping functions, such as migration to sites of neuronal death to phagocytose cellular debris or apoptotic cells, rather than initiation or exacerbation of neurodegeneration(Hickman et al. 2018).

Notably, consistent with the previous in situ hybridization results (Figure 24)(Lein et al. 2007), I observed predominant Xpnpep1−

expression in neurons, but relatively weak expression in glial cells (Figure 25 and Figure 27). These observations indicate that the substrates of aminopeptidase P1 in the hippocampus are mostly cleared within the neurons and that accumulation of undigested peptide substrates containing a penultimate proline residue in the cerebrospinal fluid influences the glial population and neuronal excitability. Considering that a variety of oligopeptides with N-terminal X-pro motifs exhibit diverse biological activities(Vanhoof et al. 1995), long-term exposure of brain cells to the substrates of aminopeptidase P1 seems to result in altered gene expression in brain cells and neuro-glial interactions.

Although the underlying mechanism of decreased number of astrocytes in aminopeptidase P1-defient hippocampus does not investigate, previous studies have suggested that accumulation of substrates in extracellular region affect cell cycle and proliferative activity of astrocyte. Chronic unpredictable stress induced a reduction in astrocytes in the cerebral cortex (Banasr and Duman 2008). Treatment of glucocorticoids which is a stress hormone induces reduction in expression of Cyclin D1 protein which is a cell cycle regulatory protein in all eukaryotic cells and the number of $BrdU^+$ cell

in cultured astrocytes(Yu et al. 2011). Astrocyte proliferation is affected by altered brain microenvironment(Sofroniew 2020). Hyperglycemia inhibits cell proliferation and triggers cell cycle arrest(Nagy et al. 2019). Treatment of high glucose (12 or 25 mM) decreases proliferating cell and induces AMPK activation which suppresses cell cycle progression, but not cell death in cultured astrocytes(Li et al. 2018; Quincozes-Santos et al. 2017; Motoshima et al. 2006). Streptozotocin-induced diabetic mice show lower expression of GFAP in the cerebral cortex, hippocampus, and cerebellum(Coleman et al. 2004). Diabetic patient with hyperglycemia exhibits reduction in the number of $GFAP^{+}$ cell in the frontal cortex and hippocampus(Sonneville et al. 2012). Although whether attenuated astrocyte population in $Xpnpep1^{-/-}$ hippocampus results from decreased proliferation remains uncertain, it is possible that substrates caused by altered metabolic function in the brain microenvironment could affect astrocyte population in the aminopeptidase P1-deficient hippocampus.

A recent study showed that depletion of astrocytes by treatment with the gliotoxin L-α-aminoadipic acid (L-α-AAA) did not induce neuronal death in the hippocampal CA3 area without insults such as

ischemia, but that the loss of astrocyte produced persistent Ca^{2+} increase in the CA3 neurons after ischemia and reperfusion(Sun et al. 2018). Thus, the reduction of astrocytes in the Xpnpep1$^{-/-}$ hippocampus likely results in insufficient neuroprotection against intracellular Ca^{2+} load during burst firing or the hyperactivation of neurons rather than direct induction of neurodegeneration in the Xpnpep1$^{-/-}$ CA3 subfield. It has been suggested that S100β, an astrocytic calcium-binding protein, protects neurons against NMDA-induced cell death by activating nuclear factor κB (NF-κB) signaling(Kogel et al. 2004). In addition to neuroprotection, S100β released from astrocytes regulates neuronal activity and oscillations(Brockett et al. 2018; Morquette et al. 2015). Therefore, fewer astrocytes and resultant insufficient S100β release seem to be associated with hippocampal dysfunction in Xpnpep1$^{-/-}$ mice.

Although the neurological deficit responsible for the altered glial population require further investigation, the present study provides the molecular and cellular mechanism underlying hippocampal dysfunction and neurodegeneration in Xpnpep1$^{-/-}$ mice.

- This work is published in Yoon et al. (2021) , *Sci Rep*.

Method

Animals.

Generation and genotyping of Xpnpep1 knockout mice has been previously described[7]. Mice were backcrossed to C57BL/6J and 129S4/SvJae mice for at least 10 generations before use. All analyses were performed on littermates of both genotypes generated by intercrosses between C57BL/6J and 129S4/SvJae heterozygous parents. Animals were housed 4–5 per cage in a specific pathogen-free facility, and maintained in a climate-controlled room with free access to food and water in a 12 h light/dark cycle with the light on at 7:00. Animal maintenance and all animal experiments were performed under protocols approved by the Institutional Animal Care and Use Committee (IACUC) at Seoul National University. All methods were carried out in accordance with Guidelines for the Care and Use of Mammals in Neuroscience and Behavioral Research (National Research Council, US).

Microarray and qRT-PCR

Hippocampi were removed from 4- to 5-week-old mice of both sexes and incubated in RNA stabilization reagent (RNAlater, Qiagen, USA) at 4° C overnight. Total hippocampal RNA was prepared using QIAzol reagent and then cleaned using the RNeasy Mini Kit (Qiagen, USA) according to the manufacturer's protocol. To evaluate the integrity of the prepared RNA samples, the RNA integrity number (RIN) was determined using an Agilent 2100 Bioanalyzer (Agilent Technologies, USA), and samples with RIN (+/+, 7.37 ± 0.025; -/-, 7.25 ± 0.095) higher than 7.1 were used for further processing. The purity of RNA samples was evaluated using a spectrophotometer (NanoDrop ND-1000, Thermo Fisher Scientific, USA) by measuring the A260/A280 ratio (+/+, 2.057 ± 0.029; -/-, 2.06 ± 0.012) and the A260/A230 ratio (+/+, 1.93 ± 0.14; -/-, 1.92 ± 0.21).

Synthesis of first- and second-strand (ss) cDNA, cRNA amplification and purification, second cycle synthesis of ss-cDNA and purification, fragmentation of ss-cDNA, and biotinylation of the fragmented cDNA were conducted according to the Affymetrix GeneChip procedure. The labeled fragmented cDNA was hybridized to

the microarray chip (GeneChip Mouse Gene 1.0 ST array, Affymetrix, USA) containing 28,853 gene-level probe sets (770,317 distinct probes), and the hybridized probe array was stained with streptavidin-coupled fluorescent dye. The stained arrays were scanned with an Affymetrix GeneChip 3000 scanner, and the signal intensity of the gene expression levels was determined using Affymetrix Expression Console software. Hierarchical clustering and heatmap generation were performed using Morpheus software (https://software.broadinstitute.org/morpheus/).

Primary neuron culture

Hippocampi were collected from embryonic day 18-19 rats and were incubated in HBSS containing 2.5% trypsin at 37° C for 20 min. After rinsing with HBSS 3 times, neurons were dissociated by repeated trituration with a fire-polished Pasteur pipet, and were plated on coverslips coated with poly-l-lysine and laminin. Neurons were cultured in neurobasal medium supplemented with B27 (Invitrogen), 2 mM L-glutamine, 1% (v/v) penicillin/streptomycin (100 U/ml, Gibco), and 2% fetal bovine serum (Gibco) in a 10% CO_2 incubator.

Glia-free hippocampal neuron cultures and neuron-free glial cultures were prepared from embryonic day 18-19 mice according to the protocol described above. To establish glia-free neuronal culture, dissociated hippocampal cells were cultivated in serum-free neurobasal medium, and cells were treated with the antimitotic agent AraC (3 μM; Sigma) for 8 days from DIV 12. AraC was then removed from the culture by washing the cells with fresh neuron culture medium, and neurons were harvested at DIV 21. To obtain neuron-free glial cultures, dissociated hippocampal cells were cultured in Dulbecco' s modified Eagle' s medium containing 2.5 mM glucose, 4 mM L-glutamine, 3.7 g/L sodium bicarbonate, 10 % (v/v) FBS, 1 mM sodium pyruvate, and 1% (v/v) penicillin/streptomycin. The cell culture medium was replaced with fresh media once every 3 days. To remove neurons, cells were detached with 0.25% trypsin-EDTA at DIV 9 and plated in a new culture dish. The cells were harvested at DIV 19 when they reached 90-100% confluence.

X-gal staining and immunofluorescence staining

Four - to five-week-old male mice were deeply anesthetized with a mixture of Zoletil (50 mg/kg, intraperitoneally [i.p.]) and xylazine (1 mg/kg, i.p), and transcardially perfused with phosphate-buffered saline (PBS), followed by treatment with a fixative containing 4% (w/v) paraformaldehyde in PBS. Mouse brains were removed, post-fixed for 12 h at 4° C, and cut into 100 μm-thick sections using a vibratome (VT1200S, Leica, Germany). The sections were incubated in X-gal staining solution (5 mM $K_3Fe(CN)_6$, 5 mM $K_4Fe(CN)_6$, 2 mM $MgCl_2$, 0.01% deoxycholate, 0.02% NP-40, and 1 mg/mL X-gal in PBS) at 37° C for 5 - 8 h and then post-fixed for 1 h at 4° C. The sections were rinsed 3 times for 10 min with PBS and stored at 4° C until use. Light microscope images were acquired using a microscope (BX51WI, Olympus, Japan) equipped with a cooled charge-coupled device camera (DP73, Olympus, Japan).

For immunofluorescence staining, formalin-fixed hippocampal sections or cultured hippocampal neurons were permeabilized with 0.3% (v/v) Triton X-100 in PBS and incubated in a blocking buffer (5% normal goat serum, 5% horse serum, 5% donkey serum, and 0.5% BSA

in PBS) for 2 h. Samples were successively incubated with primary antibodies (anti-FLAG: Sigma-Aldrich, Cat. # F1804; anti-HA: Santa Cruz Biotechnology, Cat. # sc-805; anti-GFP: Synaptic Systems, Cat. # 132 004; anti-NeuN: Millipore, Cat. # ABN78; anti-MAP2: Sigma-Aldrich, Cat. # M9942; anti-GFAP: Abcam, Cat. # ab7260, Sigma-Aldrich, Cat. # G3893; anti-S100β: Sigma-Aldrich, Cat. # S2532; anti-CD68: Bio-Rad, Cat. # MCA1957GA; anti-Iba1: Novus Biologicals, Cat. # NB100-1028; anti-O4: Millipore, Cat. # MAB345; overnight at 4° C) and fluorescence (FITC, Cy3, or Alexa Fluor 647: Jackson ImmunoResearch Laboratories, PA, USA) conjugated secondary (3 h at room temperature) antibodies. After each step, the samples were rinsed 3 times for 10 min with PBS. Stained sections or neurons were mounted on a glass slide using a fluorescence mounting medium containing DAPI (Abcam, Cat. # ab104139). Images (12 bit, 2048 × 2048 pixel resolution) were acquired (pixel dwell of 4 μs, line average of 3) using a confocal laser scanning microscope (FV 3000, Olympus, Japan). Fluorescence signals were visualized using 405 nm (50 mW), 488 nm (20 mW), 561 nm (20 mW), and 640 (40 mW) lasers. Laser power and voltage of photomultiplier tube (PMT) were set to 1-

5% of the maximal output and 350−500 V, respectively.

Western blotting

Hippocampal lysates were prepared from 4− to 5−week−old mice of both sexes. Hippocampi were homogenized in a homogenization buffer (320 mM sucrose, 10 mM Tris−HCl, 5 mM EDTA, pH 7.4) containing protease inhibitor cocktails (Sigma, P8340) and phosphatase inhibitor cocktail (GenDepot, P3200). Subcellular brain fractions were prepared as described(Huttner et al. 1983).

To extract proteins from cultured hippocampal neurons or glial cells, cells were washed twice with chilled PBS and subsequently treated with a cell lysis buffer containing 1% Triton X−100, protease inhibitor cocktails, and phosphatase inhibitor cocktails. Cell lysates were centrifuged at 10,000 × g at 4° C for 15 min and supernatants were collected.

The total protein concentrations of the hippocampal homogenates, or cell lysates were determined using the Bradford protein assay (Bio−Rad, Hercules, USA). Proteins were dissolved and boiled for 5 min in

an SDS sample loading buffer (pH 6.8) containing 50 mM Tris−HCl, 2% (w/v) SDS, 10% (v/v) glycerol, 12.5 mM EDTA, 0.02% (w/v) bromophenol blue, and 5% (v/v) 2−mercaptoethanol. Samples containing 10–15 μg of protein were loaded onto SDS−PAGE gels. The separated proteins were transferred to nitrocellulose membranes. The membranes were blocked in Tris−buffered saline (TBST, 0.1% Tween 20) containing 5% skim milk for 30 min at room temperature, and then successively incubated with diluted primary and horseradish peroxidase (HRP)−conjugated secondary antibodies for 1 h at room temperature. After each step, the membranes were rinsed 3 times for 10 min with TBST. The HRP signals were detected by enhanced chemiluminescence (GE Healthcare, UK). The production of polyclonal aminopeptidase P1−antibody has been described previously (Yoon et al. 2012). Anti−α−tubulin (Cat. # T5168) and anti−βIII−tubulin (Cat. # T8660) antibodies were purchased from Sigma−Aldrich (USA). All western blot experiments were independently repeated at least 3 times, and band intensities were quantified using MetaMorph software (Molecular Devices, Sunnyvale, USA).

Statistical analysis

Statistical analyses were performed using SPSS software (IBM Corporation, NY, USA). The Shapiro-Wilk test was used to assess normality of the collected data. The two-tailed Student's *t*-test and the Mann-Whitney test were used to compare normally distributed and non-normally distributed samples, respectively. The one-way analysis of variance (ANOVA) with Tukey's post-hoc test was used for three groups of data. The levels of statistical significance are indicated as follows: n.s., not significant ($p \geq 0.05$), $*p < 0.05$, $**p < 0.01$, $***p < 0.001$. All bar and line graphs in the figures are presented as the mean ± standard error of mean (SEM).

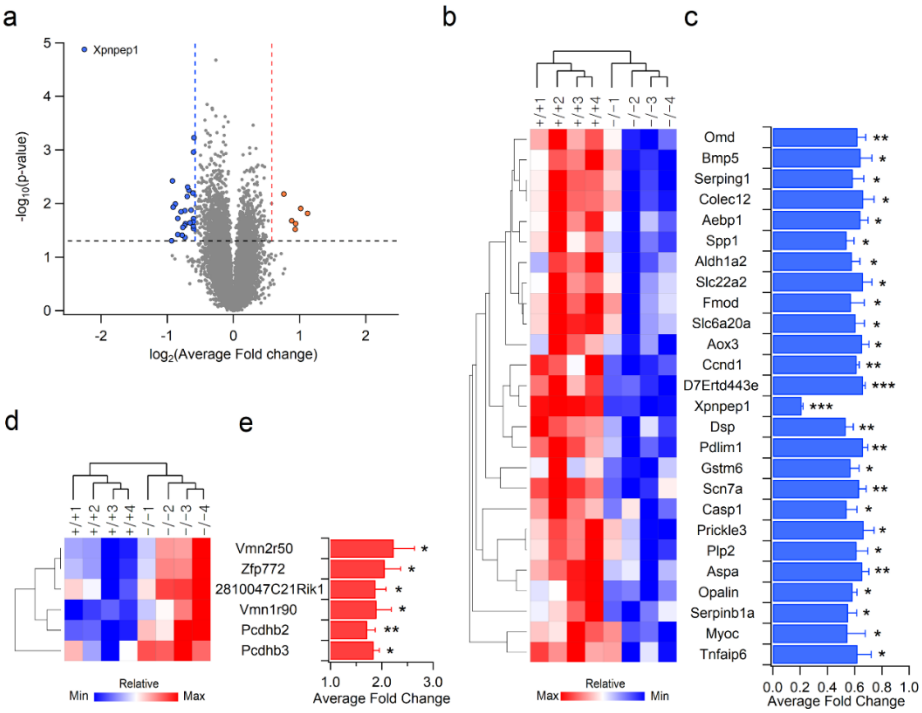
a
Xpnpep1
-log10(p-value)
log2(Average Fold change)
b
c
+/+1
+/+2
+/+3
+/+4
−/−1
−/−2
−/−3
−/−4
Omd
Bmp5
Serping1
Colec12
Aebp1
Spp1
Aldh1a2
Slc22a2
Fmod
Slc6a20a
Aox3
Ccnd1
D7Ertd443e
Xpnpep1
Dsp
Pdlim1
Gstm6
Scn7a
Casp1
Prickle3
Plp2
Aspa
Opalin
Serpinb1a
Myoc
Tnfaip6
Relative
Max
Min
Average Fold Change
d
e
Vmn2r50
Zfp772
2810047C21Rik1
Vmn1r90
Pcdhb2
Pcdhb3
Average Fold Change

Figure 22. Microarray analysis of gene expression profiling in the Xpnpep1$^{-/-}$ hippocampus.

(a) Volcano plot showing the fold change and p−value of the individual probe sets by microarray analysis. The vertical lines indicate 1.5−fold up−regulation (dotted red line) and down−regulation (dotted blue line), respectively. The horizontal dotted line represents the cutoff significance level (p = 0.05). The red and blue dots indicate up−regulated and down−regulated genes, respectively, with statistical significance. (b) The down−regulated genes in the Xpnpep1$^{-/-}$ hippocampus are visualized by heatmap and hierarchical clustering. Each gene and sample were clustered by similarity between the expression patterns of genes. Red indicates high relative expression and blue indicates low relative expression. (c) Bar graphs represent average fold changes of down−regulated genes in the Xpnpep1$^{-/-}$ hippocampus. (d, e) Treeview and hierarchical clustering (d) and average fold changes (e) of up−regulated genes in the Xpnpep1$^{-/-}$ hippocampus. (b, d) Male: +/+1, +/+4, −/−1, and −/−4; female: +/+2, +/+3, −/−2, and −/−3. (c, e) *p < 0.05; **p < 0.01; ***p < 0.001 by Student’s *t*−test, n = 4 pairs.

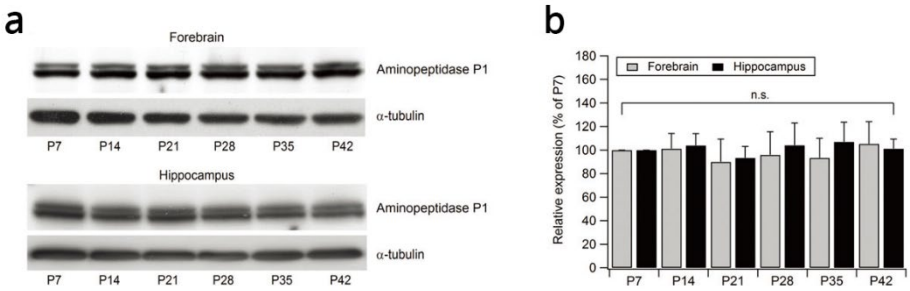

Figure 23. Developmental expression of aminopeptidase P1

(a) Developmental expression patterns of the aminopeptidase P1 proteins in the forebrain (top) and hippocampus (bottom). *α*-tubulin was used as the loading control for the western blot. P, postnatal. (b) Quantification of the aminopeptidase P1 levels in the forebrain and hippocampus. n=4 mice for each postnatal week. n.s., not significant ($P \geq 0.05$); one-way ANOVA with Tukey's HSD *post hoc* test.

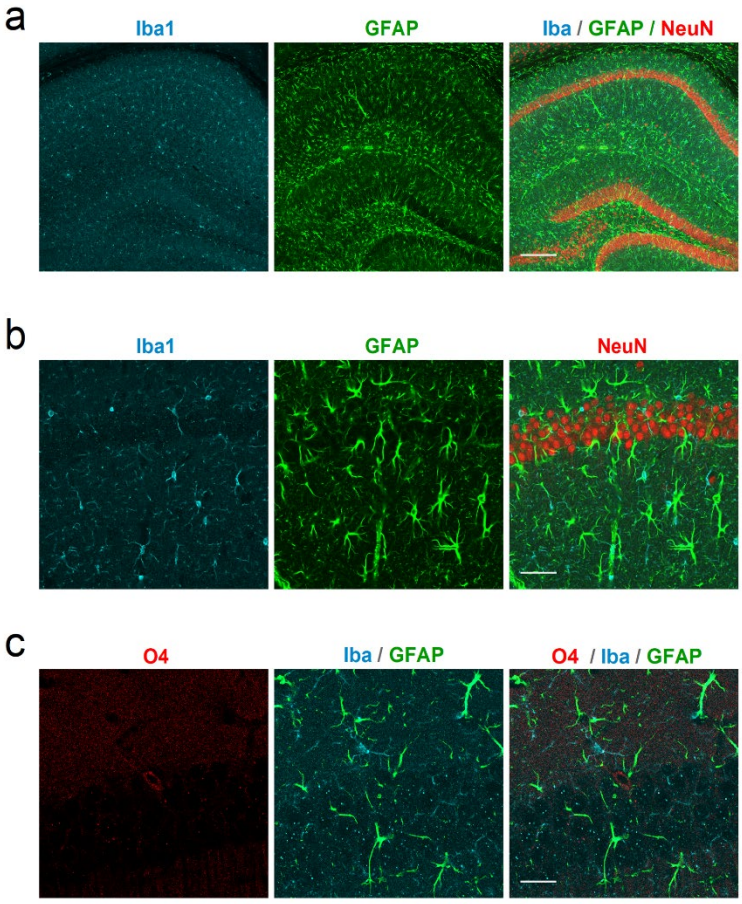
a
Iba1
GFAP
Iba / GFAP / NeuN
b
Iba1
GFAP
NeuN
c
O4
Iba / GFAP
O4 / Iba / GFAP

Figure 24. Immunohistochemical labeling of neurons and glial cells in the mouse hippocampus.

(a) Iba1-positive signals were evenly distributed throughout the hippocampus (left). GFAP-immunoreactive signals were enriched in the CA1 stratum lacunosum-moleculare and DG hilus, while principal cell layers exhibit relatively low density of GFAP-positive cells (middle). NeuN-immunoreactive signals were mostly detected in the principal cell layers (right). Scale bar, 200 μm. (b) Higher magnification images show that each antibody labels distinct cell types within the hippocampus. Scale bar, 50 μm. (c) Iba1, GFAP, and O4-postive cells constitute different populations of glial cells in the hippocampus. Scale bar, 25 μm.

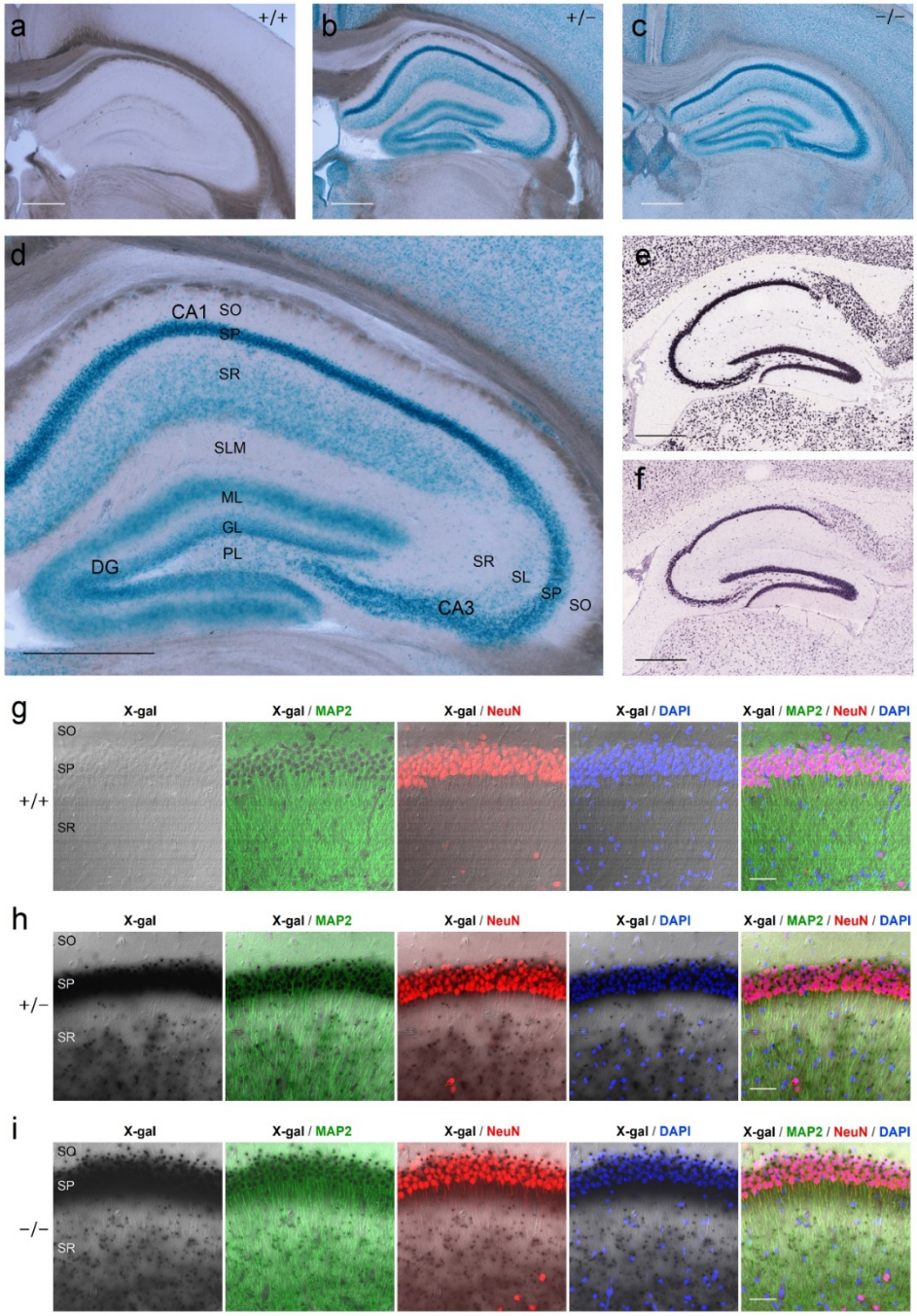
a
+/+
b
+/−
c
−/−
d
CA1
SO
SP
SR
SLM
ML
GL
PL
DG
SR
SL
SP
SO
CA3
e
f
g
X-gal
X-gal / MAP2
X-gal / NeuN
X-gal / DAPI
X-gal / MAP2 / NeuN / DAPI
+/+
SO
SP
SR
h
+/−
i
−/−

Figure 25. Aminopeptidase P1 is abundantly expressed in neurons.

(a) X-gal signals were not detected in the Xpnpep1$^{+/+}$ hippocampus. (b-c) Light-microscope images showing the X-gal staining pattern in the Xpnpep1$^{+/-}$ (b) and Xpnpep1$^{-/-}$ (c) hippocampi. (d) Higher magnification view of Xpnpep1$^{+/-}$ hippocampus shown in (b). *Stratum pyramidale* (SP) exhibits the strongest X-gal signal and disperse X-gal precipitates were detected in the *stratum radiatum* (SR) of the Xpnpep1$^{+/-}$ CA1 subfield. Occasional punctate X-gal signals were detected in the CA1 *stratum oriens* (SO) and *stratum lacunosum-moleculare* (SLM). X-gal inclusions were observed in the outer molecular layer (ML), granule cell layer (GL), and hilus (polymorphic layer, PL) of the DG. Within the CA3 subfield, X-gal signals were mainly detected in the pyramidal layer and *stratum lucidum* (SL). (e) In-situ hybridization image of neuron specific enolase (enolase 2, Eno2) showing distribution of neurons in the hippocampus (Allen Brain Atlas Experiment #:112197625). (f) Distribution of Xpnpep1 mRNA in the hippocampus (Allen Brain Atlas Experiment #:70195054) shows a pattern similar to that of Eno2. Scale bars, 500 μm (a-f). (g-i) X-gal inclusions in the hippocampal CA1 subfield were detected as dark puncta in the Xpnpep1$^{+/-}$ (h) and Xpnpep1$^{-/-}$ (i) but not in the

Xpnpep1$^{+/+}$ (g) mice by confocal microscopy with transmitted light illumination (left). Transmitted image was merged with confocal fluorescence images of MAP2, NeuN, and DAPI, respectively (middle). Right, combined transmission and fluorescence of images show the presence of X-gal precipitates in the somata and dendrites of Xpnpep1$^{+/-}$ (h) and Xpnpep1$^{-/-}$ (i) CA1 neurons. Scale bars, 50 μm (g-i).

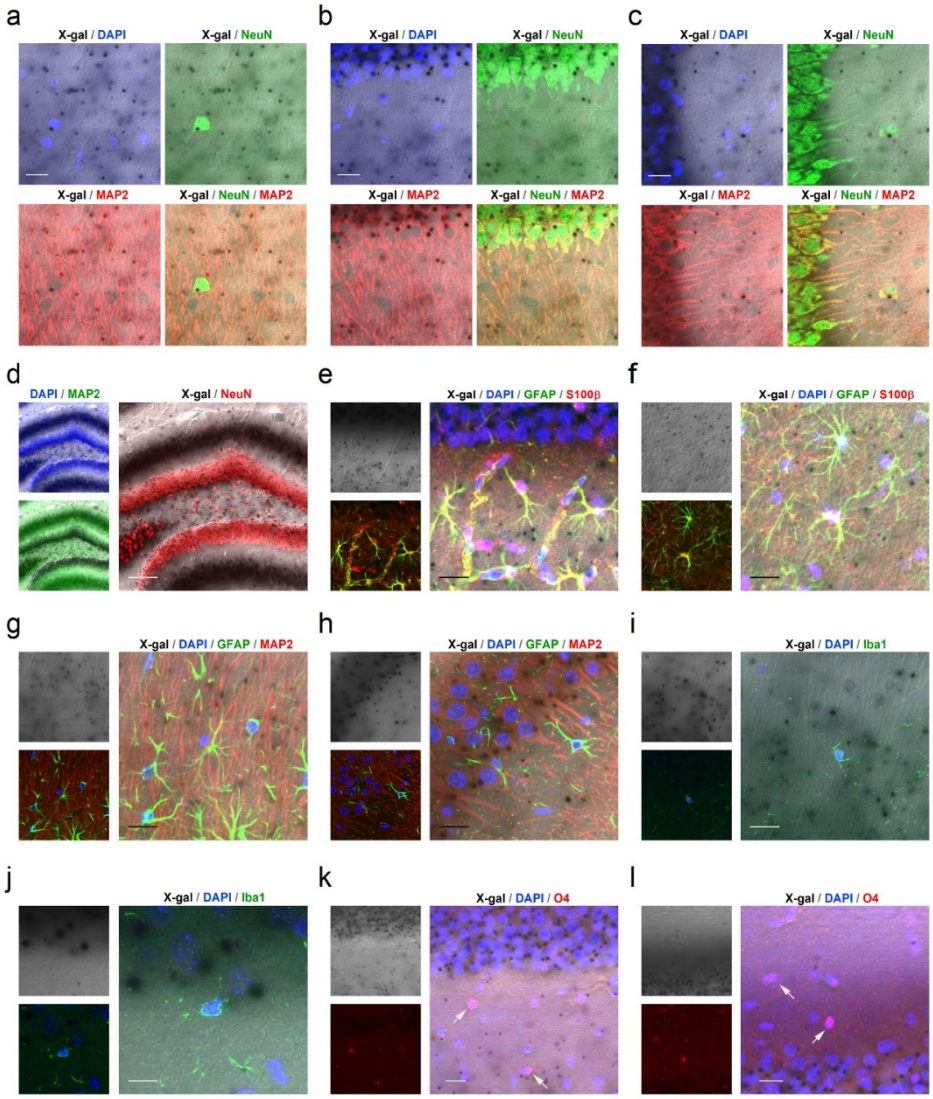
a
X-gal / DAPI
X-gal / NeuN
X-gal / MAP2
X-gal / NeuN / MAP2
b
X-gal / DAPI
X-gal / NeuN
X-gal / MAP2
X-gal / NeuN / MAP2
c
X-gal / DAPI
X-gal / NeuN
X-gal / MAP2
X-gal / NeuN / MAP2
d
DAPI / MAP2
X-gal / NeuN
e
X-gal / DAPI / GFAP / S100β
f
X-gal / DAPI / GFAP / S100β
g
X-gal / DAPI / GFAP / MAP2
h
X-gal / DAPI / GFAP / MAP2
i
X-gal / DAPI / Iba1
j
X-gal / DAPI / Iba1
k
X-gal / DAPI / O4
l
X-gal / DAPI / O4

Figure 26. X-gal staining and immunohistochemistry revealed predominant neuronal expression of aminopeptidase P1 in the Xpnpep1$^{+/-}$ hippocampus.

(a) Transmitted image of X-gal inclusions in the Xpnpep1$^{+/-}$ CA1 *stratum radiatum* region was merged with the fluorescence image of DAPI, NeuN, and/or MAP2. (b, c) Combined transmission and fluorescence of images show the presence of X-gal precipitates in the somata and dendrites of Xpnpep1$^{+/-}$ CA1 (b) and CA3 (c) neurons. (d) X-gal precipitates (black) were detected in the GC layer, hilus (polymorphic layer), and outer molecular layer of DG (left). Right, X-gal signals overlapped well with NeuN immunoreactive signals in the DG hilus. (e, f) Left, astrocytes in CA1 (e), and CA3 (f) *stratum radiatum* from the X-gal (top) stained sections were identified by immunohistochemical staining with GFAP and S100β (bottom). X-gal signals are rarely found in the cell body and processes of Xpnpep1$^{+/-}$ astrocytes (right). (g, h) Cell nuclei, neuronal dendrites, and astrocytic processes in the CA1 (g) and CA3 (h) areas from X-gal stained sections were labeled with DAPI, anti-MAP2, and anti-GFAP antibodies, respectively (left). Right, punctate X-gal signals in the CA1 *stratum radiatum* (g) and CA3 *stratum lucidum* (h) were predominantly

localized in the MAP2-positive dendrites, but they were occasionally detected in GFAP-positive astrocyte processes. (i, j) Sections were stained with X-gal (left, top), and microglia located in the CA1 (i) and CA3 (j) *stratum radiatum* were immunostained with Iba1 (left, bottom). The merged images (right) show the absence of β-galactosidase activity in Xpnpep1$^{+/-}$ microglia. (k, l) After X-gal staining (left, top), oligodendrocytes in the CA1 *stratum radiatum* (k) and *stratum oriens* (l) were immunolabeled with anti-O4 antibodies (left, bottom). Right, X-gal signals were not observed in the O4-positive cells (arrows). (a-l) DAPI was used to label the nuclei of neurons and glia. Scale bars: 10 μm (j), 20 μm (a-c, e-i, k, and l), and 100 μm (d).

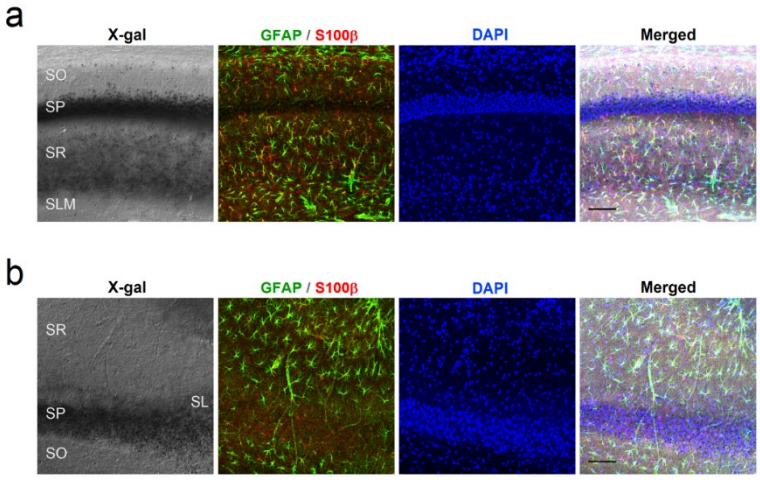

Figure 27. Distribution of astrocytes and X-gal precipitates in the Xpnpep1$^{+/-}$ hippocampus.

(a) The X-gal stained sections were immunostained with GFAP and S100β to visualize astrocytes in the hippocampus. Cell nuclei were labeled with DAPI. Note the enrichment of astrocytes in the CA1 *stratum oriens* (SO) and *stratum lacunosum-moleculare* (SLM), in which X-gal precipitates were rarely observed. (b) Astrocytes in the CA3 were abundant in the *stratum radium* (SR) and *stratum oriens* (SO), whereas X-gal signals were mostly detected in the *stratum lucidum* (SL) and *stratum pyramidale* (SP). Scale bars, 100 μm (a and b).

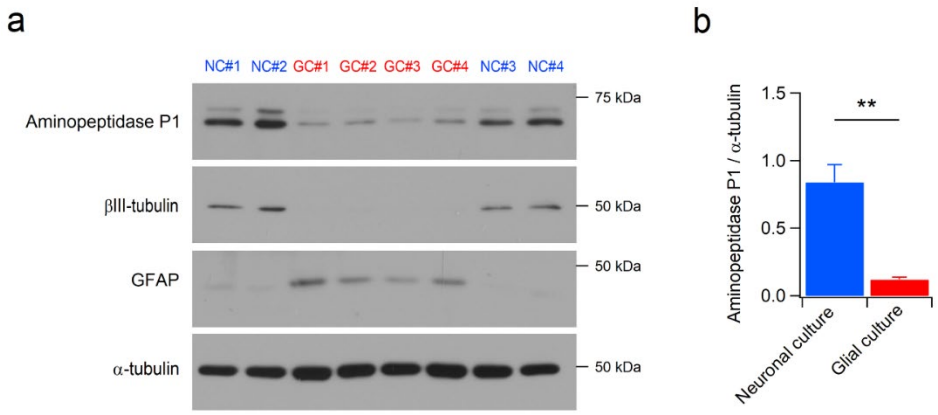

Figure 28. Protein expression levels of aminopeptidase P1 were significantly higher in neuronal lysates than in glial lysates.

(a) Total proteins extracted from 4 independent batches of cultured hippocampal neurons (NC) and glial cells (GC) were separated by SDS-PAGE. Aminopeptidase P1-immunoreactive signals were much stronger in neuronal lysates than in glial lysates. Immunoreactive signals for GFAP and βIII-tubulin were mainly detected in glial and neuronal lysates, respectively. (b) Quantification of endogenous aminopeptidase P1 protein levels (right) in the neuronal (n = 4) and glial (n = 4) lysates. $t_{(6)} = 5.44$, $^{**}p = 0.0016$ by Student's *t*-test.

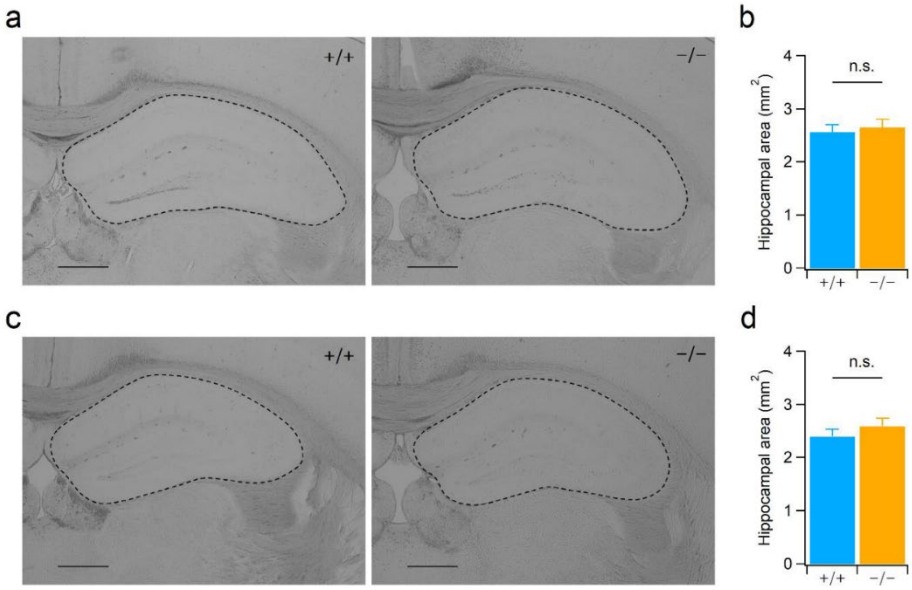
a
+/+
−/−
b
n.s.
Hippocampal area (mm²)
0
1
2
3
4
+/+
−/−
c
+/+
−/−
d
n.s.
Hippocampal area (mm²)
0
1
2
3
4
+/+
−/−

Figure 29. The areas of hippocampi in the brain sections used for the analysis of glial cell density.

(a) Representative bright−field images of the hippocampus from brain sections of WT (left) and Xpnpep1−/− (right) mice. Hippocampi are marked with a dotted line. (b) The areas of hippocampi in the brain sections used for the immunohistochemical analysis of astrocytes were not different between WT and Xpnpep1−/− (right) mice. n = 6 slices from 3 mice for each genotype; $t_{(10)} = -0.43$; n.s., not significant; p = 0.68 by Student's *t*−test. (c, d) Sample bright−field images (c) and the areas (d) of hippocampi used for the analysis of microglial cells. n = 6 slices from 3 mice for each genotype; $t_{(10)} = -0.96$; n.s., not significant; p = 0.36 by Student's *t*−test. Scale bars, 500 μm (a and c).

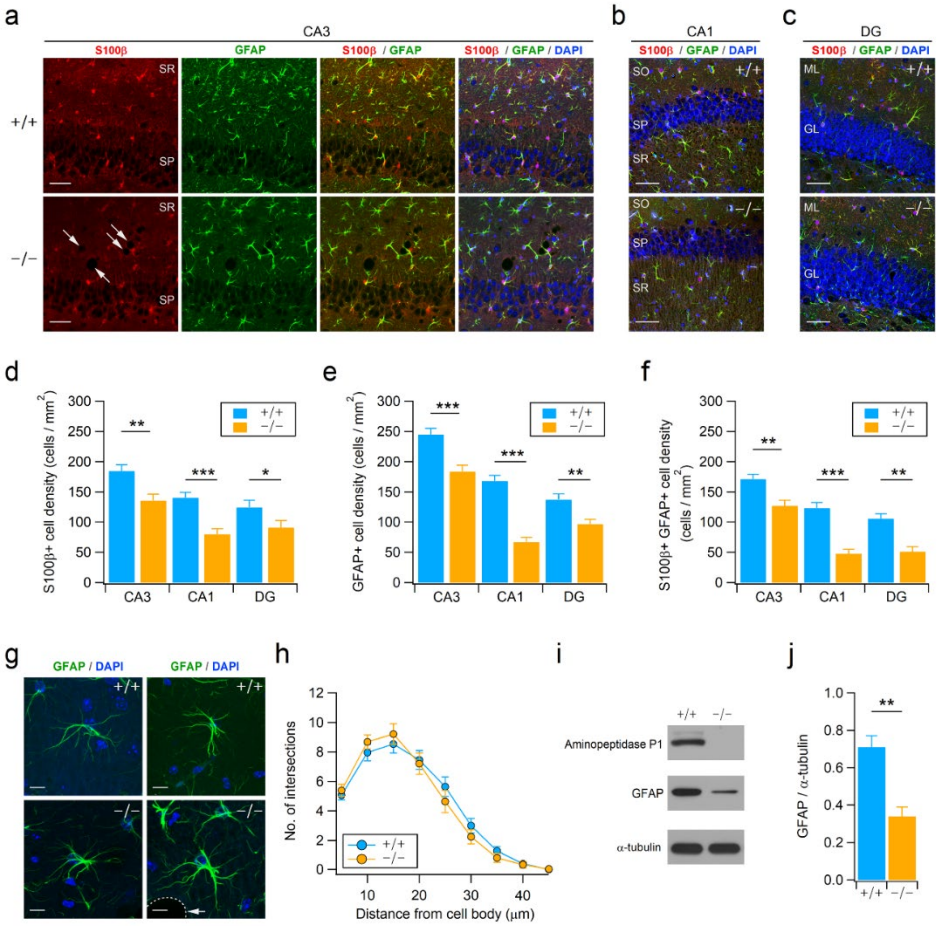
a
CA3
S100β
GFAP
S100β / GFAP
S100β / GFAP / DAPI
+/+
−/−
SR
SP
b
CA1
S100β / GFAP / DAPI
SO
SP
SR
c
DG
S100β / GFAP / DAPI
ML
GL
d
S100β+ cell density (cells / mm2)
e
GFAP+ cell density (cells / mm2)
f
S100β+ GFAP+ cell density (cells / mm2)
CA3
CA1
DG
g
GFAP / DAPI
h
No. of intersections
Distance from cell body (μm)
i
Aminopeptidase P1
GFAP
α-tubulin
j
GFAP / α-tubulin

Figure 30. Reduction of astrocytes in the Xpnpep1$^{-/-}$ hippocampus.

(a) Astrocytes in the hippocampal CA3 regions from 4- to 5-week-old WT (top) and Xpnpep1$^{-/-}$ (bottom) mice were stained with GFAP and S100β antibodies. DAPI was used to visualize cell nuclei, and arrows indicate vacuoles. Immunofluorescence images of hippocampal CA3 regions show fewer astrocytes in Xpnpep1$^{-/-}$ mice than in WT mice. (b, c) Astrocytes in the CA1 (b) and DG (c) subfields of Xpnpep1$^{+/+}$ (top) and Xpnpep1$^{-/-}$ (bottom) mice are visualized. Scale bars, 50 μm (a-c). SP, *stratum pyramidale*; SR, *stratum radiatum*; SO, *stratum oriens*; ML, molecular layer; GL, granule cell layer. (d-f) The density of GFAP- and S100β-positive cells in the CA3, CA1, and DG regions were lower in Xpnpep1$^{-/-}$ mice than in WT mice. *$p < 0.05$; **$p < 0.01$; ***$p < 0.001$ by Student's *t*-test, n = 6 slices from 3 mice for each genotype. (g) The morphology of astrocytes and cell nuclei in the hippocampal CA3 subfield were visualized by GFAP (green) and DAPI (blue), respectively. The morphological features of reactive astrocytes, such as hypertrophy and extension of processes, were not detected in Xpnpep1$^{-/-}$ astrocytes. Arrow indicates vacuole. Scale bars, 10 μm. (h) Sholl analysis of astrocyte complexity in the hippocampal CA3 subfield. n = 28 cells from 3 mice per genotype. $p > 0.05$ by Student'

s *t*−test and Mann−Whitney test. (i) Representative western blots showing the expression levels of aminopeptidase P1 and GFAP in the hippocampal extracts. Western blotting using anti−α−tubulin antibody was performed to ensure equal protein loading and transfer, and quantification of protein levels in each sample. (j) Quantification of GFAP protein levels (right) in the Xpnpep1$^{+/+}$ (n = 4) and Xpnpep1$^{-/-}$ (n = 4) hippocampus. $t_{(6)}$ = 4.62, **p = 0.0036 by Student' s *t*−test.

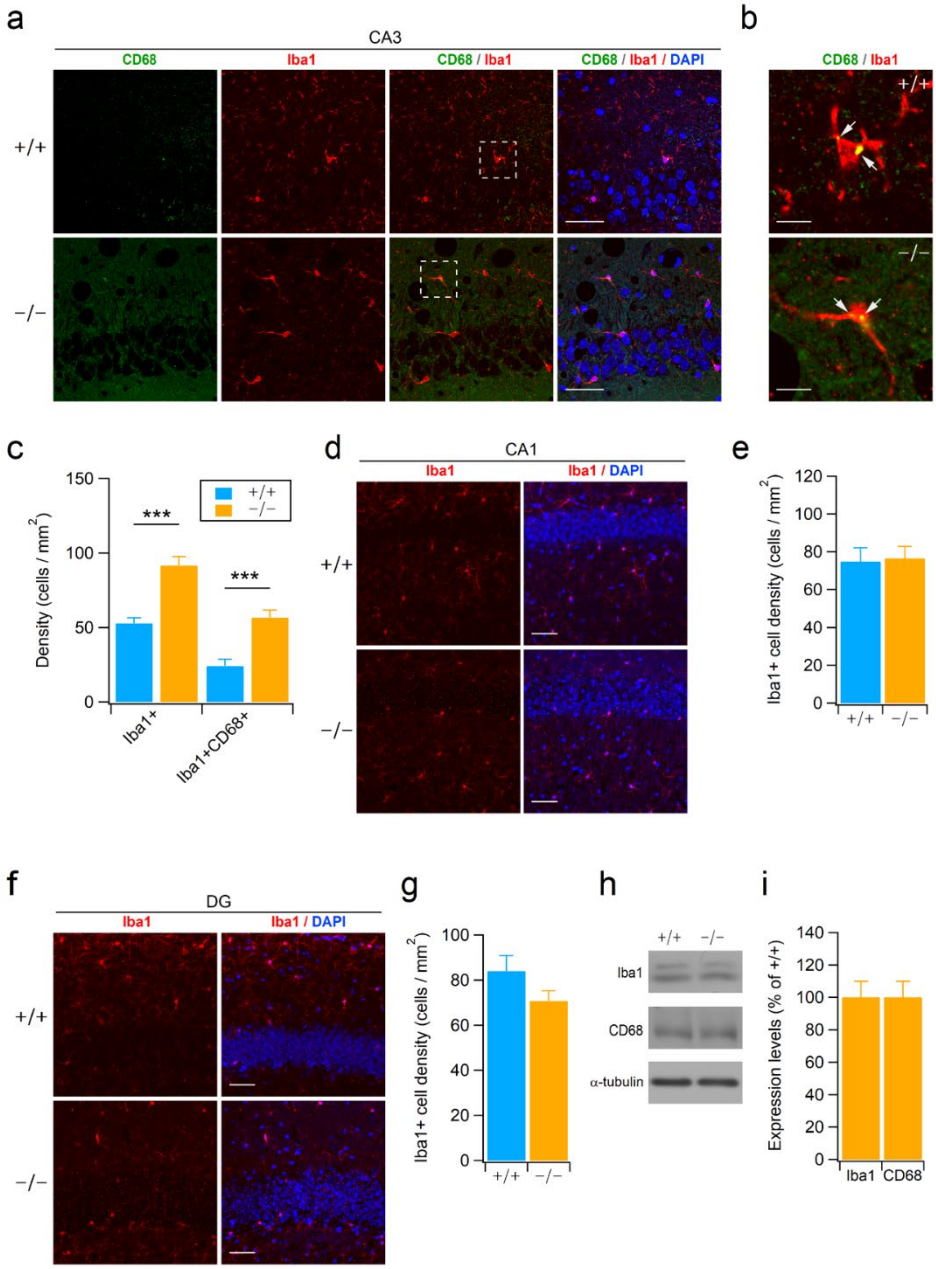
a
CA3
CD68
Iba1
CD68 / Iba1
CD68 / Iba1 / DAPI
+/+
−/−
b
CD68 / Iba1
+/+
−/−
c
Density (cells / mm2)
150
100
50
0
***
***
+/+
−/−
Iba1+
Iba1+CD68+
d
CA1
Iba1
Iba1 / DAPI
+/+
−/−
e
Iba1+ cell density (cells / mm2)
120
100
80
60
40
20
0
+/+
−/−
f
DG
Iba1
Iba1 / DAPI
+/+
−/−
g
Iba1+ cell density (cells / mm2)
100
80
60
40
20
0
+/+
−/−
h
+/+
−/−
Iba1
CD68
α-tubulin
i
Expression levels (% of +/+)
140
120
100
80
60
40
20
0
Iba1
CD68

Figure 31. The density of microglia was increased in the Xpnpep1$^{-/-}$ CA3 area.

(a) Representative images of hippocampal CA3 regions stained with CD68 and Iba1 antibodies showing a higher number of microglia in Xpnpep1$^{-/-}$ (bottom) than WT (top) mice. Scale bars, 50 μm. (b) Higher magnification views of areas indicated by the dotted white box in panel (a) show morphological features of normal resting microglia in both Xpnpep1$^{+/+}$ (top) and Xpnpep1$^{-/-}$ (bottom) mice. Scale bars, 10 μm. Note the punctate immunoreactive signals of CD68 (arrows) near the cell body but not the processes of microglia. (c) Increased density of microglia in the Xpnpep1$^{-/-}$ CA3 region. n = 6 slices from 3 mice per genotype. U = 82 (Iba1+) and 102.5 (Iba1+CD68+), Z = −4.39 (Iba1+) and −3.97 (Iba1+CD68+), ***$p < 0.001$ by Mann−Whitney test. (d) Microglia in the hippocampal CA1 area were immunostained with Iba1 antibodies (left) and merged (right) with DAPI signals. Scale bars, 50 μm. (e) Quantification of Iba1−positive cell density in hippocampal CA1 subfields. n.s., not significant. $t_{(10)} = -0.17$, $p = 0.87$ by Student's *t*−test. (f) Iba1−immnostained (left) and merged (right) images with DAPI staining showing normal density of microglia in the Xpnpep1$^{-/-}$ (bottom) DG subfield. Scale bars, 50 μm. (g) The density

of microglia in the hippocampal DG is not changed by aminopeptidase P1 deficiency. n.s., not significant. $t_{(10)} = 1.59$, $p = 0.13$ by Student's *t*-test. (h, i) Western blot images (h) and quantification (i) of Iba1 and CD68 proteins in the hippocampal lysates. n = 4 pairs. α-tubulin was used as a loading control for western blotting. $t_{(6)} = -0.21$ (Iba1) and -0.81 (CD68), $p = 0.84$ (Iba1) and 0.45 (CD68) by Student's *t*-test. n.s., not significant.

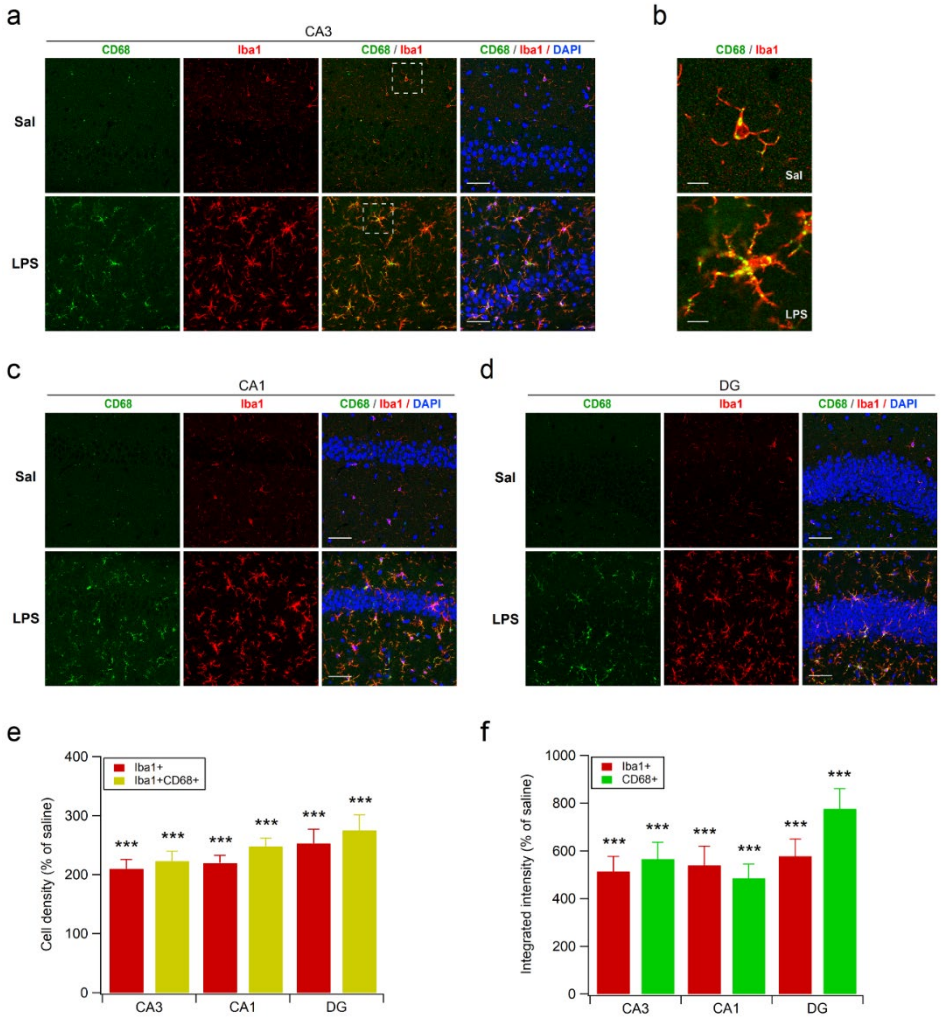
a
CA3
CD68
Iba1
CD68 / Iba1
CD68 / Iba1 / DAPI
Sal
LPS
b
CD68 / Iba1
Sal
LPS
c
CA1
CD68
Iba1
CD68 / Iba1 / DAPI
Sal
LPS
d
DG
CD68
Iba1
CD68 / Iba1 / DAPI
Sal
LPS
e
Iba1+
Iba1+CD68+
Cell density (% of saline)
400
300
200
100
0
***
CA3
CA1
DG
f
Iba1+
CD68+
Integrated intensity (% of saline)
1000
800
600
400
200
0
***
CA3
CA1
DG

Figure 32. Punctate CD68-immunoreactive signals in hippocampal microglia may be indicative of a resting state microglia.

(a) LPS treatment (once daily for 4 days) results in an increased density of microglia and enhanced expression of Iba1 and CD68 proteins in the hippocampal CA3 region of Xpnpep1$^{+/+}$ mice. (b) Higher magnification views of areas indicated by the dotted white box in panel (a) show differences in morphology and distribution of CD68-immunoreactive signals between control (top) and LPS-activated (bottom) microglia. (c, d) Representative fluorescence images of Iba1, CD68, and DAPI showing LPS-induced activation of microglia in the hippocampal CA1 (c) and DG (d) subfields of Xpnpep1$^{+/+}$ mice. Scale bars, 50 μm (a, c, and d) and 10 μm (b). (e, f) Quantification of microglial cell density (e) and fluorescence intensity (f) across the hippocampal subfields in LPS-treated mice. Data are normalized to those of saline-treated mice. n = 12 slices from 6 mice in each group. $t_{(10)} = -4.29 \sim -9.55$, ***$p < 0.001$ by Student's *t*-test.

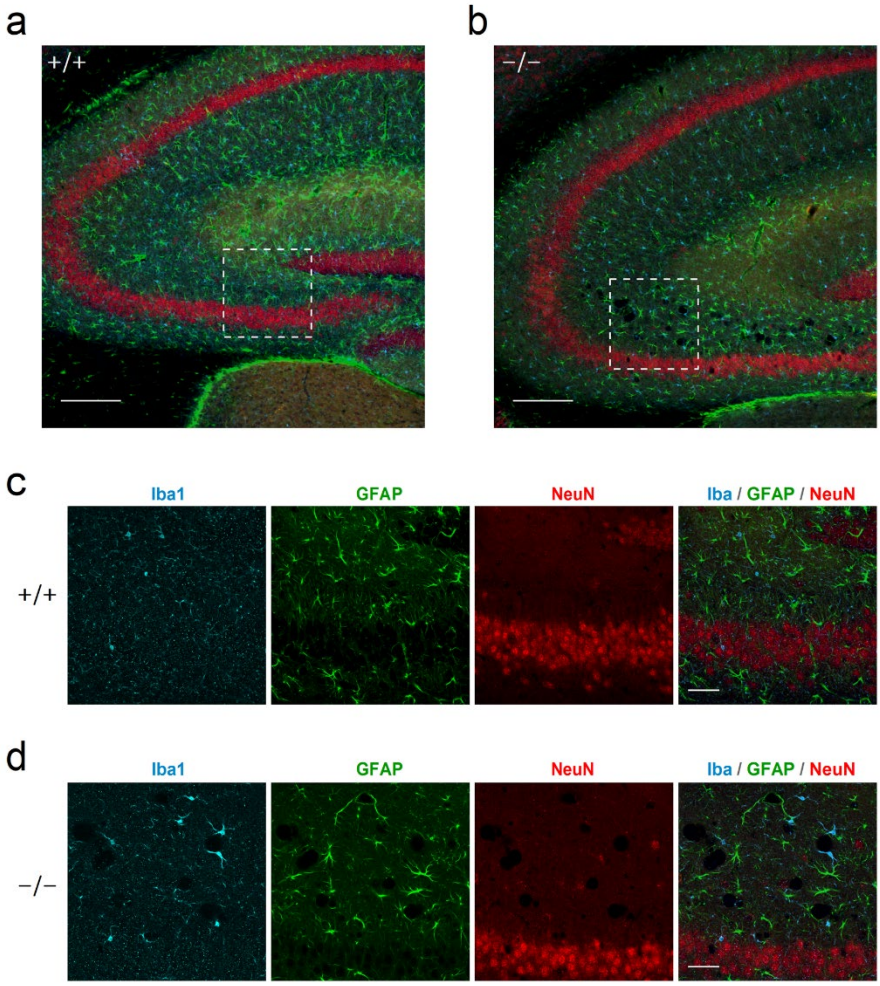
a
+/+
b
−/−
c
Iba1
GFAP
NeuN
Iba / GFAP / NeuN
+/+
d
Iba1
GFAP
NeuN
Iba / GFAP / NeuN
−/−

Figure 33. Distribution of astrocytes and microglia in the hippocampal CA3 subfield of Xpnpep1$^{+/+}$ and Xpnpep1$^{-/-}$ mice.

(a, b) Low-magnification images of Xpnpep1$^{+/+}$ (a) and Xpnpep1$^{-/-}$ (b) hippocampi showing distribution of NeuN-positive neurons, GFAP-positive astrocytes, and Iba1-positive microglia. Note the numerous vacuoles in the CA3 area of Xpnpep1$^{-/-}$ mice (b). (c, d) Compared to WT mice (c), Xpnpep1$^{-/-}$ mice (d) exhibited a higher number of microglia but fewer astrocytes in the CA3 region. However, accumulation of microglia or extension of astrocytic processes to vacuoles was not observed in the Xpnpep1$^{-/-}$ CA3 area. Scale bars, 200 μm (a and b) and 50 μm (c and d).

Table 2. Summary of developmental, behavioral, and neurological complication in aminopeptidase P1-deficient mice.

Developmental abnormalities	Reduced body size Reduced brain size Embryonic or perinatal lethality	(Yoon et al. 2012)
Behavioral abnormalities	Urinary excretion of undigested peptides containing a penultimate proline Hyperactivity Impaired hippocampus-dependent learning and memory task - Impaired novel-object recognition test - Impaired performance in Morris water maze test - Impaired contextual fear conditioning test Enhanced epileptic EEG activity	(Yoon et al. 2012) (Bae et al. 2018)
Neurological abnormalities	Reduced neuronal density in the hippocampal CA3 region Vacuolation in the hippocampal CA3 region	(Bae et al. 2018) (Yoon et al. 2021)

	Activation of cell death signaling, including apoptosis, necrosis, and autophagy Exaggerated neuronal excitability in the CA3 pyramidal neuron	

Table 3. Gene ontology analysis of differentially expressed genes in Xpnpep1$^{-/-}$ hippocampus.

Category	Term	Genes
Biological process	GO:0071310 cellular response to organic substance	CCND1, CASP1
	GO:0008152 Metabolic process	ALDH1A2, ASPA, GSTM6
Cellular component	GO:0031012 extracellular matrix	DSP, MYOC, OMD, AEBP1, FMOD
	GO:0005615 extracellular space	SERPINB1A, MYOC, TNFAIP6, OMD, SPP1, SERPING1, AEBP1, FMOD, BMP5
	GO:0005576 extracellular region	MYOC, OMD, CASP1, SPP1, SERPING1, AEBP1, FMOD, BMP5
	GO:0070062 extracellular exosome	DSP, COLEC12, SERPINB1A, MYOC, SLC22A2,

		OMD, SPP1, SERPING1, AEBP1, PLP2, ASPA
	GO:0005737 cytoplasm	DSP, MYOC, AEBP1, PDLIM1, SERPINB1A, D7ERTD443E, CCND1, ALDH1A2, AOX3, CASP1, SPP1, ASPA, GSTM6

References

Aguilar-Valles, A., D. De Gregorio, E. Matta-Camacho, M. J. Eslamizade, A. Khlaifia, A. Skaleka, M. Lopez-Canul, A. Torres-Berrio, S. Bermudez, G. M. Rurak, S. Simard, N. Salmaso, G. Gobbi, J. C. Lacaille, and N. Sonenberg. 2020. 'Antidepressant actions of ketamine engage cell-specific translation via eIF4E', *Nature*.

Ahrlund-Richter, S., Y. Xuan, J. A. van Lunteren, H. Kim, C. Ortiz, I. Pollak Dorocic, K. Meletis, and M. Carlen. 2019. 'A whole-brain atlas of monosynaptic input targeting four different cell types in the medial prefrontal cortex of the mouse', *Nat Neurosci*, 22: 657-68.

Ali, F., D. M. Gerhard, K. Sweasy, S. Pothula, C. Pittenger, R. S. Duman, and A. C. Kwan. 2020. 'Ketamine disinhibits dendrites and enhances calcium signals in prefrontal dendritic spines', *Nat Commun*, 11: 72.

Alibhai, J. D., A. B. Diack, and J. C. Manson. 2018. 'Unravelling the glial response in the pathogenesis of Alzheimer's disease', *FASEB J*, 32: 5766-77.

Alonso, M., J. H. Medina, and L. Pozzo-Miller. 2004. 'ERK1/2 activation is necessary for BDNF to increase dendritic spine density in hippocampal CA1 pyramidal neurons', *Learn Mem*, 11: 172-8.

Anacker, C., and R. Hen. 2017. 'Adult hippocampal neurogenesis and cognitive flexibility – linking memory and mood', *Nat Rev Neurosci*, 18: 335–46.

Anand, K. S., and V. Dhikav. 2012. 'Hippocampus in health and disease: An overview', *Ann Indian Acad Neurol*, 15: 239–46.

Applegarth, D. A., J. R. Toone, and R. B. Lowry. 2000. 'Incidence of inborn errors of metabolism in British Columbia, 1969–1996', *Pediatrics*, 105: e10.

Aso, E., A. Ozaita, E. M. Valdizan, C. Ledent, A. Pazos, R. Maldonado, and O. Valverde. 2008. 'BDNF impairment in the hippocampus is related to enhanced despair behavior in CB1 knockout mice', *J Neurochem*, 105: 565–72.

Autry, A. E., M. Adachi, E. Nosyreva, E. S. Na, M. F. Los, P. F. Cheng, E. T. Kavalali, and L. M. Monteggia. 2011. 'NMDA receptor blockade at rest triggers rapid behavioural antidepressant responses', *Nature*, 475: 91–5.

Bacq, A., L. Balasse, G. Biala, B. Guiard, A. M. Gardier, A. Schinkel, F. Louis, V. Vialou, M. P. Martres, C. Chevarin, M. Hamon, B. Giros, and S. Gautron. 2012. 'Organic cation transporter 2 controls brain norepinephrine and serotonin clearance and antidepressant response', *Mol Psychiatry*, 17: 926–39.

Bae, Y. S., W. Chung, K. Han, K. Y. Park, H. Kim, E. Kim, and M. H. Kim.

2013. 'Down-regulation of RalBP1 expression reduces seizure threshold and synaptic inhibition in mice', *Biochem Biophys Res Commun*, 433: 175-80.

Bae, Y. S., S. H. Yoon, J. Y. Han, J. Woo, Y. S. Cho, S. K. Kwon, Y. C. Bae, D. Kim, E. Kim, and M. H. Kim. 2018. 'Deficiency of aminopeptidase P1 causes behavioral hyperactivity, cognitive deficits, and hippocampal neurodegeneration', *Genes Brain Behav*, 17: 126-38.

Baker, M. R., and R. Y. Wong. 2019. 'Contextual fear learning and memory differ between stress coping styles in zebrafish', *Sci Rep*, 9: 9935.

Banasr, M., A. Lepack, C. Fee, V. Duric, J. Maldonado-Aviles, R. DiLeone, E. Sibille, R. S. Duman, and G. Sanacora. 2017. 'Characterization of GABAergic marker expression in the chronic unpredictable stress model of depression', *Chronic Stress (Thousand Oaks)*, 1.

Betin, C., F. V. DeFeudis, N. Blavet, and F. Clostre. 1982. 'Further characterization of the behavioral despair test in mice: positive effects of convulsants', *Physiol Behav*, 28: 307-11.

Biselli, T., S. S. Lange, L. Sablottny, J. Steffen, and A. Walther. 2021. 'Optogenetic and chemogenetic insights into the neurocircuitry of depression-like behaviour: A systematic review', *Eur J*

Neurosci, 53: 9-38.

Blau, N., A. Niederwieser, and D. H. Shmerling. 1988. 'Peptiduria presumably caused by aminopeptidase-P deficiency. A new inborn error of metabolism', *J Inherit Metab Dis*, 11 Suppl 2: 240-2.

Bradfield, L. A., B. K. Leung, S. Boldt, S. Liang, and B. W. Balleine. 2020. 'Goal-directed actions transiently depend on dorsal hippocampus', *Nat Neurosci*, 23: 1194-97.

Brockett, A. T., G. A. Kane, P. K. Monari, B. A. Briones, P. A. Vigneron, G. A. Barber, A. Bermudez, U. Dieffenbach, A. D. Kloth, T. J. Buschman, and E. Gould. 2018. 'Evidence supporting a role for astrocytes in the regulation of cognitive flexibility and neuronal oscillations through the Ca2+ binding protein S100beta', *PLoS One*, 13: e0195726.

Cabib, S., P. Campus, D. Conversi, C. Orsini, and S. Puglisi-Allegra. 2020. 'Functional and Dysfunctional Neuroplasticity in Learning to Cope with Stress', *Brain Sci*, 10.

Cammer, W., and H. Zhang. 1993. 'Atypical localization of the oligodendrocytic isoform (PI) of glutathione-S-transferase in astrocytes during cuprizone intoxication', *J Neurosci Res*, 36: 183-90.

Campeau, P. M., C. R. Scriver, and J. J. Mitchell. 2008. 'A 25-year

longitudinal analysis of treatment efficacy in inborn errors of metabolism', *Mol Genet Metab*, 95: 11-6.

Cazorla, M., J. Premont, A. Mann, N. Girard, C. Kellendonk, and D. Rognan. 2011. 'Identification of a low-molecular weight TrkB antagonist with anxiolytic and antidepressant activity in mice', *J Clin Invest*, 121: 1846-57.

Chai, H., B. Diaz-Castro, E. Shigetomi, E. Monte, J. C. Octeau, X. Yu, W. Cohn, P. S. Rajendran, T. M. Vondriska, J. P. Whitelegge, G. Coppola, and B. S. Khakh. 2017. 'Neural Circuit-Specialized Astrocytes: Transcriptomic, Proteomic, Morphological, and Functional Evidence', *Neuron*, 95: 531-49 e9.

Ciapa, B., and S. Granon. 2018. 'Expression of Cyclin-D1 in Astrocytes Varies During Aging', *Front Aging Neurosci*, 10: 104.

Coleman, E., R. Judd, L. Hoe, J. Dennis, and P. Posner. 2004. 'Effects of diabetes mellitus on astrocyte GFAP and glutamate transporters in the CNS', *Glia*, 48: 166-78.

Commons, K. G., A. B. Cholanians, J. A. Babb, and D. G. Ehlinger. 2017. 'The Rodent Forced Swim Test Measures Stress-Coping Strategy, Not Depression-like Behavior', *ACS Chem Neurosci*, 8: 955-60.

Cottrell, G. S., N. M. Hooper, and A. J. Turner. 2000. 'Cloning, expression, and characterization of human cytosolic

aminopeptidase P: a single manganese(II)-dependent enzyme', *Biochemistry*, 39: 15121-8.

Covington, H. E., 3rd, M. K. Lobo, I. Maze, V. Vialou, J. M. Hyman, S. Zaman, Q. LaPlant, E. Mouzon, S. Ghose, C. A. Tamminga, R. L. Neve, K. Deisseroth, and E. J. Nestler. 2010. 'Antidepressant effect of optogenetic stimulation of the medial prefrontal cortex', *J Neurosci*, 30: 16082-90.

Cryan, J. F., C. Mombereau, and A. Vassout. 2005. 'The tail suspension test as a model for assessing antidepressant activity: review of pharmacological and genetic studies in mice', *Neurosci Biobehav Rev*, 29: 571-625.

Csabai, D., L. Seress, Z. Varga, H. Abraham, A. Miseta, O. Wiborg, and B. Czeh. 2017. 'Electron Microscopic Analysis of Hippocampal Axo-Somatic Synapses in a Chronic Stress Model for Depression', *Hippocampus*, 27: 17-27.

Davidson, R. J., D. A. Lewis, L. B. Alloy, D. G. Amaral, G. Bush, J. D. Cohen, W. C. Drevets, M. J. Farah, J. Kagan, J. L. McClelland, S. Nolen-Hoeksema, and B. S. Peterson. 2002. 'Neural and behavioral substrates of mood and mood regulation', *Biol Psychiatry*, 52: 478-502.

de Kloet, E. R., and M. L. Molendijk. 2016. 'Coping with the Forced Swim Stressor: Towards Understanding an Adaptive

Mechanism', *Neural Plast*, 2016: 6503162.

DeBerardinis, R. J., and C. B. Thompson. 2012. 'Cellular metabolism and disease: what do metabolic outliers teach us?', *Cell*, 148: 1132-44.

Dossi, E., F. Vasile, and N. Rouach. 2018. 'Human astrocytes in the diseased brain', *Brain Res Bull*, 136: 139-56.

Duman, R. S., G. K. Aghajanian, G. Sanacora, and J. H. Krystal. 2016. 'Synaptic plasticity and depression: new insights from stress and rapid-acting antidepressants', *Nat Med*, 22: 238-49.

Duman, R. S., and L. M. Monteggia. 2006. 'A neurotrophic model for stress-related mood disorders', *Biol Psychiatry*, 59: 1116-27.

Durrenberger, P. F., F. S. Fernando, R. Magliozzi, S. N. Kashefi, T. P. Bonnert, I. Ferrer, D. Seilhean, B. Nait-Oumesmar, A. Schmitt, P. J. Gebicke-Haerter, P. Falkai, E. Grunblatt, M. Palkovits, P. Parchi, S. Capellari, T. Arzberger, H. Kretzschmar, F. Roncaroli, D. T. Dexter, and R. Reynolds. 2012. 'Selection of novel reference genes for use in the human central nervous system: a BrainNet Europe Study', *Acta Neuropathol*, 124: 893-903.

Essrich, C., M. Lorez, J. A. Benson, J. M. Fritschy, and B. Luscher. 1998. 'Postsynaptic clustering of major GABAA receptor subtypes requires the gamma 2 subunit and gephyrin', *Nat Neurosci*, 1: 563-71.

Fanselow, M. S., and H. W. Dong. 2010. 'Are the dorsal and ventral hippocampus functionally distinct structures?', *Neuron*, 65: 7–19.

Fee, C., M. Banasr, and E. Sibille. 2017. 'Somatostatin-Positive Gamma-Aminobutyric Acid Interneuron Deficits in Depression: Cortical Microcircuit and Therapeutic Perspectives', *Biol Psychiatry*, 82: 549–59.

Ferbinteanu, J., C. Ray, and R. J. McDonald. 2003. 'Both dorsal and ventral hippocampus contribute to spatial learning in Long-Evans rats', *Neurosci Lett*, 345: 131–5.

Fischell, J., A. M. Van Dyke, M. D. Kvarta, T. A. LeGates, and S. M. Thompson. 2015. 'Rapid Antidepressant Action and Restoration of Excitatory Synaptic Strength After Chronic Stress by Negative Modulators of Alpha5-Containing GABAA Receptors', *Neuropsychopharmacology*, 40: 2499–509.

Fisher, D. W., Y. Han, K. A. Lyman, R. J. Heuermann, L. A. Bean, N. Ybarra, K. M. Foote, H. Dong, D. A. Nicholson, and D. M. Chetkovich. 2018. 'HCN channels in the hippocampus regulate active coping behavior', *J Neurochem*, 146: 753–66.

Frintrop, L., S. Trinh, J. Liesbrock, C. Leunissen, J. Kempermann, S. Etdoger, M. J. Kas, R. Tolba, N. Heussen, J. Neulen, K. Konrad, V. Pafgen, F. Kiessling, B. Herpertz-Dahlmann, C. Beyer, and J.

Seitz. 2019. 'The reduction of astrocytes and brain volume loss in anorexia nervosa-the impact of starvation and refeeding in a rodent model', *Transl Psychiatry*, 9: 159.

Fuchikami, M., A. Thomas, R. Liu, E. S. Wohleb, B. B. Land, R. J. DiLeone, G. K. Aghajanian, and R. S. Duman. 2015. 'Optogenetic stimulation of infralimbic PFC reproduces ketamine's rapid and sustained antidepressant actions', *Proc Natl Acad Sci U S A*, 112: 8106-11.

Gabrys, R. L., N. Tabri, H. Anisman, and K. Matheson. 2018. 'Cognitive Control and Flexibility in the Context of Stress and Depressive Symptoms: The Cognitive Control and Flexibility Questionnaire', *Front Psychol*, 9: 2219.

Goeldner, C., D. Reiss, B. L. Kieffer, and A. M. Ouagazzal. 2010. 'Endogenous nociceptin/orphanin-FQ in the dorsal hippocampus facilitates despair-related behavior', *Hippocampus*, 20: 911-6.

Hagihara, H., K. Takao, N. M. Walton, M. Matsumoto, and T. Miyakawa. 2013. 'Immature dentate gyrus: an endophenotype of neuropsychiatric disorders', *Neural Plast*, 2013: 318596.

Han, K., M. H. Kim, D. Seeburg, J. Seo, C. Verpelli, S. Han, H. S. Chung, J. Ko, H. W. Lee, K. Kim, W. D. Heo, T. Meyer, H. Kim, C. Sala, S. Y. Choi, M. Sheng, and E. Kim. 2009. 'Regulated RalBP1 binding to RalA and PSD-95 controls AMPA receptor

endocytosis and LTD', *PLoS Biol*, 7: e1000187.

Han, Y., R. J. Heuermann, K. A. Lyman, D. Fisher, Q. A. Ismail, and D. M. Chetkovich. 2017. 'HCN-channel dendritic targeting requires bipartite interaction with TRIP8b and regulates antidepressant-like behavioral effects', *Mol Psychiatry*, 22: 458-65.

Hare, B. D., R. Shinohara, R. J. Liu, S. Pothula, R. J. DiLeone, and R. S. Duman. 2019. 'Optogenetic stimulation of medial prefrontal cortex Drd1 neurons produces rapid and long-lasting antidepressant effects', *Nat Commun*, 10: 223.

Hartley, C. A., and E. A. Phelps. 2010. 'Changing fear: the neurocircuitry of emotion regulation', *Neuropsychopharmacology*, 35: 136-46.

Hickman, S., S. Izzy, P. Sen, L. Morsett, and J. El Khoury. 2018. 'Microglia in neurodegeneration', *Nat Neurosci*, 21: 1359-69.

Homayoun, H., and B. Moghaddam. 2007. 'NMDA receptor hypofunction produces opposite effects on prefrontal cortex interneurons and pyramidal neurons', *J Neurosci*, 27: 11496-500.

Hoover, W. B., and R. P. Vertes. 2007. 'Anatomical analysis of afferent projections to the medial prefrontal cortex in the rat', *Brain Struct Funct*, 212: 149-79.

Huang, E. J., and L. F. Reichardt. 2001. 'Neurotrophins: roles in neuronal development and function', *Annu Rev Neurosci*, 24:

677-736.

Huang, R. Q., C. L. Bell-Horner, M. I. Dibas, D. F. Covey, J. A. Drewe, and G. H. Dillon. 2001. 'Pentylenetetrazole-induced inhibition of recombinant gamma-aminobutyric acid type A (GABA(A)) receptors: mechanism and site of action', *J Pharmacol Exp Ther*, 298: 986-95.

Huttner, W. B., W. Schiebler, P. Greengard, and P. De Camilli. 1983. 'Synapsin I (protein I), a nerve terminal-specific phosphoprotein. III. Its association with synaptic vesicles studied in a highly purified synaptic vesicle preparation', *J Cell Biol*, 96: 1374-88.

Jacob, T. C., S. J. Moss, and R. Jurd. 2008. 'GABA(A) receptor trafficking and its role in the dynamic modulation of neuronal inhibition', *Nat Rev Neurosci*, 9: 331-43.

Jolly, R. A., K. M. Goldstein, T. Wei, H. Gao, P. Chen, S. Huang, J. M. Colet, T. P. Ryan, C. E. Thomas, and S. T. Estrem. 2005. 'Pooling samples within microarray studies: a comparative analysis of rat liver transcription response to prototypical toxicants', *Physiol Genomics*, 22: 346-55.

Kallarackal, A. J., M. D. Kvarta, E. Cammarata, L. Jaberi, X. Cai, A. M. Bailey, and S. M. Thompson. 2013. 'Chronic stress induces a selective decrease in AMPA receptor-mediated synaptic

excitation at hippocampal temporoammonic-CA1 synapses', *J Neurosci*, 33: 15669-74.

Kang, H., and E. M. Schuman. 1995. 'Long-lasting neurotrophin-induced enhancement of synaptic transmission in the adult hippocampus', *Science*, 267: 1658-62.

Kim, C. S., P. Y. Chang, and D. Johnston. 2012. 'Enhancement of dorsal hippocampal activity by knockdown of HCN1 channels leads to anxiolytic- and antidepressant-like behaviors', *Neuron*, 75: 503-16.

Kircanski, K., J. Joormann, and I. H. Gotlib. 2012. 'Cognitive Aspects of Depression', *Wiley Interdiscip Rev Cogn Sci*, 3: 301-13.

Kobayashi, K., Y. Ikeda, A. Sakai, N. Yamasaki, E. Haneda, T. Miyakawa, and H. Suzuki. 2010. 'Reversal of hippocampal neuronal maturation by serotonergic antidepressants', *Proc Natl Acad Sci U S A*, 107: 8434-9.

Kogel, D., M. Peters, H. G. Konig, S. M. Hashemi, N. T. Bui, V. Arolt, M. Rothermundt, and J. H. Prehn. 2004. 'S100B potently activates p65/c-Rel transcriptional complexes in hippocampal neurons: Clinical implications for the role of S100B in excitotoxic brain injury', *Neuroscience*, 127: 913-20.

Koike, H., K. Fukumoto, M. Iijima, and S. Chaki. 2013. 'Role of BDNF/TrkB signaling in antidepressant-like effects of a group

II metabotropic glutamate receptor antagonist in animal models of depression', *Behav Brain Res*, 238: 48–52.

Kowalczuk, S., A. Broer, M. Munzinger, N. Tietze, K. Klingel, and S. Broer. 2005. 'Molecular cloning of the mouse IMINO system: an Na+– and Cl––dependent proline transporter', *Biochem J*, 386: 417–22.

Kowianski, P., G. Lietzau, E. Czuba, M. Waskow, A. Steliga, and J. Morys. 2018. 'BDNF: A Key Factor with Multipotent Impact on Brain Signaling and Synaptic Plasticity', *Cell Mol Neurobiol*, 38: 579–93.

Krishnan, V., and E. J. Nestler. 2011. 'Animal models of depression: molecular perspectives', *Curr Top Behav Neurosci*, 7: 121–47.

Kumar, S., S. J. Black, R. Hultman, S. T. Szabo, K. D. DeMaio, J. Du, B. M. Katz, G. Feng, H. E. Covington, 3rd, and K. Dzirasa. 2013. 'Cortical control of affective networks', *J Neurosci*, 33: 1116–29.

Kwon, H. S., N. Nakaya, M. Abu–Asab, H. S. Kim, and S. I. Tomarev. 2014. 'Myocilin is involved in NgR1/Lingo–1–mediated oligodendrocyte differentiation and myelination of the optic nerve', *J Neurosci*, 34: 5539–51.

Lein, E. S., M. J. Hawrylycz, N. Ao, M. Ayres, A. Bensinger, A. Bernard, A. F. Boe, M. S. Boguski, K. S. Brockway, E. J. Byrnes, L. Chen,

L. Chen, T. M. Chen, M. C. Chin, J. Chong, B. E. Crook, A. Czaplinska, C. N. Dang, S. Datta, N. R. Dee, A. L. Desaki, T. Desta, E. Diep, T. A. Dolbeare, M. J. Donelan, H. W. Dong, J. G. Dougherty, B. J. Duncan, A. J. Ebbert, G. Eichele, L. K. Estin, C. Faber, B. A. Facer, R. Fields, S. R. Fischer, T. P. Fliss, C. Frensley, S. N. Gates, K. J. Glattfelder, K. R. Halverson, M. R. Hart, J. G. Hohmann, M. P. Howell, D. P. Jeung, R. A. Johnson, P. T. Karr, R. Kawal, J. M. Kidney, R. H. Knapik, C. L. Kuan, J. H. Lake, A. R. Laramee, K. D. Larsen, C. Lau, T. A. Lemon, A. J. Liang, Y. Liu, L. T. Luong, J. Michaels, J. J. Morgan, R. J. Morgan, M. T. Mortrud, N. F. Mosqueda, L. L. Ng, R. Ng, G. J. Orta, C. C. Overly, T. H. Pak, S. E. Parry, S. D. Pathak, O. C. Pearson, R. B. Puchalski, Z. L. Riley, H. R. Rockett, S. A. Rowland, J. J. Royall, M. J. Ruiz, N. R. Sarno, K. Schaffnit, N. V. Shapovalova, T. Sivisay, C. R. Slaughterbeck, S. C. Smith, K. A. Smith, B. I. Smith, A. J. Sodt, N. N. Stewart, K. R. Stumpf, S. M. Sunkin, M. Sutram, A. Tam, C. D. Teemer, C. Thaller, C. L. Thompson, L. R. Varnam, A. Visel, R. M. Whitlock, P. E. Wohnoutka, C. K. Wolkey, V. Y. Wong, M. Wood, M. B. Yaylaoglu, R. C. Young, B. L. Youngstrom, X. F. Yuan, B. Zhang, T. A. Zwingman, and A. R. Jones. 2007. 'Genome-wide atlas of gene expression in the adult mouse brain', *Nature*, 445: 168-76.

Lein, E. S., X. Zhao, and F. H. Gage. 2004. 'Defining a molecular atlas of the hippocampus using DNA microarrays and high-throughput in situ hybridization', *J Neurosci*, 24: 3879-89.

Li, N., B. Lee, R. J. Liu, M. Banasr, J. M. Dwyer, M. Iwata, X. Y. Li, G. Aghajanian, and R. S. Duman. 2010. 'mTOR-dependent synapse formation underlies the rapid antidepressant effects of NMDA antagonists', *Science*, 329: 959-64.

Li, W., G. Roy Choudhury, A. Winters, J. Prah, W. Lin, R. Liu, and S. H. Yang. 2018. 'Hyperglycemia Alters Astrocyte Metabolism and Inhibits Astrocyte Proliferation', *Aging Dis*, 9: 674-84.

Li, Y., E. B. Dammer, X. Zhang-Brotzge, S. Chen, D. M. Duong, N. T. Seyfried, C. Y. Kuan, and Y. Y. Sun. 2017. 'Osteopontin Is a Blood Biomarker for Microglial Activation and Brain Injury in Experimental Hypoxic-Ischemic Encephalopathy', *eNeuro*, 4.

Luscher, B., Q. Shen, and N. Sahir. 2011. 'The GABAergic deficit hypothesis of major depressive disorder', *Mol Psychiatry*, 16: 383-406.

Marin, O. 2012. 'Interneuron dysfunction in psychiatric disorders', *Nat Rev Neurosci*, 13: 107-20.

Matias, I., J. Morgado, and F. C. A. Gomes. 2019. 'Astrocyte Heterogeneity: Impact to Brain Aging and Disease', *Front Aging Neurosci*, 11: 59.

Matsui, T., T. Nakata, and Y. Kobayashi. 2016. 'Localization of organic cation transporter 2 (OCT2) in monoaminergic and cholinergic axon terminals of the mouse brain', *Neurosci Lett*, 633: 118–24.

Meilleur, S., N. Aznavour, L. Descarries, L. Carmant, O. A. Mamer, and C. Psarropoulou. 2003. 'Pentylenetetrazol-induced seizures in immature rats provoke long-term changes in adult hippocampal cholinergic excitability', *Epilepsia*, 44: 507–17.

Mineur, Y. S., S. R. Taylor, and M. R. Picciotto. 2014. 'Calcineurin downregulation in the amygdala is sufficient to induce anxiety-like and depression-like behaviors in C57BL/6J male mice', *Biol Psychiatry*, 75: 991–8.

Miyakawa, T., M. Yamada, A. Duttaroy, and J. Wess. 2001. 'Hyperactivity and intact hippocampus-dependent learning in mice lacking the M1 muscarinic acetylcholine receptor', *J Neurosci*, 21: 5239–50.

Mizee, M. R., P. G. Nijland, S. M. van der Pol, J. A. Drexhage, B. van Het Hof, R. Mebius, P. van der Valk, J. van Horssen, A. Reijerkerk, and H. E. de Vries. 2014. 'Astrocyte-derived retinoic acid: a novel regulator of blood-brain barrier function in multiple sclerosis', *Acta Neuropathol*, 128: 691–703.

Molendijk, M. L., and E. R. de Kloet. 2015. 'Immobility in the forced swim test is adaptive and does not reflect depression',

Psychoneuroendocrinology, 62: 389-91.

Morquette, P., D. Verdier, A. Kadala, J. Fethiere, A. G. Philippe, R. Robitaille, and A. Kolta. 2015. 'An astrocyte-dependent mechanism for neuronal rhythmogenesis', *Nat Neurosci*, 18: 844-54.

Moser, M. B., and E. I. Moser. 1998. 'Functional differentiation in the hippocampus', *Hippocampus*, 8: 608-19.

Motoshima, H., B. J. Goldstein, M. Igata, and E. Araki. 2006. 'AMPK and cell proliferation--AMPK as a therapeutic target for atherosclerosis and cancer', *J Physiol*, 574: 63-71.

Moy, S. S., J. J. Nadler, A. Perez, R. P. Barbaro, J. M. Johns, T. R. Magnuson, J. Piven, and J. N. Crawley. 2004. 'Sociability and preference for social novelty in five inbred strains: an approach to assess autistic-like behavior in mice', *Genes Brain Behav*, 3: 287-302.

Nagy, T., V. Fisi, D. Frank, E. Katai, Z. Nagy, and A. Miseta. 2019. 'Hyperglycemia-Induced Aberrant Cell Proliferation; A Metabolic Challenge Mediated by Protein O-GlcNAc Modification', *Cells*, 8.

Nestler, E. J., M. Barrot, R. J. DiLeone, A. J. Eisch, S. J. Gold, and L. M. Monteggia. 2002. 'Neurobiology of depression', *Neuron*, 34: 13-25.

O'Leary, O. F., and J. F. Cryan. 2014. 'A ventral view on antidepressant action: roles for adult hippocampal neurogenesis along the dorsoventral axis', *Trends Pharmacol Sci*, 35: 675-87.

Pan, L., and J. Vockley. 2013. 'Neuropsychiatric Symptoms in Inborn Errors of Metabolism: Incorporation of Genomic and Metabolomic Analysis into Therapeutics and Prevention', *Curr Genet Med Rep*, 1: 65-70.

Phillips, J. L., S. Norris, J. Talbot, T. Hatchard, A. Ortiz, M. Birmingham, O. Owoeye, L. A. Batten, and P. Blier. 2019. 'Single and repeated ketamine infusions for reduction of suicidal ideation in treatment-resistant depression', *Neuropsychopharmacology*, 45: 606-12.

Porsolt, R. D., A. Bertin, and M. Jalfre. 1977. 'Behavioral despair in mice: a primary screening test for antidepressants', *Arch Int Pharmacodyn Ther*, 229: 327-36.

Przegalinski, E., E. Tatarczynska, A. Deren-Wesolek, and E. Chojnacka-Wojcik. 1997. 'Antidepressant-like effects of a partial agonist at strychnine-insensitive glycine receptors and a competitive NMDA receptor antagonist', *Neuropharmacology*, 36: 31-7.

Qin, C., X. L. Bian, H. Y. Wu, J. Y. Xian, C. Y. Cai, Y. H. Lin, Y. Zhou, X. L. Kou, L. Chang, C. X. Luo, and D. Y. Zhu. 2021. 'Dorsal

Hippocampus to Infralimbic Cortex Circuit is Essential for the Recall of Extinction Memory', *Cereb Cortex*, 31: 1707–18.

Quincozes–Santos, A., L. D. Bobermin, A. M. de Assis, C. A. Goncalves, and D. O. Souza. 2017. 'Fluctuations in glucose levels induce glial toxicity with glutamatergic, oxidative and inflammatory implications', *Biochim Biophys Acta Mol Basis Dis*, 1863: 1–14.

Raghuveer, T. S., U. Garg, and W. D. Graf. 2006. 'Inborn errors of metabolism in infancy and early childhood: an update', *Am Fam Physician*, 73: 1981–90.

Rajkowska, G., G. O'Dwyer, Z. Teleki, C. A. Stockmeier, and J. J. Miguel–Hidalgo. 2007. 'GABAergic neurons immunoreactive for calcium binding proteins are reduced in the prefrontal cortex in major depression', *Neuropsychopharmacology*, 32: 471–82.

Ren, Z., H. Pribiag, S. J. Jefferson, M. Shorey, T. Fuchs, D. Stellwagen, and B. Luscher. 2016. 'Bidirectional Homeostatic Regulation of a Depression–Related Brain State by Gamma–Aminobutyric Acidergic Deficits and Ketamine Treatment', *Biol Psychiatry*, 80: 457–68.

Rubin, R. D., P. D. Watson, M. C. Duff, and N. J. Cohen. 2014. 'The role of the hippocampus in flexible cognition and social behavior', *Front Hum Neurosci*, 8: 742.

Rudy, J. W., and P. Matus–Amat. 2005. 'The ventral hippocampus

supports a memory representation of context and contextual fear conditioning: implications for a unitary function of the hippocampus', *Behav Neurosci*, 119: 154–63.

Sanacora, G., R. Gueorguieva, C. N. Epperson, Y. T. Wu, M. Appel, D. L. Rothman, J. H. Krystal, and G. F. Mason. 2004. 'Subtype-specific alterations of gamma-aminobutyric acid and glutamate in patients with major depression', *Archives of General Psychiatry*, 61: 705–13.

Sanacora, G., G. Treccani, and M. Popoli. 2012. 'Towards a glutamate hypothesis of depression: an emerging frontier of neuropsychopharmacology for mood disorders', *Neuropharmacology*, 62: 63–77.

Sanderson, S., A. Green, M. A. Preece, and H. Burton. 2006. 'The incidence of inherited metabolic disorders in the West Midlands, UK', *Arch Dis Child*, 91: 896–9.

Saudubray, J. M., and A. Garcia-Cazorla. 2018. 'An overview of inborn errors of metabolism affecting the brain: from neurodevelopment to neurodegenerative disorders', *Dialogues Clin Neurosci*, 20: 301–25.

Shanahan, L., S. N. Hill, L. M. Gaydosh, A. Steinhoff, E. J. Costello, K. A. Dodge, K. M. Harris, and W. E. Copeland. 2019. 'Does Despair Really Kill? A Roadmap for an Evidence-Based Answer', *Am J*

Public Health, 109: 854–58.

Shi, H. S., W. L. Zhu, J. F. Liu, Y. X. Luo, J. J. Si, S. J. Wang, Y. X. Xue, Z. B. Ding, J. Shi, and L. Lu. 2012. 'PI3K/Akt signaling pathway in the basolateral amygdala mediates the rapid antidepressant-like effects of trefoil factor 3', *Neuropsychopharmacology*, 37: 2671–83.

Shirayama, Y., A. C. Chen, S. Nakagawa, D. S. Russell, and R. S. Duman. 2002. 'Brain-derived neurotrophic factor produces antidepressant effects in behavioral models of depression', *J Neurosci*, 22: 3251–61.

Simon, R., H. Brylka, H. Schwegler, S. Venkataramanappa, J. Andratschke, C. Wiegreffe, P. Liu, E. Fuchs, N. A. Jenkins, N. G. Copeland, C. Birchmeier, and S. Britsch. 2012. 'A dual function of Bcl11b/Ctip2 in hippocampal neurogenesis', *EMBO J*, 31: 2922–36.

Snyder, C. R., C. Harris, J. R. Anderson, S. A. Holleran, L. M. Irving, S. T. Sigmon, L. Yoshinobu, J. Gibb, C. Langelle, and P. Harney. 1991. 'The will and the ways: development and validation of an individual-differences measure of hope', *J Pers Soc Psychol*, 60: 570–85.

Sofroniew, M. V. 2020. 'Astrocyte Reactivity: Subtypes, States, and Functions in CNS Innate Immunity', *Trends Immunol*, 41: 758–

70.

Sonneville, R., H. M. den Hertog, F. Guiza, J. Gunst, I. Derese, P. J. Wouters, J. P. Brouland, A. Polito, F. Gray, F. Chretien, P. Charlier, D. Annane, T. Sharshar, G. Van den Berghe, and I. Vanhorebeek. 2012. 'Impact of hyperglycemia on neuropathological alterations during critical illness', *J Clin Endocrinol Metab*, 97: 2113–23.

Steru, L., R. Chermat, B. Thierry, and P. Simon. 1985. 'The tail suspension test: a new method for screening antidepressants in mice', *Psychopharmacology (Berl)*, 85: 367–70.

Strange, B. A., M. P. Witter, E. S. Lein, and E. I. Moser. 2014. 'Functional organization of the hippocampal longitudinal axis', *Nat Rev Neurosci*, 15: 655–69.

Sun, C., Y. Fukushi, Y. Wang, and S. Yamamoto. 2018. 'Astrocytes Protect Neurons in the Hippocampal CA3 Against Ischemia by Suppressing the Intracellular Ca(2+) Overload', *Front Cell Neurosci*, 12: 280.

Sutton, M. A., A. M. Taylor, H. T. Ito, A. Pham, and E. M. Schuman. 2007. 'Postsynaptic decoding of neural activity: eEF2 as a biochemical sensor coupling miniature synaptic transmission to local protein synthesis', *Neuron*, 55: 648–61.

Swerdlow, N. R., M. Weber, Y. Qu, G. A. Light, and D. L. Braff. 2008.

'Realistic expectations of prepulse inhibition in translational models for schizophrenia research', *Psychopharmacology (Berl)*, 199: 331–88.

Takanaga, H., B. Mackenzie, Y. Suzuki, and M. A. Hediger. 2005. 'Identification of mammalian proline transporter SIT1 (SLC6A20) with characteristics of classical system imino', *J Biol Chem*, 280: 8974–84.

Tannenholz, L., J. C. Jimenez, and M. A. Kheirbek. 2014. 'Local and regional heterogeneity underlying hippocampal modulation of cognition and mood', *Front Behav Neurosci*, 8: 147.

Thomas, A., A. Burant, N. Bui, D. Graham, L. A. Yuva–Paylor, and R. Paylor. 2009. 'Marble burying reflects a repetitive and perseverative behavior more than novelty–induced anxiety', *Psychopharmacology (Berl)*, 204: 361–73.

Tricoire, L., K. A. Pelkey, B. E. Erkkila, B. W. Jeffries, X. Yuan, and C. J. McBain. 2011. 'A blueprint for the spatiotemporal origins of mouse hippocampal interneuron diversity', *J Neurosci*, 31: 10948–70.

Turecki, G., C. Ernst, F. Jollant, B. Labonte, and N. Mechawar. 2012. 'The neurodevelopmental origins of suicidal behavior', *Trends Neurosci*, 35: 14–23.

Ugolini, F., D. Lana, P. Nardiello, D. Nosi, D. Pantano, F. Casamenti, and

M. G. Giovannini. 2018. 'Different Patterns of Neurodegeneration and Glia Activation in CA1 and CA3 Hippocampal Regions of TgCRND8 Mice', *Front Aging Neurosci*, 10: 372.

van Karnebeek, C. D., and S. Stockler. 2012. 'Treatable inborn errors of metabolism causing intellectual disability: a systematic literature review', *Mol Genet Metab*, 105: 368–81.

Vanhoof, G., F. Goossens, I. De Meester, D. Hendriks, and S. Scharpe. 1995. 'Proline motifs in peptides and their biological processing', *FASEB J*, 9: 736–44.

Widman, A. J., and L. L. McMahon. 2018. 'Disinhibition of CA1 pyramidal cells by low-dose ketamine and other antagonists with rapid antidepressant efficacy', *Proc Natl Acad Sci U S A*, 115: E3007–E16.

Wray, N. H., J. M. Schappi, H. Singh, N. B. Senese, and M. M. Rasenick. 2018. 'NMDAR-independent, cAMP-dependent antidepressant actions of ketamine', *Mol Psychiatry*.

Xiong, Z., K. Zhang, T. Ishima, Q. Ren, L. Chang, J. Chen, and K. Hashimoto. 2018. 'Comparison of rapid and long-lasting antidepressant effects of negative modulators of alpha5-containing GABAA receptors and (R)ketamine in a chronic social defeat stress model', *Pharmacol Biochem Behav*, 175:

139-45.

Xu, W., and T. C. Sudhof. 2013. 'A neural circuit for memory specificity and generalization', *Science*, 339: 1290-5.

Yamamiya, M., S. Tanabe, and R. Muramatsu. 2019. 'Microglia promote the proliferation of neural precursor cells by secreting osteopontin', *Biochem Biophys Res Commun*, 513: 841-45.

Ye, X., D. Kapeller-Libermann, A. Travaglia, M. C. Inda, and C. M. Alberini. 2017. 'Direct dorsal hippocampal-prelimbic cortex connections strengthen fear memories', *Nat Neurosci*, 20: 52-61.

Ying, S. W., M. Futter, K. Rosenblum, M. J. Webber, S. P. Hunt, T. V. Bliss, and C. R. Bramham. 2002. 'Brain-derived neurotrophic factor induces long-term potentiation in intact adult hippocampus: requirement for ERK activation coupled to CREB and upregulation of Arc synthesis', *J Neurosci*, 22: 1532-40.

Yoon, S. H., Y. S. Bae, M. S. Mun, K. Y. Park, S. K. Ye, E. Kim, and M. H. Kim. 2012. 'Developmental retardation, microcephaly, and peptiduria in mice without aminopeptidase P1', *Biochem Biophys Res Commun*, 429: 204-9.

Yoon, S. H., Y. S. Bae, S. P. Oh, W. S. Song, H. Chang, and M. H. Kim. 2021. 'Altered hippocampal gene expression, glial cell population, and neuronal excitability in aminopeptidase P1

deficiency', *Sci Rep*, 11: 932.

Yoon, S. H., B. H. Kim, S. K. Ye, and M. H. Kim. 2014. 'Chronic non-social stress affects depressive behaviors but not anxiety in mice', *Korean J Physiol Pharmacol*, 18: 263-8.

Yu, S., S. Yang, F. Holsboer, N. Sousa, and O. F. Almeida. 2011. 'Glucocorticoid regulation of astrocytic fate and function', *PLoS One*, 6: e22419.

Zanos, P., R. Moaddel, P. J. Morris, P. Georgiou, J. Fischell, G. I. Elmer, M. Alkondon, P. Yuan, H. J. Pribut, N. S. Singh, K. S. Dossou, Y. Fang, X. P. Huang, C. L. Mayo, I. W. Wainer, E. X. Albuquerque, S. M. Thompson, C. J. Thomas, C. A. Zarate, Jr., and T. D. Gould. 2016. 'NMDAR inhibition-independent antidepressant actions of ketamine metabolites', *Nature*, 533: 481-6.

Zanos, P., S. M. Thompson, R. S. Duman, C. A. Zarate, Jr., and T. D. Gould. 2018. 'Convergent Mechanisms Underlying Rapid Antidepressant Action', *CNS Drugs*, 32: 197-227.

Zhang, Y., K. Chen, S. A. Sloan, M. L. Bennett, A. R. Scholze, S. O'Keeffe, H. P. Phatnani, P. Guarnieri, C. Caneda, N. Ruderisch, S. Deng, S. A. Liddelow, C. Zhang, R. Daneman, T. Maniatis, B. A. Barres, and J. Q. Wu. 2014. 'An RNA-sequencing transcriptome and splicing database of glia, neurons, and vascular cells of the cerebral cortex', *J Neurosci*, 34: 11929-47.

Zhang, Y., S. A. Sloan, L. E. Clarke, C. Caneda, C. A. Plaza, P. D. Blumenthal, H. Vogel, G. K. Steinberg, M. S. Edwards, G. Li, J. A. Duncan, 3rd, S. H. Cheshier, L. M. Shuer, E. F. Chang, G. A. Grant, M. G. Gephart, and B. A. Barres. 2016. 'Purification and Characterization of Progenitor and Mature Human Astrocytes Reveals Transcriptional and Functional Differences with Mouse', *Neuron*, 89: 37–53.

국문초록

활성 의존적인 시냅스 가소성과 신경세포 흥분성 변화에 의한 해마 신경회로의 기능적 변형은 학습과 기억기능을 수행하는 기전으로 받아들여지고 있다. 인지기능 뿐만 아니라 해마는 뇌의 다양한 부위와 신경연결을 통해 감정 및 행동 조절에 관여한다. 해마 신경회로는 미세환경 변화에 민감하여, 다양한 질환에서 손상과 변형이 동반된다. 이러한 해마 신경회로의 변화는 인지기능과 감정행동 변화로 이어지게 된다. 그러나 해마에 의한 감정 조절은 잘 알려져 있지 않으며, 미세환경 변화는 해마 신경회로에 어떠한 변형을 유발하는지 잘 알려져 있지 않다. 본 연구에서는 인지기능 이외에 다른 기능이 알려져 있지 않은 등쪽 해마가 어떠한 감정행동 조절에 관여하는지 연구하였다. 또한, 선천성 대사 이상 및 기질 축적에 의한 미세환경 변화는 해마 유전자 발현과 세포에 어떠한 변형을 유발하는지 분석하였다. 등쪽해마 CA1 신경세포에 억제성 시냅스 수용체 발현을 감소시키거나 화학유전학적 조작을 통해 억제성 신경세포의 활성을 저하시켰을 때 실험동물에서 절망-유사행동이 감소함을 확인하였다. 반대로 GABA 수용체 작용제를 등쪽 해마에 국소적으로 주입하거나, 억제성 신경세포의 활성을 증가시켰을 때에는 마우스의 절망-유사행동이 증가함을 확인하였다. 이러한 사실은 등쪽해마의 억제성 시냅스 전도의 변화가 절망-유사행동의 변화로 이어짐을 암시한다. 미세환경 변화에 의한 해마 신경회

로 변형을 분석하기 위해 aminopeptidase P1 결핍 선천성 대사 이상 모델 마우스의 해마를 분석하였을 때, 유전자 발현의 변화와 함께 교세포 숫자의 변화를 확인하였다. 선택적인 신경세포 사멸이 일어나는 부위인 CA3 부위에서는 신경세포의 흥분성 증가와 함께 미세아교세포의 밀도가 증가하였으며, 별아교세포는 흥미롭게도 해마 전체에서 감소하였다. 이러한 결과는 aminopeptidase P1 결핍에 의해 변화된 미세환경은 별아교세포에 의한 신경세포 보호가 부족한 상황에서 신경세포의 과도한 흥분을 통해 세포사멸을 유발하며, 신경세포 사멸이 일어난 CA3 부위로 미세아교세포의 밀집을 유도함을 암시한다. 전체적으로 본 연구는 등쪽 해마가 기존에 알려진 인지기능 뿐만 아니라 절망감이나 절망행동을 조절함을 새롭게 제시하며, 선천성 대사 이상에 의한 장기적 미세환경 변화는 신경세포의 활성과 교세포 밀도의 변화를 통해 해마 기능 저하로 이어짐을 제시한다.

중심단어

해마, 해마 신경회로, 행동적 절망, 해마, 억제성 시냅스 전도, 미세환경, 선천성 대사 이상, 아미노펩티드분해효소

학번: 2013-21783